# Modeling of Patch Antennas & Feeds on Cylindrical & Doubly Conformal Platforms

L.C. Kempel, J.L. Volakis, T. Özdemir & J. Gong

Mission Research Corp.
3975 Research Blvd.
Dayton, Ohio 45340

Rome Laboratory/ ERPT
US Air Force
Griffiss AFB, New York 13441

October 1994

# Table of Contents

# EXECUTIVE SUMMARY

**Project Goal**
The goal of this project is to develop techniques and codes for modeling antennas and arrays on doubly conformal platforms. The first year emphasis is to be on cylindrical platforms whereas the second year effort is to concentrate on doubly conformal platforms such as those of satellites, missiles and aircraft.

**1st Year Progress Summary**
During the first year of this work we developed the general purpose program FEMA-CYL for radiation and scattering analysis of printed antennas and arrays on cylindrical platforms. The code is based on the finite element-boundary integral method and a challenge in its development was the efficient computation of the cylinder's Green's function. Extensive validation of the code was carried out using measured data and data from reference planar antenna codes. In addition, the effect of several parameters on scattering and radiation performance was examined. Specifically, parametric curves were computed which show the effect of curvature on input impedance, beamwidth gain and scattering. The theory and formulation of the code are described in the U-M Radiation Laboratory Report 031173-2-T and a user and test case manual was delivered along with the code FEMA-CYL.

To account for dielectric coatings and fully conformal (doubly curved platforms) it was necessary to develop a code which does not rely on a Green's function for terminating the finite element mesh. This led us to the development of a finite element ABC code. In this code the finite element mesh is terminated by an absorbing boundary condition, whereas in FEMA-CYL the mesh is terminated by the Stratton-Chu boundary integral. The ABC permits the analysis of antennas recessed on any platform but has the disadvantage of being less rigorous than the boundary integral. Nevertheless, it is a computationally attractive alternative because the formulation provides reasonably accurate answers to otherwise untractable problems. The code FEMA-CYLA was developed on the basis of this formulation and results generated by this code were found in good agreement with reference date when the mesh is terminated a mere 0.3 wavelengths from the antenna surface. Because FEMA-CYLA still uses the cylindrical shell for discretizing the volume, it is only applicable to antennas on cylindrical platforms but can handle patches and arrays with superstrates. Only limited validation of the

1

code has been carried out for modeling antennas with superstrates because of a lack of reference data. Measurements though have just been completed using the model illustrated in Figure 1. The patches on this cylinder-ogive model were coated and comparison between measurements and calculations will be carried out over the next month.

Over the last three months of this year work shifted to the development of the future code FEMA-PRISM suitable for modeling a variety of printed antennas (circular, rectangular, spirals, slots, apertures, etc.) on a doubly curved platform. The key feature of the code is the use of the new edge-based distorted prism shown below.
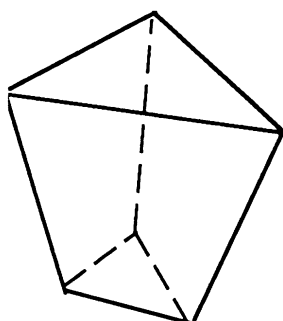


*Distorted Prism*

So far, we developed and implemented the finite element matrix for these elements and performed a number of validations for scattering and radiation analyses. Using this preliminary version of FEMA-PRISM results were obtained for several patch antennas on cylindrical and planar platforms. Thus, FEMA-PRISM supersedes FEMA-CYL and FEMA-CYLA.

An important advantage of using the prism is the possibility of avoiding sophisticated meshing packages for generating the volume mesh. Instead, by using prisms the mesh can be "grown" off the surface, thus generating a simple structural mesh (see Fig.2). Consequently, simple preprocessors can be developed to mesh standard antenna elements. Of course, this does not preclude the possibility of using sophisticated meshing packages for antennas of arbitrary shape.

An important development during the latter four months was the introduction of a new approach for modeling coax and slot antenna feeds in the context of the finite element method. This formulation is based on the continuity of the potential rather than the tangential field and allows for the independent meshing of the antenna volume and feed region. The document entitled "An Efficient and Accurate Model of the Coax Cable Feeding Structure for FEM Simulation" describes this formulation for a coaxial cable feed.

This annual progress report contains four independent sections as listed in the Table of contents. Each section describes the formulation and provides validation and results as generated by the codes mentioned above. The reader is referred to reports #031307-1-T and 031307-2-T which are the users manuals of the codes FEMA-CYL and FEMA-CYLA. The FEMA-PRISM code is still in development and will incorporate the new feed models described in the section by Gong and Volakis.
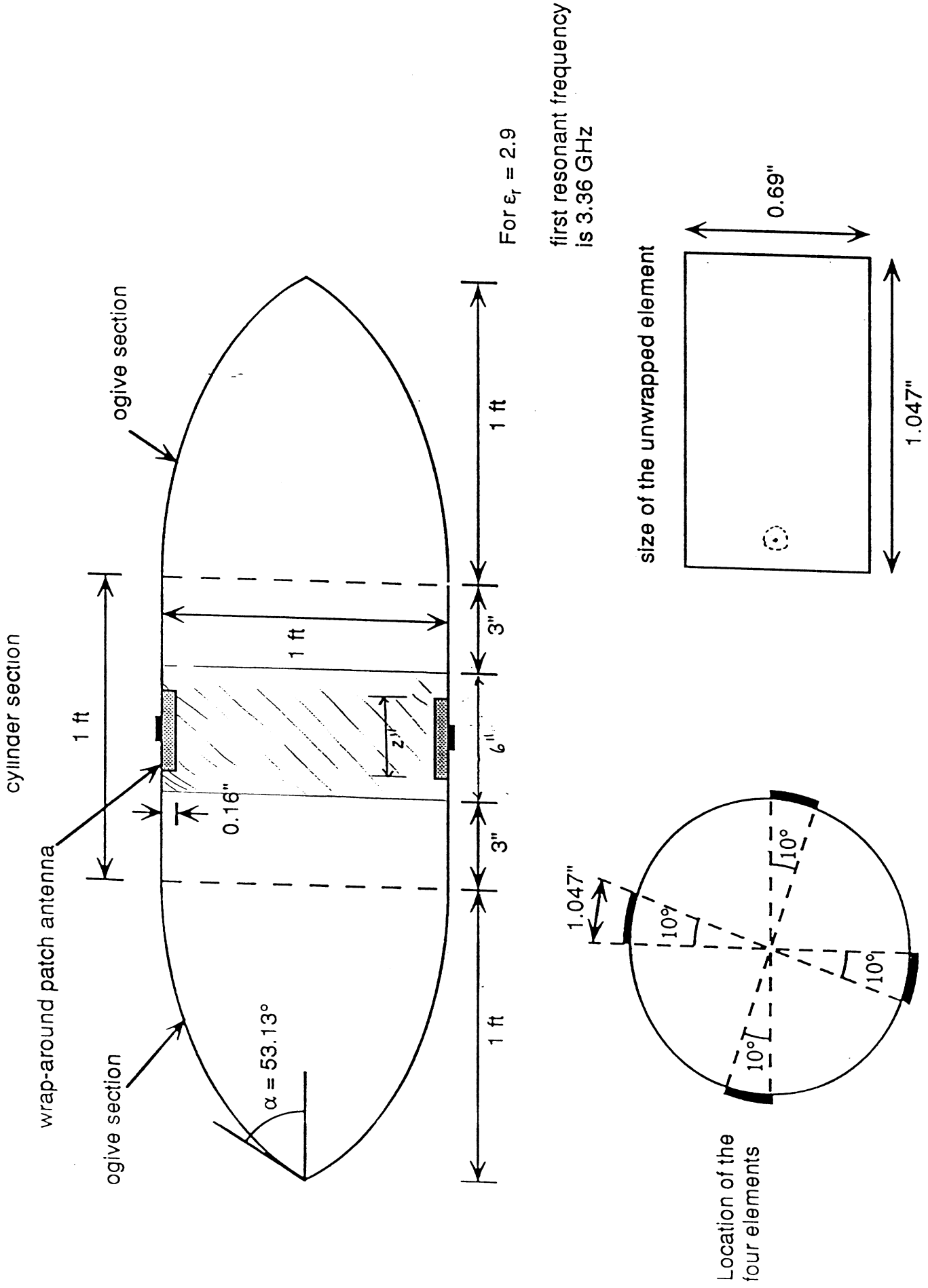
cylinder section

ogive section

wrap-around patch antenna

ogive section

$\alpha = 53.13°$

1 ft

0.16"

1 ft

1 ft

3"

6"

3"

1 ft

z"

For $\varepsilon_r = 2.9$

first resonant frequency is 3.36 GHz

size of the unwrapped element

0.69"

1.047"

Location of the four elements

1.047"

10°

10°

10°

10°

*Figure 1* : Measurement model for patches on a coated cylinder

4

FEM-ABC analysis of cavity-backed *conformal antennas* mounted on doubly curved platforms using *distorted triangular prisms* as finite elements
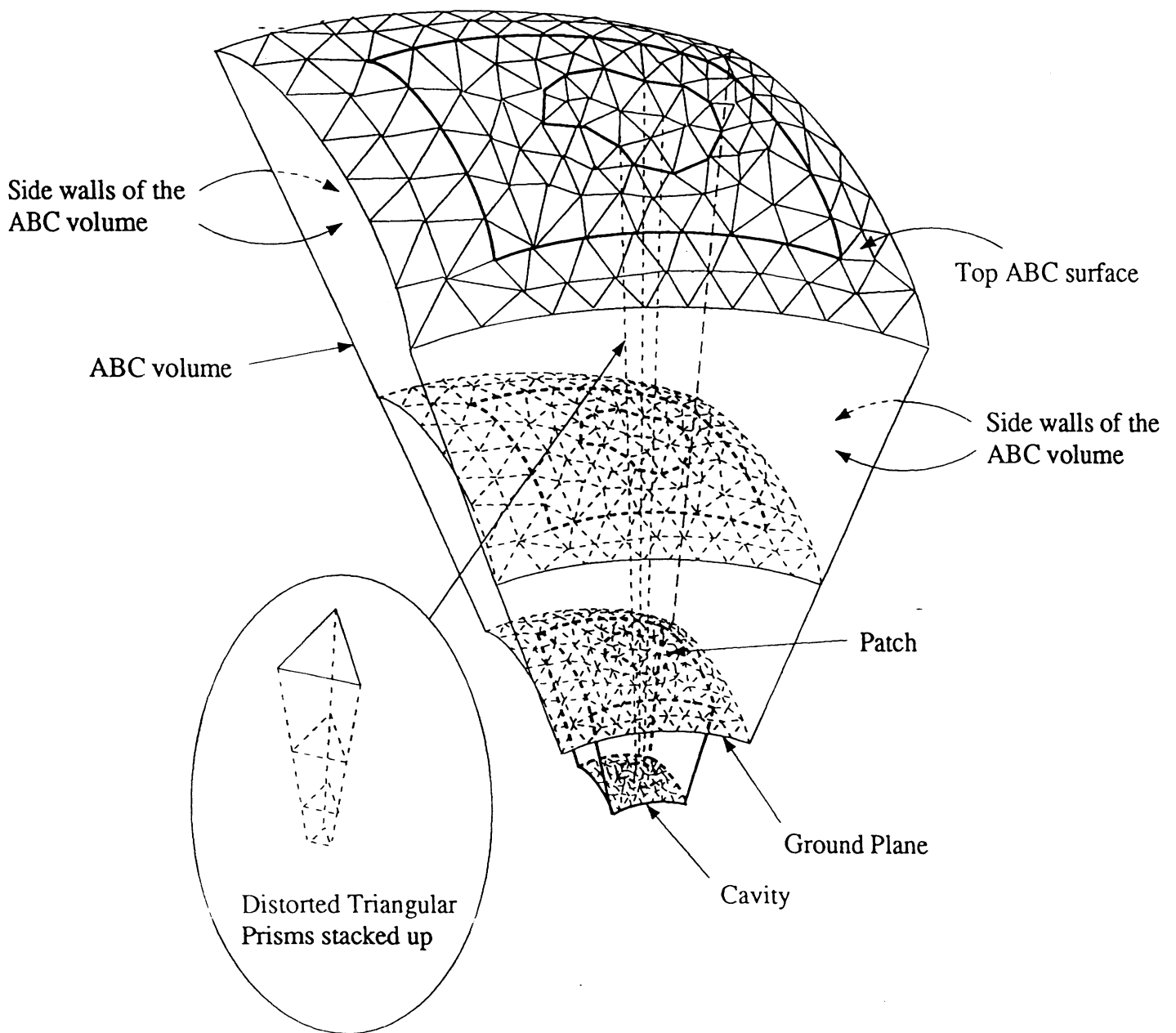
Side walls of the ABC volume

ABC volume

Top ABC surface

Side walls of the ABC volume

Patch

Distorted Triangular Prisms stacked up

Ground Plane

Cavity

*Figure 2* : Illustration of the prismatic mesh for modeling antennas on doubly curved platforms

5

# Radiation by Cavity-backed Antennas on a Circular Cylinder

Leo C. Kempel, John L. Volakis
Radiation Laboratory
University of Michigan
1301 Beal Ave.
Ann Arbor, MI 48109-2122
and
Randall J. Sliva
Naval Air Warfare Center
China Lake, CA 93555-6001

June 14, 1994

## Abstract

Conformal antenna arrays are popular for deployment on curved aircraft, spacecraft and land vehicle platforms due to their inherent low weight, cost and drag properties. However, to date there has been a dearth of rigorous analytical and numerical solutions to aid the designer. In fact, it has been common practice to use limited measurements and planar approximations in designing such non-planar antennas. In this paper, we extend the finite element-boundary integral method to radiation by cavity-backed structures recessed in an infinite, metallic cylinder. The accuracy of the developed FE-BI code for a microstrip patch arrays is established by comparison with measurements. The formulation is then used to investigate the effect that the finite aperture has on the radiation pattern. In addition, the effect of curvature on resonant frequency, gain, input impedance and pattern shape is examined.

# 1  Introduction

Modern aircraft and missile designs seek to utilize conformal antenna arrays rather than conventional protruding antennas due to their low weight, low drag, low cost and flexibility. Although most useful aircraft surfaces possess some curvature, the vast majority of available design information assumes planar elements. Indeed, the literature is rich with approximate [1], numerical [2] and experimental [3] design and characterization data for planar structures. The most common antenna element is a microstrip patch printed on a dielectric coated groundplane. Dielectric coated cylinders have also been investigated using approximate [4] and numerical [5] approaches.

Often, it is desirable to enclose each radiating element within a metallic cavity to suppress parasitic substrate coupling [6]. Approximate methods, such as the cavity model [1], do not include finite aperture effects since the radiating currents are restricted to the immediate vicinity of the patch. Most integral equation formulations such as the one proposed by Pozar and Voda [2] utilize a grounded slab Green's function in their construction which precludes practical finite aperture simulations. Recently, Aberle [6] proposed an integral equation formulation which partitions the geometry into an exterior half space and an interior homogeneously filled cavity. This approach determines the electric field attributed to the patch and feed currents and the two regions are coupled by enforcing field continuity across the finite aperture. Unfortunately, as with all integral formulations, the linear system requires $\mathcal{O}(N^2)$ storage and considerable computational effort due the fully populated system and the slowly converging cavity Green's function. The simulation of large finite cavity-backed arrays using such an approach is therefore not practical.

An alternative formulation, utilizing the Finite Element-Boundary Integral (FE-BI) method, was proposed by Jin and Volakis [7]. This approach is also suitable for inhomogeneously filled cavity-backed antennas recessed in a metallic ground plane. As with all partial differential equation formulations, this approach is associated with a highly sparse system which requires only $\mathcal{O}(N)$ storage. Additionally, when coupled with a Conjugate or Biconjugate Gradient-Fast Fourier Transform (BiCG-FFT) solver, the computational burden is significantly reduced. The FE-BI method has been successfully used for scattering and antenna performance analysis involving planar platforms.

A similar FE-BI method was proposed by the authors [8] for scattering

7

by cylindrical-rectangular and wraparound patch antennas. New divergence free, high fidelity edge-based elements were presented along with an efficient solution strategy which exploited an asymptotic evaluation of the appropriate dyadic Green's function as well as a BiCG-FFT solver. The resulting computer code was shown to accurately compute the scattering by both planar and highly curved elements. This paper investigates the accuracy and utility of such a FE-BI formulation for antenna performance analysis. The radiation pattern of a single element as well as that of a wraparound array is compared with measured results. The importance of modelling finite apertures is examined and in addition, the effect that curvature has on the resonant frequency, gain, driving point impedance and pattern shape is quantified.

## 2   Formulation

In this section, the FE-BI formulation appropriate for radiation analysis is developed for cavity-backed antennas recessed in an infinite metallic cylinder (see figure 1). As usual, the finite element formulation permits substantial modeling flexibility, including cavity inhomogeneities, lumped loads and microstrip feeding lines.

The FE-BI formulation begins with the weak form of the vector wave equation followed by specification of appropriate vector shape functions and dyadic Green's function. The resulting FE-BI equations are then used to solve for the total electric fields within the cavity and on the aperture (for further details, see Volakis *et al.* [9]). The weak form of the wave equation can be written as

$$\sum_j E_j \left\{ \int_{V_i} \left[ \frac{\nabla \times \vec{W_j}(\rho,\phi,z) \cdot \nabla \times \vec{W_i}(\rho,\phi,z)}{\mu_r(\rho,\phi,z)} \right. \right.$$

$$-k_o^2 \epsilon_r(\rho,\phi,z)\vec{W_j}(\rho,\phi,z) \cdot \vec{W_i}(\rho,\phi,z) \bigg] \rho\, d\rho\, d\phi\, dz$$

$$+(k_o a)^2 \delta_a(j)\delta_a(i) \int_{S_i} \int_{S_j} \left[ \vec{W_i}(a,\phi,z) \cdot \hat{\rho}(a,\phi,z) \times \right.$$

$$\left. \overline{\overline{G}}_{e2}(a,\bar{\phi},\bar{z}) \times \hat{\rho}(a,\phi',z') \cdot \vec{W_j}(a,\phi',z') \right] d\phi'\, dz'\, d\phi\, dz \bigg\} = f_i^{int} \quad (1)$$

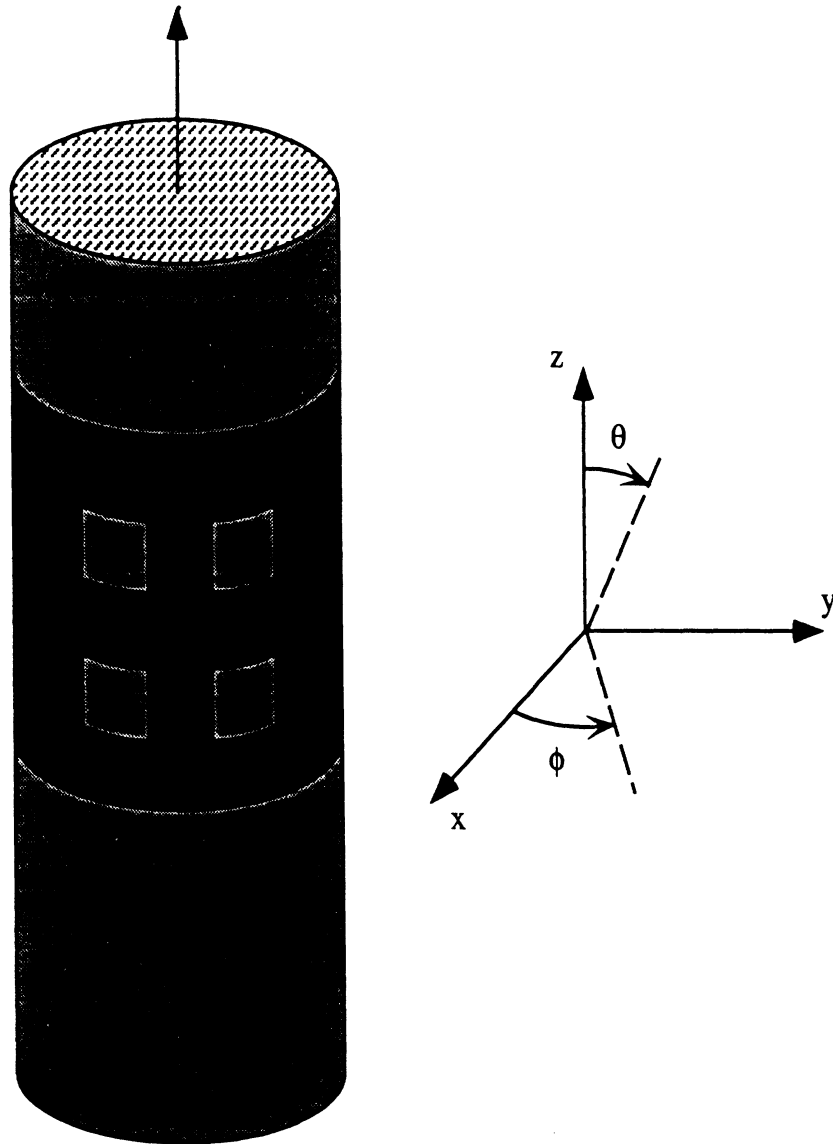In this, $\vec{W_i}$ are vector basis functions with support limited to the finite el-

Figure 1: Illustration of a typical cavity-backed antenna situated on a metal-lic cylinder and the associated coordinate system.

ement volume $V_i$ which is associated with the $i^{th}$ degree of freedom, and in a similar fashion, $S_i$ and $S_j$ represent aperture surfaces associated with the $i^{th}$ and $j^{th}$ degrees of freedom, respectively. The appropriate dyadic Green's function is denoted by $\overline{\overline{G}}_{e2}$ and it has convolutional ($\bar{\phi} = \phi - \phi'$, $\bar{z} = z - z'$) form when evaluated on the surface of the cylinder, $\rho = a$. The unprimed coordinates represent the test point while the primed ones denote the source point and $(\rho, \phi, z)$ are the usual cylindrical coordinates. The free-space propagation constant is given by $k_0 = \frac{2\pi}{\lambda_0}$, where $\lambda_0$ is the free-space wavelength. The cavity is filled with an inhomogeneous material having relative constitutive properties $\epsilon_r$ and $\mu_r$. The function $\delta_a(i)\delta_a(j)$ identifies when both the source and test unknowns belong to the aperture and accordingly contribute to the boundary integral sub-matrix. The FE-BI equation (1) may be rewritten in matrix form as

$$\left[\mathcal{A}\right] \begin{Bmatrix} E_j^{ap} \\ E_j^{int} \end{Bmatrix} + \begin{bmatrix} [\mathcal{G}] & [0] \\ [0] & [0] \end{bmatrix} \begin{Bmatrix} E_j^{ap} \\ E_j^{int} \end{Bmatrix} = \begin{Bmatrix} \{0\} \\ \{f_i^{int}\} \end{Bmatrix} \tag{2}$$

where the entries of $[\mathcal{A}]$ are due to the FE portion of the formulation and $[\mathcal{G}]$ is the boundary integral sub-matrix. In (2), $E_j^{ap}$ and $E_j^{int}$ denote degrees of freedom associated with the aperture and interior fields, respectively. In (2), $f_i^{int}$ represents the internal excitation and for this paper, a radially oriented probe feed is considered.

The vector elements, dyadic Green's function evaluation, matrices $[\mathcal{A}]$ and $[\mathcal{G}]$ and the far-zone field formulae are given in [8] and are therefore not repeated here. The interior source function is given by

$$f_i^{int} = -\int_{V_i} \left\{ \nabla \times \left[ \frac{\vec{M}^{int}(\rho, \phi, z)}{\mu_r(\rho, \phi, z)} \right] + jk_oZ_o\vec{J}^{int}(\rho, \phi, z) \right\} \cdot \vec{W}_i(\rho, \phi, z)\rho \, d\rho \, d\phi \, dz \tag{3}$$

where $\vec{J}^{int}$ and $\vec{M}^{int}$ are the impressed electric or magnetic current densities. For a radially ($\hat{\rho}$) directed probe feed, the impressed current located at $(\phi_s, z_s)$ is given by

$$\vec{J}^{int} = \hat{\rho}I_0\frac{\delta(\phi - \phi_s)(z - z_s)}{\rho} \tag{4}$$

10

and (3) becomes

$$f_i^{int} = -jk_oZ_oI_o\frac{\tilde{s}_i\rho_b}{\alpha_ih_i}\ln\left(\frac{\rho_b}{\rho_a}\right)\left[\left(\phi_s - \tilde{\phi}_i\right)(z_s - \tilde{z}_i)\right] \tag{5}$$

if the edge-based elements introduced in [8] are used.

Having computed the finite element and boundary integral matrices as well as the internal excitation, the BiCG method is used to solve for the unknown electric fields throughout the computation domain. Given that the FE matrix is highly sparse and symmetric, the BiCG method is a well-suited choice among iterative solvers. It is also important to note that the matrix-vector product associated with the boundary integral can be performed using FFTs resulting in a reduced storage and computational burden. The computed electric field within and on the aperture of the cavity may now be used to compute antenna parameters such as the gain and the input impedance.

The radiated magnetic field is computed by integrating the aperture fields with the far-zone dyadic Green's function given in [8]

$$\vec{H}^r(r,\theta,\phi) = jY_ok_oa\int_S \overline{\overline{G}}_{e2}(r,\theta,\phi;a,\phi',z')\cdot$$
$$\left[\hat{\rho}(a,\phi',z') \times \vec{E}(a,\phi',z')\right]d\phi'\,dz' \tag{6}$$

where $(r,\theta,\phi)$ indicates the observation point in spherical coordinates. The far-zone electric field may be obtained from (6) in the usual manner. The radiation pattern, directive gain and other useful antenna parameters may be calculated using (6). For example, the antenna gain may be computed from the far-zone electric field as

$$G_{dB}(\theta,\phi) = 10\log_{10}\left[4\pi|E^r(\theta,\phi)|^2\right] + 10\log_{10}\left[\frac{1}{Z_0R_{in}}\right] \tag{7}$$

where $R_{in}$ is the input resistance which is given below and $E^r$ is the radiated electric field as $r \to \infty$.

In addition to the antenna gain, designers are concerned with the input impedance of an antenna for feed line matching purposes. The input impedance is comprised of two contributions [10]

$$Z_{in} = Z_P + Z_D \tag{8}$$

**11**

where the first term is the probe's self-impedance and the second term is the contribution due to the presence of the patch. The probe self-impedance accounts for the finite radius of the probe and hence can be omitted when a zero-thickness probe is assumed. Accordingly, the driving point impedance may be found by calculating the voltage between the patch and the cavity base

$$Z_{in} = Z_D = -\frac{1}{I_o^2} \int_V \vec{E}(\rho,\phi,z) \cdot \vec{J}^{int}(\rho,\phi,z)\rho d\rho d\phi dz \qquad (9)$$

where the impressed current is given by (4), $V_i$ refers to the volume of the finite element which contains the probe-feed, $\vec{E}(\rho,\phi,z)$ is the interior field and $I_o$ is the constant current impressed upon the probe. Substituting (4) into (9), for the cylindrical edge elements presented in [8], it follows that the input impedance if given by

$$Z_{in} = \sum_{i=1}^{4} Z_{in}^i \qquad (10)$$

where

$$Z_{in}^i = -\frac{E(i)}{I_o} \frac{\tilde{s}_i \rho_b^i}{\alpha_i h_i} \ln\left(\frac{\rho_b}{\rho_a}\right) \left[\left(\phi_s - \tilde{\phi}_i\right)\left(z_s - \tilde{z}_i\right)\right] \qquad (11)$$

is the contribution due to one of the four radial edges of the element containing the probe.

# 3 Results

Two types of antenna elements are considered in this paper and they are shown in figure 2 where each patch is $a\alpha^o \times b$ in size with $a$ denoting the radius of the cylinder. Although the FE-BI method permits mixed-mode feeding, for this paper it is convenient to consider only the two lowest order non-hybrid modes. A patch whose radiating side walls are axially oriented is termed an axially polarized patch and is fed at $\phi_s = \frac{\alpha}{2}$. Circumferentially (or azimuthally) polarized patches have radiating walls forming constant z-surfaces and are typically fed at $z_s = \frac{b}{2}$. The $\theta = 90^o$ cut is the E-plane for circumferentially polarized patches and the H-plane for axially polarized
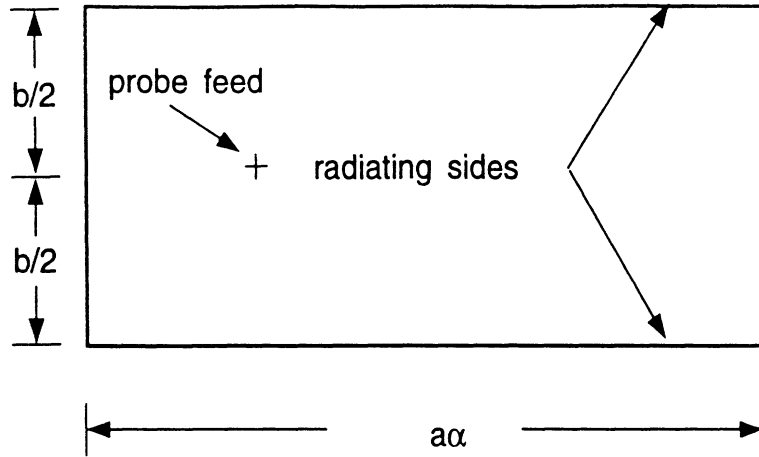
**(a)**
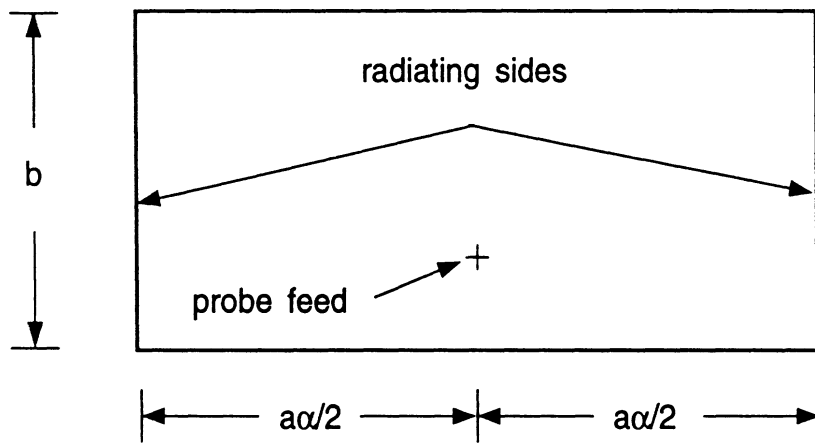


**(b)**

Figure 2: Illustration of (a) a circumferentially polarized·patch element; and
(b) an axially polarized patch element. The radius of the cylinder is denoted
by $a$.

elements. Observation is considered in the $\theta = 90°$ cut/plane since creeping wave effects are a primary interest of this paper.

Several computed and measured antenna patterns have been published for patches printed on a coated cylinder. One such patch, which is 3.5 cm × 3.5 cm, was used by Sohtell [11] to compare the accuracy of the cavity model [4] to a surface current integral equation [5]. The measured data was taken at 2.615 GHz for a metallic cylinder which was 63.5 cm long and had a radius of 14.95 cm. The cylinder was coated with a 0.3175 cm uniform dielectric having relative permittivity of $\epsilon_r = 2.32$. Data was taken for $-180° \le \phi \le 180°$ in the $\theta = 90°$ plane. Figure 3 compares these measured patterns with data generated using the FE-BI method for an identical patch placed within a $360° \times 7$ cm cavity. This wraparound cavity was chosen to simulate the coated physical test body. Note that the H-plane patterns are symmetric due to the symmetric placement of the feed, whereas the E-plane patterns are not symmetric. The placement of the feed was not specified in [11]; however, the agreement for the E-plane pattern shown in figure 3 indicates that the position used in the FE-BI model ($a\phi_s$ = -1 cm) is reasonable. The feed was placed at $z_s$ = -1 cm for the axially polarized (H-plane) case.

We next consider patch arrays. Being a rigorous method, the FE-BI formulation accounts for mutual coupling and cavity termination effects. The H-plane pattern of a four element array was measured to gauge the accuracy of the FE-BI approach. Each element is 2 cm × 3 cm and placed within a 5 cm × 6 cm × 0.07874 cm cavity which is filled with a dielectric having $\epsilon_r = 2.17$. The cylinder is 91.44 cm long and has a radius of 15.24 cm. The cavities are placed symmetrically around the cylinder (e.g. a patch is centered at $0°$, $90°$, $180°$ and $270°$). Only the patch centered at $0°$ was excited while the remaining patches were terminated with a $50\Omega$ load. The driven patch was axially polarized and the feed was located at $z_s$ = $-0.375$ cm. Figure 4 illustrates the excellent agreement between the FE-BI formulation and the measured data.

In a previous paper [8], discrete wraparound cavity arrays were found to have a significantly lower radar cross section (RCS) compared to a continuous wraparound cavity array. Thus, the size of the cavity had a significant effect on the scattering properties of the array. The two antennas presented by Sohtell [11] were placed within individual cavities which were 7 cm high and approximately $30°$, $50°$, $90°$, $180°$, $270°$ or $360°$ in angular extent. Figure 5 illustrates that the azimuthal cavity size has little effect on the radiation
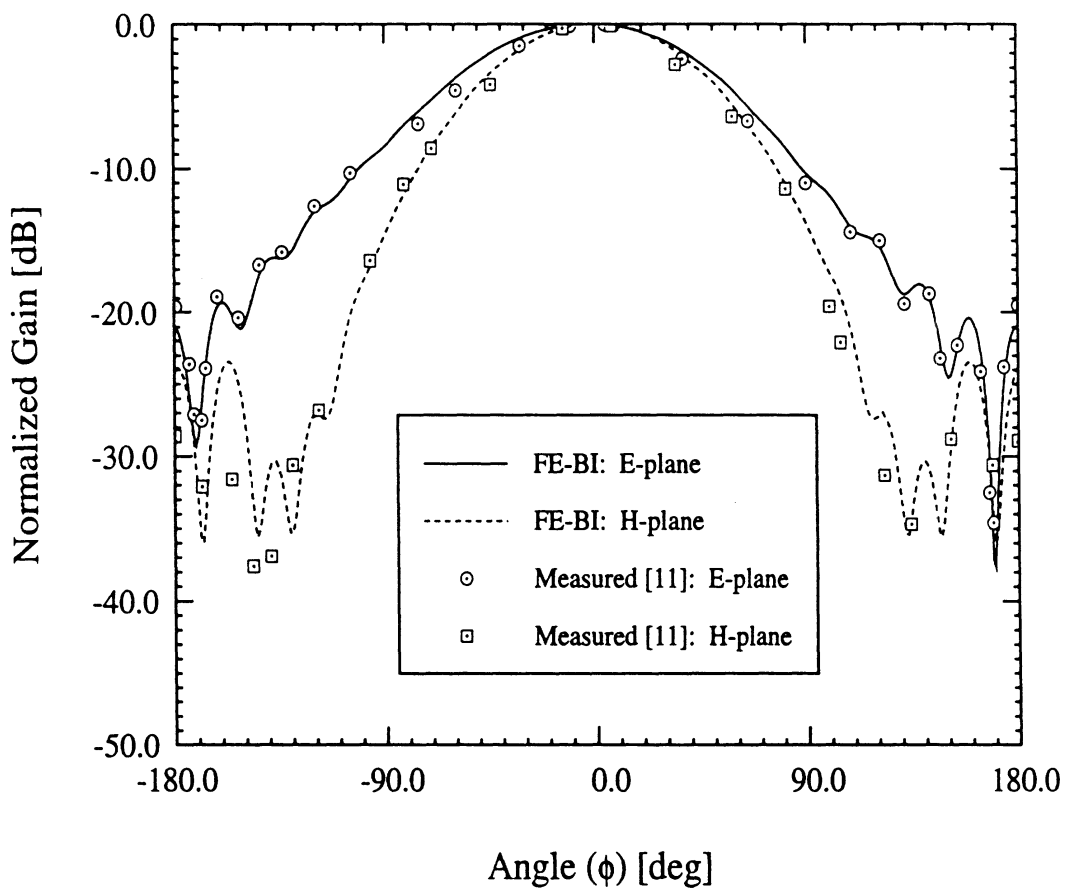
Figure 3: Comparison of measured and computed data for a circumferentially polarized element (E-plane) and an axially polarized element (H-plane). The antenna (3.5 cm × 3.5 cm ) was printed on a 14.95 cm cylinder with a 0.3175 cm coating ($\epsilon_r$ = 2.32). The probe feed was place at $(a\phi_s, z_s)$ = (-1.0,0.0) for the circumferentially polarized patch and at $(a\phi_s, z_s)$ = (0.0,-1.0) for the axially polarized antenna.
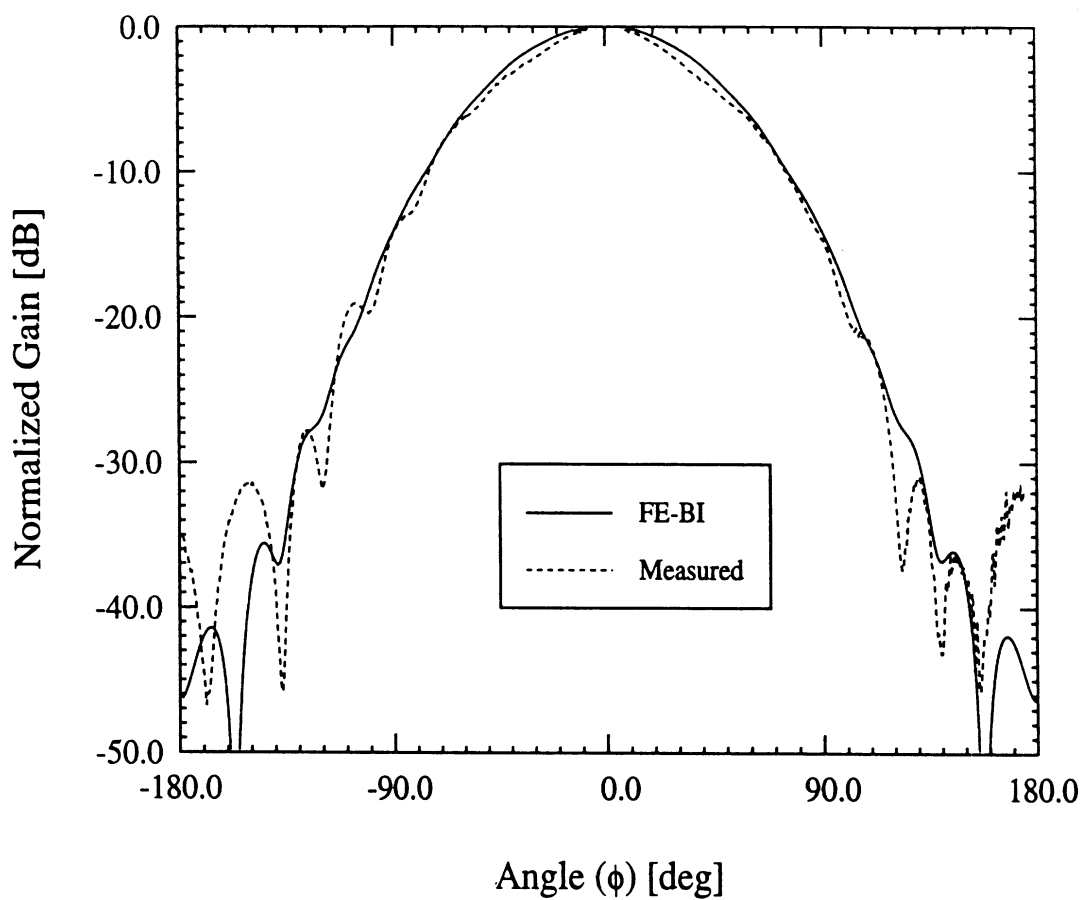
15

Figure 4: H-plane pattern for a four element patch array. Each patch is 2 cm × 3 cm and the patches are placed symmetrically around the cylinder. Only the patch centered at 0° is fed while the other patches are terminated with 50Ω loads.
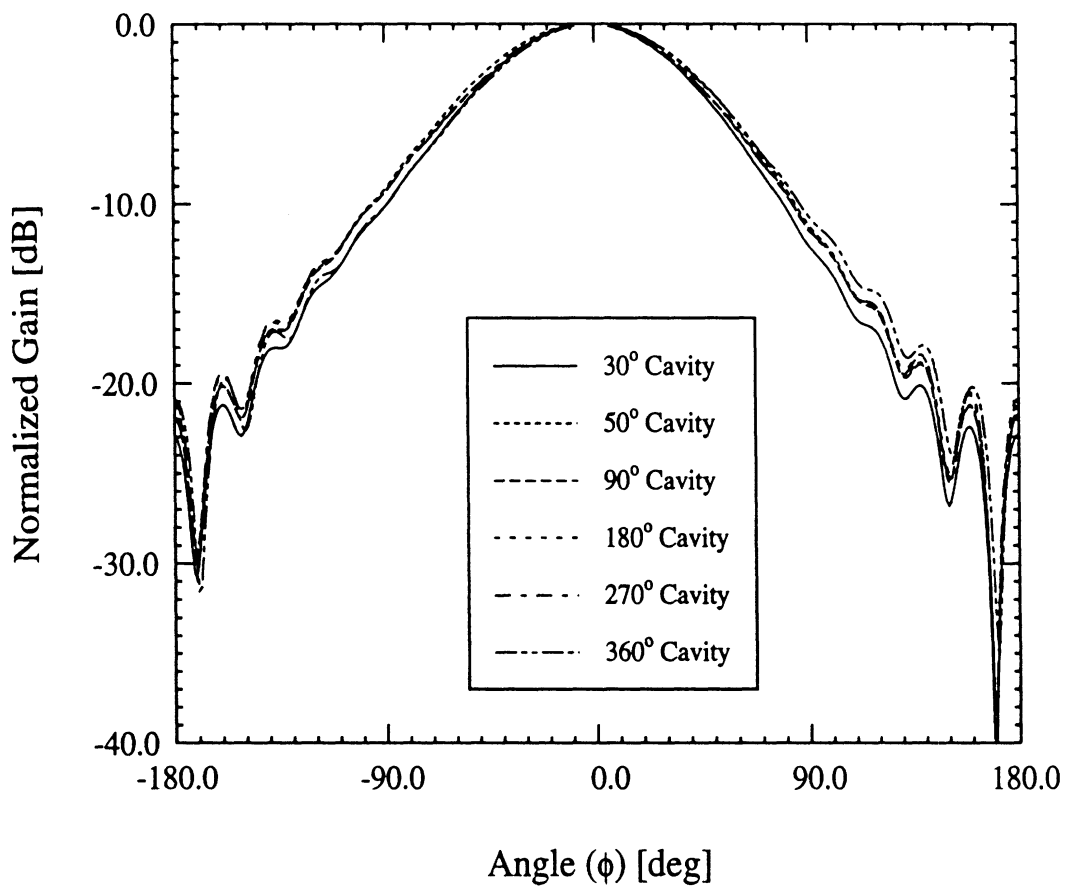
16

Figure 5: Effect of cavity size on the E-plane radiation pattern of a circum-ferentially polarized patch antenna.

pattern for a circumferentially polarized element and a similar comparison for the axially polarized patch is shown in figure 6. The back lobe of the antenna (near $\phi = 180^{\circ}$) is very small for cavities less than $180^{\circ}$ but increases for larger cavities. For cavities which lie solely on the forward face of the cylinder, the substrate modes apparently diffract off the cavity walls; an effect which has little influence on the main lobe of the pattern. However, for wraparound cavities and cavities which extend into the back side of the cylinder, the substrate modes either shed like creeping waves or diffract strongly behind the cylinder thus giving rise to the back lobe.

Having examined the effect of cavity size on the radiation patterns, we will now look at the effect of curvature on the gain of patch antennas on cylindrical platforms near resonance. Each of the two antennas used above were separately placed within 10.5 cm × 10.5 cm cavities which were embedded in cylinders with increasing radius. The frequency was allowed to vary from 2.4 GHz to 2.7 GHz and the gain (7) was recorded every 5 MHz. Figure 7 illustrates that the gain decreases with increasing element curvature for a circumferentially polarized patch. Since the input impedance is only slightly affected by curvature as shown in figure 8 the resulting decrease in gain implies a decreased radiated power which is expected since the effective aperture area observed normal to the patch is reduced as the curvature increases. The axially polarized patch exhibits a greater decrease in gain with increasing curvature as shown in figure 9. For this polarization, the input impedance is affected by curvature as shown in figure 10. The enhanced sensitivity of the axially polarized antenna is due to the combined effects of a decreased radiated power and driving point impedance. Both antennas exhibit a small decrease in resonant frequency (less than 1.5 percent) with increasing curvature as illustrated by the rotation of the curves in figures 8 and 10.

The radiation pattern of a circumferentially polarized antenna at resonance exhibits reduced creeping wave interactions with decreasing curvature due to attenuation as shown in figure 11 when excited at a resonant frequency. For circumferentially polarized E-plane observation, the radiating surface fields are aligned along the $\hat{\phi}$-axis which results in little pattern broadening. The radiation pattern of the axially polarized antenna broadens as the curvature increases which is illustrated in figure 12. Since the radiating aperture fields are aligned along the $\hat{z}$-axis for axially polarized H-plane observation, the pattern exhibits broadening due to the orientation of the
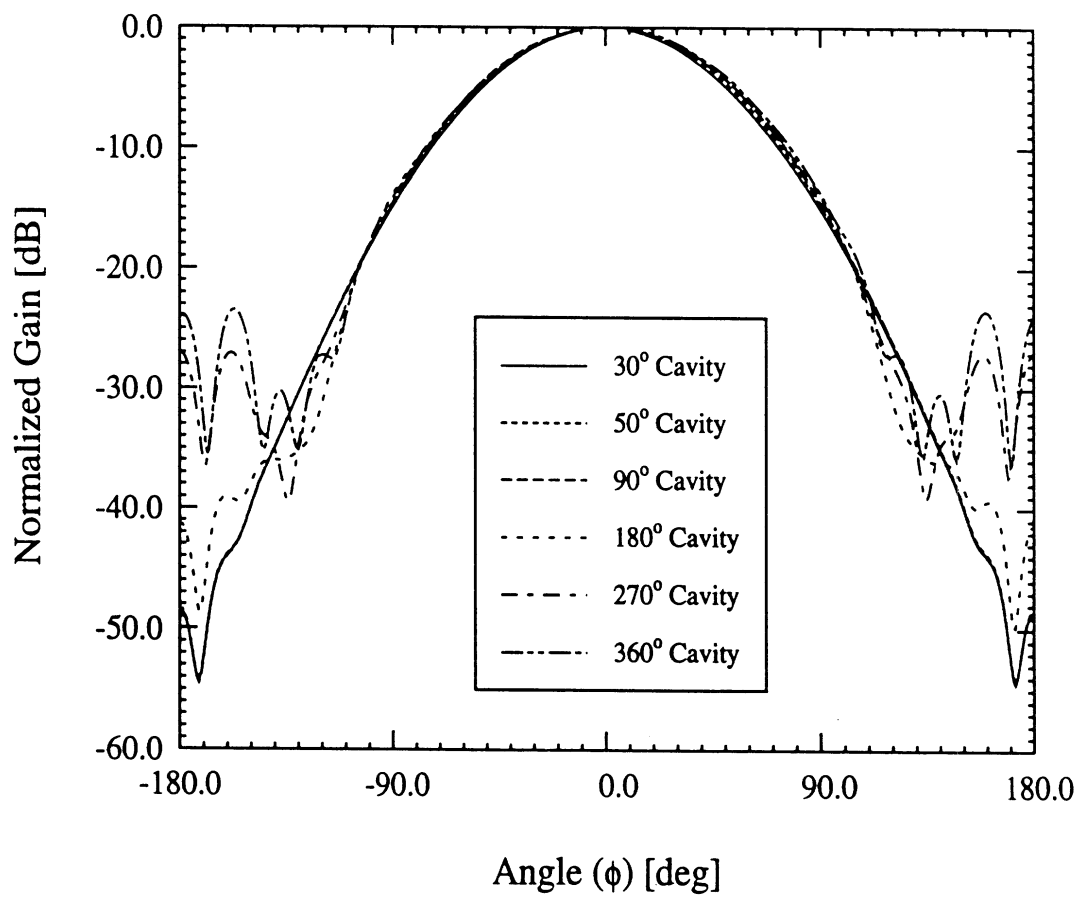
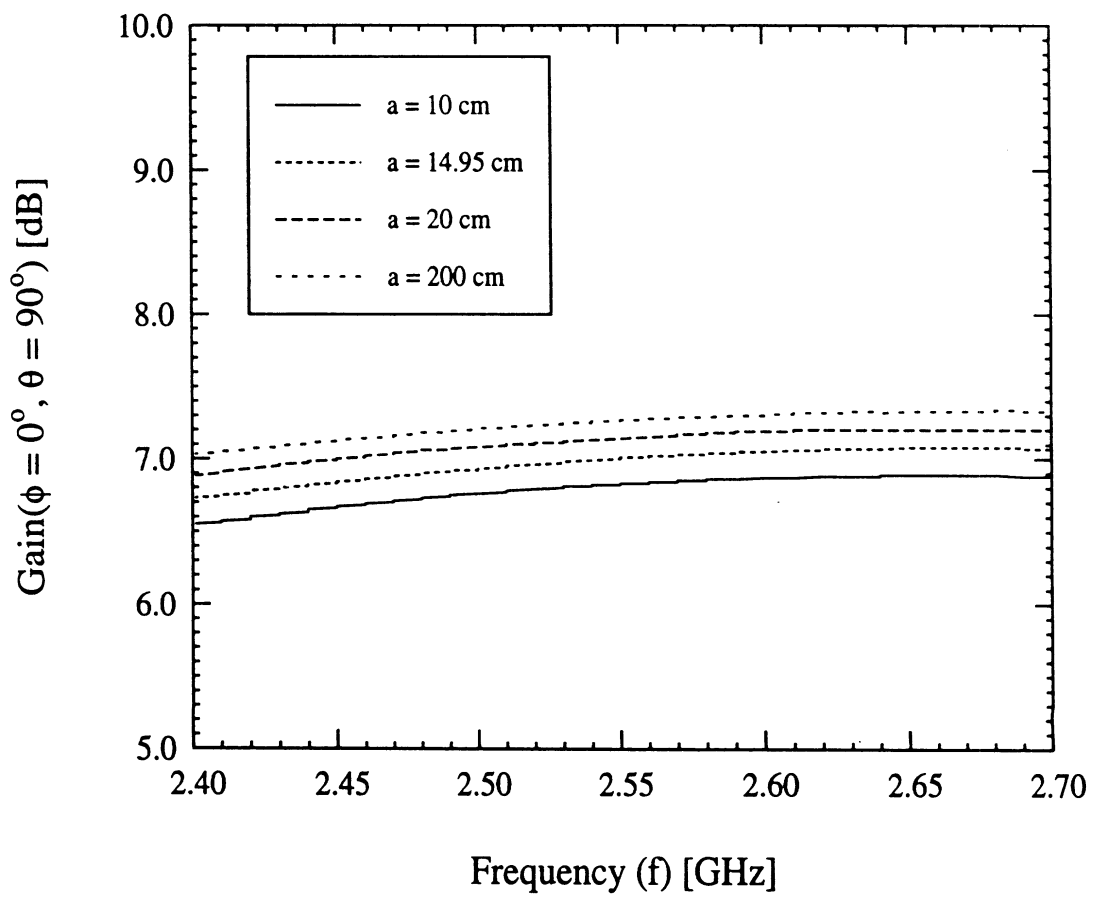Figure 6: Effect of cavity size on the H-plane radiation pattern of an axially polarized patch antenna.

Figure 7: Gain (7) of a circumferentially polarized patch antenna near resonance for various cylinder radii.
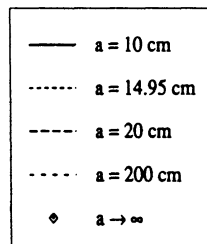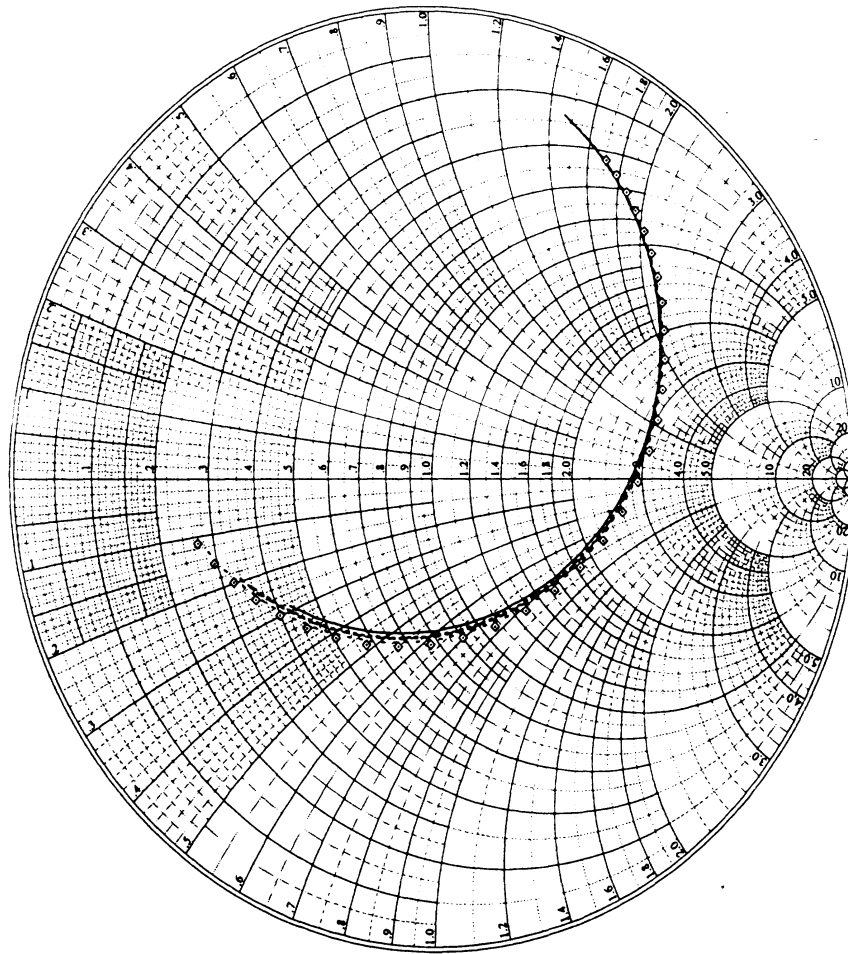
Figure 8: Input impedance of a circumferentially polarized patch antenna for various cylinder radii. The frequency range was 2.4 GHz to 2.7 GHz and the cavity size was 10.5 cm × 10.5 cm.

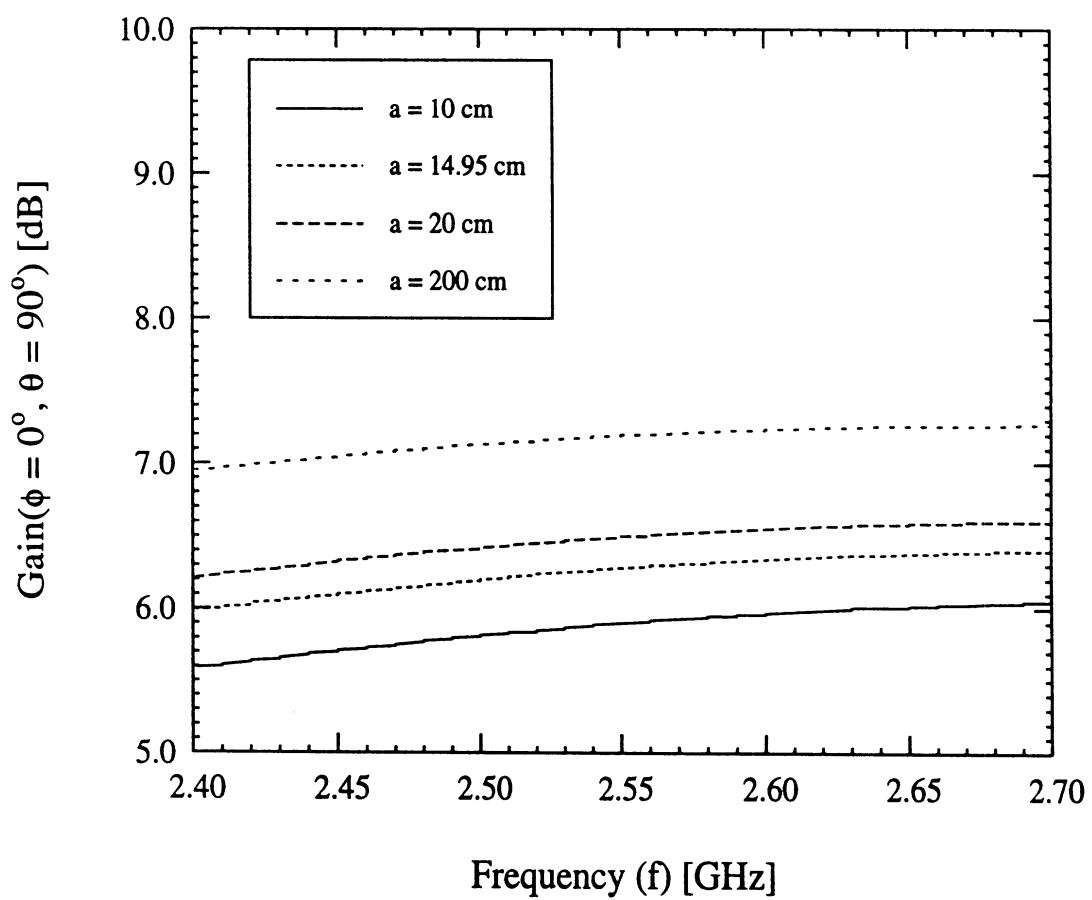Figure 9: Gain (7) of an axially polarized patch antenna near resonance for various cylinder radii.

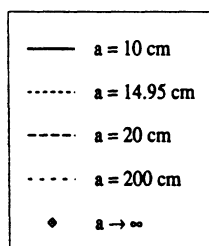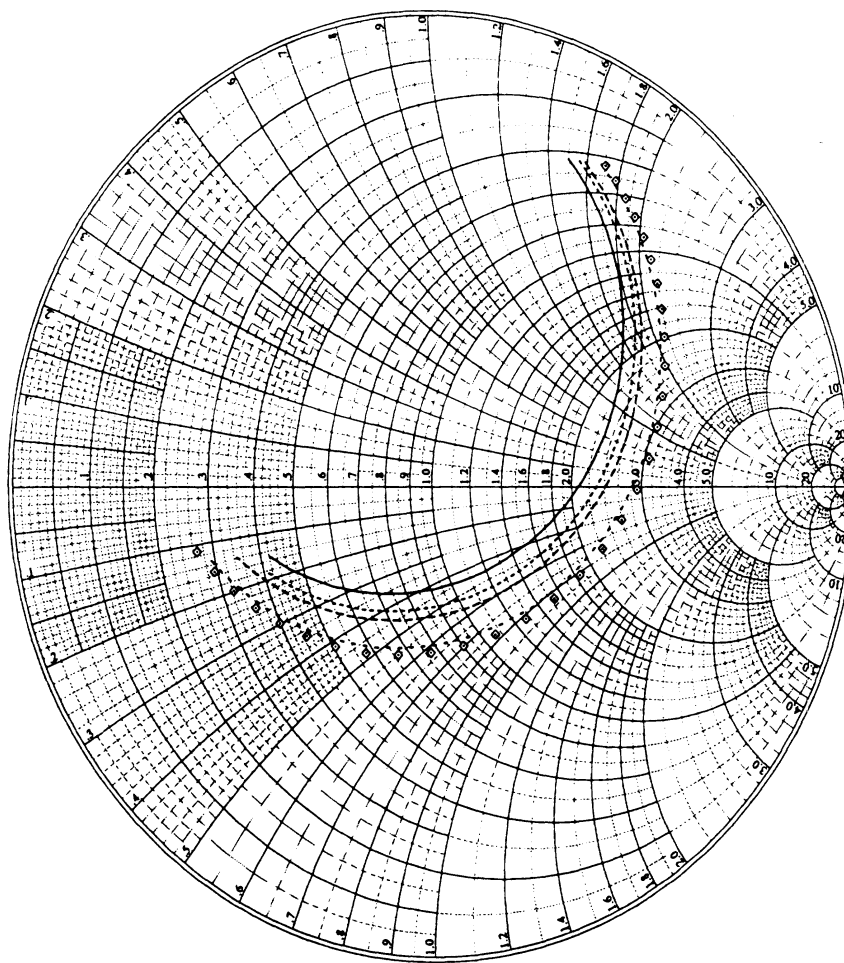Figure 10: Input impedance of an axially polarized patch antenna for various cylinder radii. The frequency range was 2.4 GHz to 2.7 GHz and the cavity size was 10.5 cm × 10.5 cm.
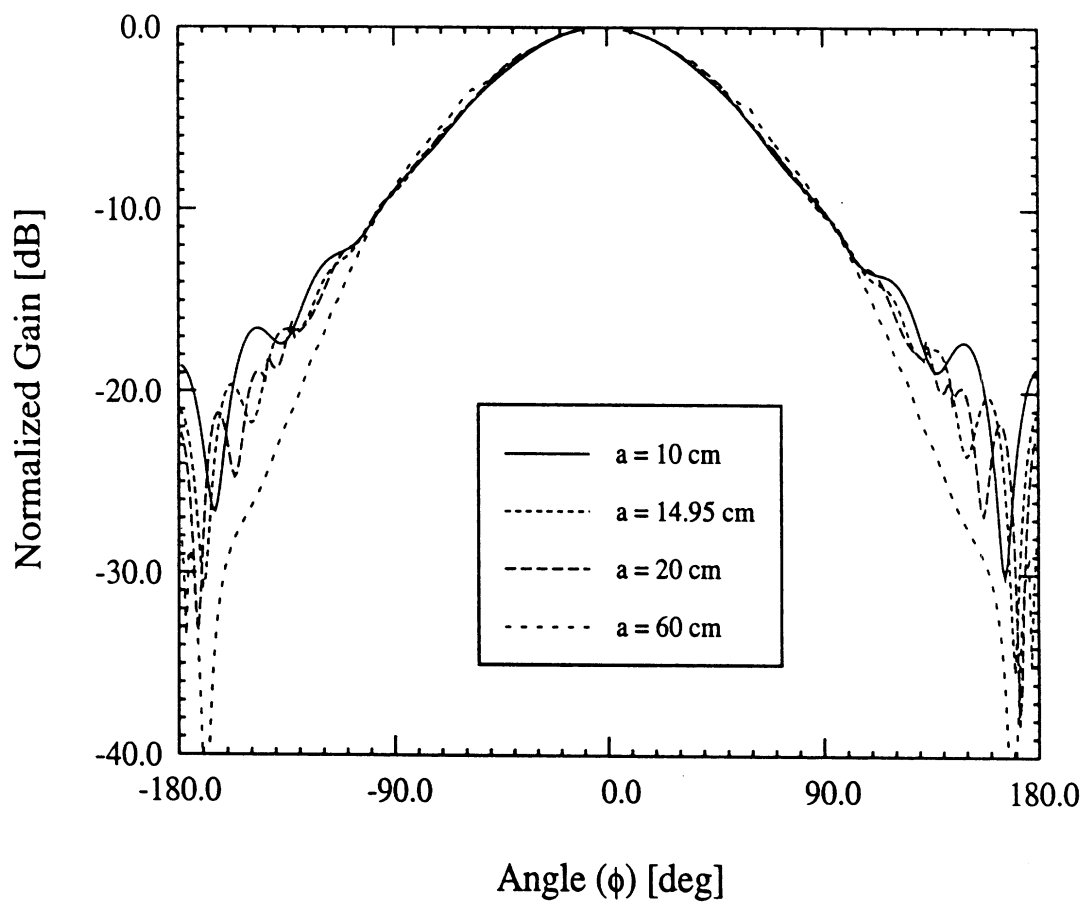
Figure 11: Variation of the radiation pattern shape with respect to curvature for a circumferentially polarized antenna.
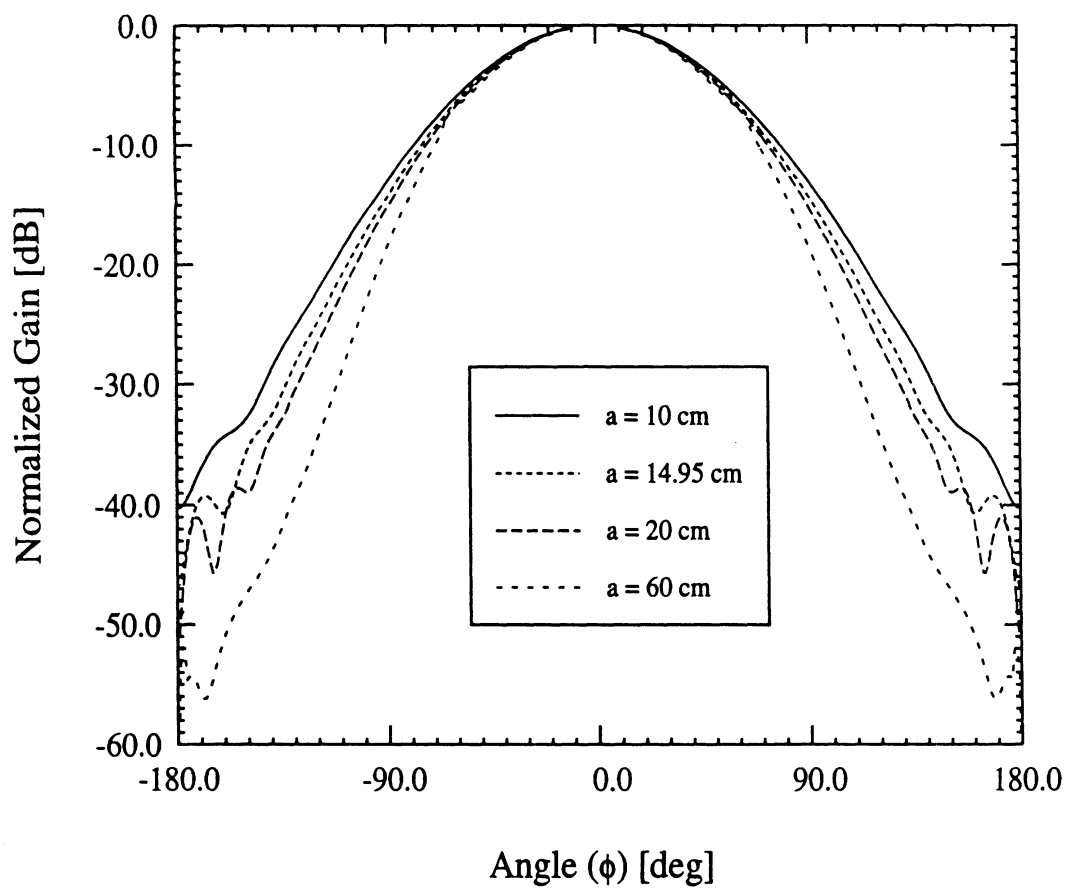
Figure 12: Variation of the radiation pattern shape with respect to curvature for an axially polarized antenna.

surface field with respect to the observation direction.

# 4  Conclusions

In this paper, we presented a rigorous analysis of the radiation by individual and arrays of patches placed in a cavity recessed in a cylindrical platform. A finite element-boundary integral code was developed and the data generated by this code for a typical cylindrical-rectangular patches were found to compare favorably with measurements. Since the cavity model does not include mutual coupling and the usual integral equation formulations requires large storage and computational resources, the FE-BI formulation is especially attractive for array analysis.

This FE-BI method was used to study the radiation properties of circumferentially and axially polarized patch antennas. The finite cavity size was found to have little effect on the circumferentially polarized E-plane pattern. However, for the H-plane pattern of an axially polarized element, the back lobe is significantly larger for cavities which extend from the front side to the back side of the cylinder. A wraparound antenna exhibited the largest back lobe implying that this lobe is a result of creeping wave shedding rather than diffraction off the lateral metallic walls of the cavity. The presence of a back lobe must be considered when designing low observable, jam-resistant antennas or antennas on complex platforms (e.g. an antenna near an obstruction). Thus, as was the case for scattering reduction, it is advisable to configure the patch antenna in the smallest possible cavity.

The effect of curvature on resonance, gain, radiation pattern shape and input impedance was studied. Both circumferentially and axially polarized antennas were considered and was found that the resonant frequency increased with increasing curvature for both antennas. The gain of both types of patch antennas decreased with increasing curvature with the axially polarized antenna exhibiting greater sensitivity attributed to the orientation of the radiating surface fields and the decreasing driving point impedance. The radiation pattern for axially polarized antennas broadens with increasing curvature while the corresponding patterns for circumferentially polarized antennas does not broaden; however, creeping wave interactions are reduced for the latter element with decreasing curvature as expected. We conclude that axially polarized antennas exhibit more sensitivity to curvature as compared

to their circumferentially polarized counterparts.

# References

[1] Y.T. Lo, D. Solomon and W.F. Richards, "Theory and experiments on microstrip antennas," *IEEE Trans. Antennas and Propagat.*, Vol. 27, pp. 137-145, 1979.

[2] D.M. Pozar and S.M. Voda, "A rigorous analysis of a microstripline fed patch antenna," *IEEE Antennas Propagat.*, Vol. 35, pp. 1343-1350, Dec. 1987.

[3] J.R. James and G.J. Wilson, "Microstrip antennas and arrays, Pt. 1 – Fundamental action and limitations," *IEE J. Microwaves, Optics, and Acoustics*, Vol. 1, pp. 165-174, 1977.

[4] J.S. Dahele, R.J. Mitchell, K.M. Luk and K.F. Lee, "Effect of curvature on characteristics of rectangular patch antenna," *Electronics Letters*, Vol 23, pp. 748-749, 2 July 1987.

[5] J. Ashkenazy, S. Shtrikman and D. Treves, "Electric surface current model for the analysis of microstrip antennas on cylindrical bodies," *IEEE Antennas Propagat.*, Vol. 33, pp. 295-300, Mar. 1985.

[6] J. T. Aberle and F. Zavosh, "Analysis of probe-fed circular microstrip patches backed by circular cavities," *Electromagnetics*, Vol. 14, pp. 239-258, Mar-Apr 1994.

[7] J-M Jin and J.L. Volakis, "A hybrid finite element method for scattering and radiation by microstrip patch antennas and arrays residing in a cavity," *IEEE Trans. Antennas and Propagat.*, Vol. 39, No. 11, pp. 1598-1604, Nov. 1991.

[8] L.C. Kempel and J.L. Volakis, "Scattering by cavity-backed antennas on a circular cylinder," *IEEE Trans. Antennas and Propagat.*, 1994 (in press).

[9] J.L. Volakis, A. Chatterjee and J. Gong, "A review of the finite element method for three-dimensional electromagnetic scattering," *J. Opt. Soc. Am. - A*, pp. 1422-1433, Apr. 1994.

[10] T.M. Hashaby, S.M. Ali and J.A. Kong, "Input impedance and radiation pattern of cylindrical-rectangular and wraparound microstrip antennas," *IEEE Trans. Antennas and Propagat.*, Vol. 38, No. 5, pp. 722-731, May 1990.

[11] E.V. Sohtell, "Microstrip antennas on a cylindrical surface," in *Handbook of microstrip antennas*, Ed. J.R. James and P.S. Hall, Peregrinus: London, pp. 1227-1255, 1989.

[12] K-M Luk, K-F Lee and J.S. Dahele, "Analysis of the cylindrical-rectangular patch antenna," *IEEE Trans. Antennas and Propagat.*, Vol. 37, No. 2, pp. 143-147, Feb. 1989.

# Scattering by Cavity-Backed Antennas on a Circular Cylinder

Leo C. Kempel, *Student Member, IEEE*, and John L. Volakis, *Senior Member, IEEE*

*Abstract*—Conformal arrays are popular antennas for aircraft, spacecraft, and land vehicle platforms due to their inherent low weight, drag, and observables. However, to date there has been a dearth of rigorous analytical or numerical solutions to aid the designer. In fact, it has been common practice to use limited measurements and planar approximations in designing such nonplanar antennas. In this paper, we extend the finite element–boundary integral method to scattering by cavity-backed structures in an infinite, metallic cylinder. In particular, we discuss the formulation specifics, such as weight functions, dyadic Green's function, implementation details, and particular difficulties inherent to cylindrical structures. Special care is taken to ensure that the resulting computer program has low memory demand and minimal computational requirements. Scattering results are presented and validated as much as possible.

## I. INTRODUCTION

CONFORMAL antenna arrays are attractive for aircraft, spacecraft, and land vehicle applications since these antenna systems have low weight, low drag, flexibility, and cost advantages over conventional protruding antennas. The majority of previous studies pertaining to nonplanar conformal antennas has been conducted experimentally due to a dearth of rigorous analysis techniques. Traditional rigorous techniques involve an integral equation and are limited in terms of radius of curvature and structural complexity. Some approximate methods have been considered, but these are restricted in accuracy and element shape.

Recently, the finite element–boundary integral (FE-BI) method was successfully employed for scattering analysis of large cavity-backed planar arrays [1]. The resulting system is sparse due to the local nature of the finite element method, whereas the boundary integral submatrix is fully populated. However, by resorting to an iterative solver such as the Biconjugate Gradient (BiCG) method, the boundary integral subsystem may be cast in circulant form, allowing use of the Fast Fourier Transform (FFT) in performing the matrix-vector products. This BiCG-FFT solution scheme ensures $\mathcal{O}(N)$ memory demand for the entire FE-BI system and minimizes the computational requirements.

In this paper, the FE-BI formulation is extended to scattering by aperture antennas conformal to a cylindrical metallic surface. In contrast to the planar aperture array, the implementation of the cylindrically conformal array requires shell-shaped elements rather than bricks, and the required external

Green's function must satisfy the boundary conditions on the surface of the cylinder. In its exact form, this Green's function is an infinite series that imposes unacceptable computational burdens on the method. However, for large-radius cylinders, a suitable asymptotic formula is available and herein used for an efficient evaluation of the Green's function. In addition, the resulting BI system is again cast in circulant form to ensure an $\mathcal{O}(N)$ memory demand and to take advantage of the FFT's efficiency when carrying out the matrix-vector product.

A primary difficulty in studying cavity-backed antennas mounted on curved surfaces is the lack of reference data. In this paper, scattering calculations based on the FE-BI method are compared with data based on different techniques. Although such validation is necessarily limited, it provides confidence in the formulation's accuracy so that this approach may be used in extending the available reference data.

An alternative approach for terminating the FE mesh is to use an absorbing boundary condition rather than the exact boundary integral used herein. The finite element-absorbing boundary condition (FE-ABC) method is associated with a higher CPU cost because of its enlarged computational domain; however, it is more flexible than the FE-BI method presented in this paper since it may include a complex radome as well as the cavity-backed antenna elements. Such an FE-ABC formulation will be the subject of a future paper.

## II. FE-BI FOR CIRCULAR CYLINDERS

In this section, the FE-BI formulation is developed for cavities recessed in an infinite metallic cylinder, having walls that coincide with constant $\rho$-, $\phi$- or $z$-surfaces (see Fig. 1).

As usual, the finite element formulation permits substantial modeling flexibility, including cavity inhomogeneities, lumped loads, super/substrate antenna configurations, or microstrip lines and so on.

The FE-BI approach possesses both low memory and computational demand when implemented with a BiCG-FFT solver. Although the system of equations associated with the FE formulation is sparse, the boundary integral submatrix is fully populated. However, if the aperture mesh is a uniform grid, the BiCG-FFT solver may be employed for that portion of the system, thus retaining $\mathcal{O}(N)$ memory demand for the entire system. In addition, the solver has low computational demand since the sparse matrix-vector
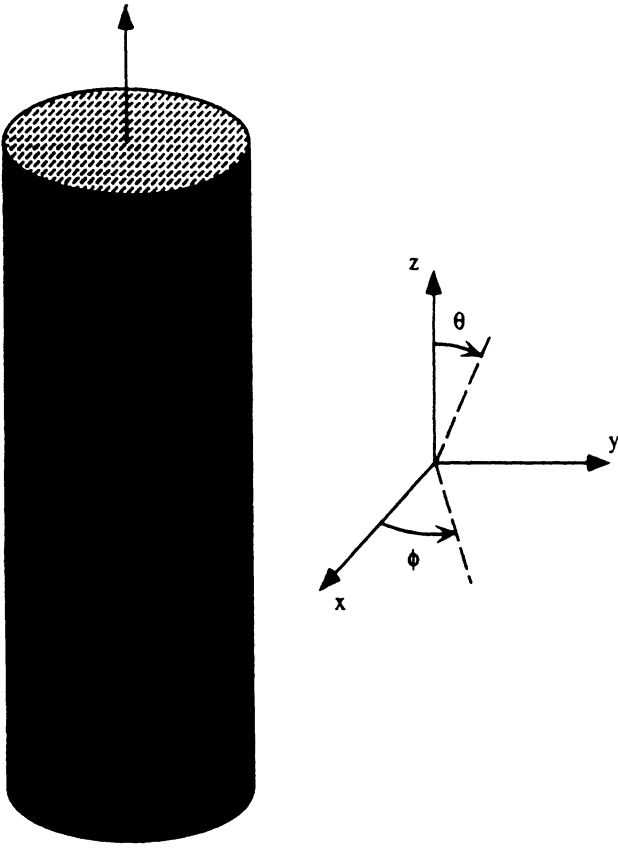
Fig. 1. Illustration of a typical cavity-backed antenna situated on a metallic cylinder and the associated coordinate system.

products require $\mathcal{O}(N)$ operations per iteration and the discrete convolutions that utilize FFTs require only $\mathcal{O}(N\log N)$ operations per iteration.

The FE-BI formulation begins with the weak form of the vector wave equation followed by specification of appropriate vector shape functions and a dyadic Green's function. The resulting FE-BI equations are then used to solve for the total electric fields within the cavity and on the aperture (see, for example, Volakis *et al.* [2]). For the specific configuration at hand, the weak form of the wave equation can be written as

$$
\int_{V_i} \left\{ \frac{\nabla \times \vec{W}_j(\rho.\phi.z) \cdot \nabla \times \vec{W}_i(\rho,\phi,z)}{\mu_r(\rho,\phi,z)} \right.
$$

$$
\left. - k_o^2 \epsilon_r(\rho.\phi.z)\vec{W}_j(\rho.\phi.z) \cdot \vec{W}_i(\rho.\phi.z) \right\} \rho\,d\rho\,d\phi\,dz
$$

$$
+ (k_o a)^2 \delta_a(j)\delta_a(i) \int_{S_i} \int_{S_j} \left[ \vec{W}_i(a.\phi.z) \cdot \hat{\rho}(a.\phi.z) \times \right.
$$

$$
\left. \overline{\overline{G}}_2(a.\tilde{\phi}.\tilde{z}) \times \hat{\rho}(a.\phi'.z') \cdot \vec{W}_j(a.\phi'.z') \right] d\phi'\,dz'\,d\phi\,dz
$$

$$
= f_i^{int} + f_i^{ext}. \tag{1}
$$

In this, $\vec{W}_i$ are vector basis functions with support over the volume $V_i$, which is associated with the $i$th degree of freedom, and in a similar fashion, $S_i$ and $S_j$ represent aperture surfaces associated with the $i$th and $j$th degrees of freedom, respectively. The appropriate dyadic Green's function is denoted by $\overline{\overline{G}}_2$, and it has convolutional ($\tilde{\phi} = \phi - \phi'$,

$\tilde{z} = z - z'$) form when evaluated on the surface of the cylinder $\rho = a$. The unprimed coordinates represent the test point, while the primed ones denote the source point. The free-space propagation constant is given by $k_0 = \frac{2\pi}{\lambda_0}$, where $\lambda_0$ is the free-space wavelength. The cavity is filled with an inhomogeneous material having relative constitutive properties $\epsilon_r$ and $\mu_r$. The function $\delta_a(i)\delta_a(j)$ is the product of two Kronecker delta functions. Hence, it identifies which pairs of unknowns belong to the aperture and accordingly contribute to the boundary integral submatrix. The right-hand side contains an internal source ($f_i^{int}$) and an external source ($f_i^{ext}$) term. The former is used only for radiation analysis and is omitted for this paper. The latter is used for scattering analysis and is discussed later.

The FE-BI equation (1) may be rewritten in matrix form as

$$
\left[\mathcal{A}\right]\begin{Bmatrix} \{E_j^{ap}\} \\ \{E_j^{int}\} \end{Bmatrix} + \begin{bmatrix} [\mathcal{G}] & [0] \\ [0] & [0] \end{bmatrix}\begin{Bmatrix} \{E_j^{ap}\} \\ \{E_j^{int}\} \end{Bmatrix} = \begin{Bmatrix} \{f_i^{ext}\} \\ \{0\} \end{Bmatrix} \tag{2}
$$

where the entries of $[\mathcal{A}]$ are due to the FE portion of the formulation and $[\mathcal{G}]$ is the boundary integral submatrix. In (2), $E_j^{ap}$ and $E_j^{int}$ denote degrees of freedom associated with the aperture and interior fields, respectively.

An important factor in choosing the finite elements for gridding the cavity is the element's suitability for satisfying the mathematical requirements of the formulation as well as the physical features of the antenna system. Traditional node-based finite elements associate the degrees of freedom with the nodal fields and have proven unsatisfactory for three-dimensional electromagnetics applications since they do not correctly represent the null space of the curl operator, and hence spurious modes are generated [3]–[4]. In contrast, edge-based elements correctly model the curl operator and therefore the electromagnetic fields. In addition, edge-based elements avoid explicit specification of the fields at corners where edge conditions may require a singularity. Jin and Volakis [6] presented edge-based brick elements, which are convenient for rectangular-type structures and cavities. For cavities residing in a circular cylinder, shell elements are the natural choice.

Cylindrical shell elements possess both geometrical fidelity and simplicity for cylindrical-rectangular cavities. Fig. 2 illustrates a typical shell element, which has eight nodes connected by twelve edges: four edges aligned along each of the three orthogonal directions of the cylindrical coordinate system. Each element is associated with twelve vector shape functions given by

$$
\vec{W}_{12}(\rho,\phi,z) = \vec{W}_\rho(\rho.\phi.z: \cdot.\phi_r.z_t.+).
$$

$$
\vec{W}_{43}(\rho.\phi,z) = \vec{W}_\rho(\rho.\phi.z: \cdot.\phi_l.z_t.-)
$$

$$
\vec{W}_{56}(\rho.\phi.z) = \vec{W}_\rho(\rho.\phi.z: \cdot.\phi_r.z_b.-).
$$

$$
\vec{W}_{87}(\rho.\phi.z) = \vec{W}_\rho(\rho.\phi.z: \cdot.\phi_l.z_b.+)
$$

$$
\vec{W}_{14}(\rho.\phi.z) = \vec{W}_\phi(\rho.\phi.z: \rho_b. \cdot.z_t.+).
$$

$$
\vec{W}_{23}(\rho.\phi.z) = \vec{W}_\phi(\rho.\phi.z: \rho_a. \cdot.z_t.-)
$$

$$
\vec{W}_{58}(\rho.\phi.z) = \vec{W}_\phi(\rho.\phi.z: \rho_b. \cdot.z_b.-).
$$

$$
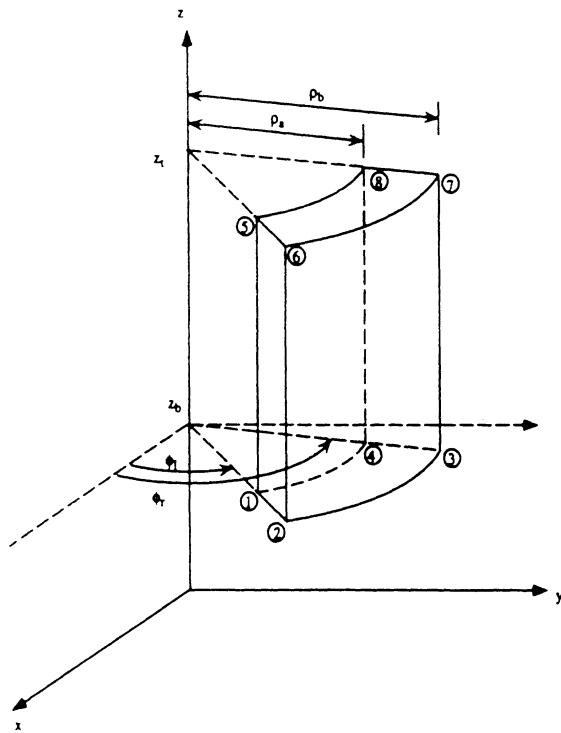\vec{W}_{67}(\rho.\phi.z) = \vec{W}_\phi(\rho.\phi.z: \rho_a. \cdot.z_b.+)
$$

31

Fig. 2. Cylindrical shell element.

$$\vec{W}_{15}(\rho, \phi, z) = \vec{W}_z(\rho, \phi, z; \rho_b, \phi_r, \cdot, +),$$

$$\vec{W}_{26}(\rho, \phi, z) = \vec{W}_z(\rho, \phi, z; \rho_a, \phi_r, \cdot, -)$$

$$\vec{W}_{48}(\rho, \phi, z) = \vec{W}_z(\rho, \phi, z; \rho_b, \phi_l, \cdot, -),$$

$$\vec{W}_{37}(\rho, \phi, z) = \vec{W}_z(\rho, \phi, z; \rho_a, \phi_l, \cdot, +) \qquad (3)$$

where $\vec{W}_{lk}$ is associated with the edge which is delimited by local nodes $(l, k)$, as shown in Fig. 2. As seen from (3), three fundamental vector weight functions are required for the complete representation of the shell element. They are

$$\vec{W}_\rho(\rho, \phi, z; \tilde{\rho}, \tilde{\phi}, \tilde{z}, \tilde{s}) = \frac{\tilde{s}\rho_b}{\alpha h} \frac{(\phi - \tilde{\phi})(z - \tilde{z})}{\rho} \hat{\rho}$$

$$\vec{W}_\Phi(\rho, \phi, z; \tilde{\rho}, \tilde{\phi}, \tilde{z}, \tilde{s}) = \frac{\tilde{s}}{th}(\rho - \tilde{\rho})(z - \tilde{z})\hat{\phi}$$

$$\vec{W}_z(\rho, \phi, z; \tilde{\rho}, \tilde{\phi}, \tilde{z}, \tilde{s}) = \frac{\tilde{s}}{t\alpha}(\rho - \tilde{\rho})(\phi - \tilde{\phi})\hat{z} \qquad (4)$$

where the element parameters $(\rho_a, \rho_b, \phi_l, \phi_r, z_b, z_t)$ are shown in Fig. 2, $t = \rho_b - \rho_a$, $\alpha = \phi_r - \phi_l$, and $h = z_t - z_b$. Each local edge is distinguished by $\tilde{\rho}$, $\tilde{\phi}$, $\tilde{z}$, and $\tilde{s}$ as given in (3). The $\frac{1}{\rho}$-term, which appears in the definition of the $\tilde{\rho}$-directed weight (4), is essential in satisfying the divergence free requirement, i.e., so that $\nabla \cdot \vec{W}_j = 0$.[1] Note that as the radius of the cylinder becomes large, the curvature of these elements decreases, resulting in weight functions that are functionally similar to the bricks presented by Jin and Volakis [6]. Having specified the vector basis functions, we may proceed to develop the matrix entries for the system (2).

The FE-BI system is composed of two parts: a sparse FE matrix and a fully populated BI submatrix, as shown in (2).

[1] $\vec{W}_j(\rho, \phi, z)$ will satisfy this requirement only within the volume of the element. These weighting functions introduce artificial charges on the faces of the element and are not divergenceless at element interfaces. This is allowable since these elements do not guarantee normal field continuity across the element faces.

The FE matrix entries are represented by

$$A_{ij} = \frac{1}{\mu_r} I_{st}^{(1)ij} - k_o^2 \epsilon_r I_{st}^{(2)ij} \qquad (5)$$

where constant material properties have been assumed within each element. The subscripts $(i, j)$ refer to the row and column of the matrix entry and correspond to the test and source edges, respectively. The auxiliary functions

$$I_{st}^{(1)ij} = \int_{V_i} \nabla \times \vec{W}_s(\rho, \phi, z; \tilde{\rho}_j, \tilde{\phi}_j, \tilde{z}_j, \tilde{s}_j)$$
$$\cdot \nabla \times \vec{W}_t(\rho, \phi, z; \tilde{\rho}_i, \tilde{\phi}_i, \tilde{z}_i, \tilde{s}_i) \rho \, d\rho \, d\phi \, dz$$

$$I_{st}^{(2)ij} = \int_{V_i} \vec{W}_s(\rho, \phi, z; \tilde{\rho}_j, \tilde{\phi}_j, \tilde{z}_j, \tilde{s}_j)$$
$$\cdot \vec{W}_t(\rho, \phi, z; \tilde{\rho}_i, \tilde{\phi}_i, \tilde{z}_i, \tilde{s}_i) \rho \, d\rho \, d\phi \, dz \qquad (6)$$

are identically zero unless both test and source edges share at least one element in common, resulting in a highly sparse system. Physically, such a system is a consequence of the locality property inherent in a partial differential equation formulation. In (6), the direction of the source and test edges are represented by $(s, t) \in \{\rho, \phi, z\}$, respectively. Since the edges of the mesh are aligned along three orthogonal directions, only six unique combinations of $(s, t)$ are required for $I^{(1)}$, and only three such combinations for $I^{(2)}$. Since (6) is symmetric with respect to source and test edges, the FE matrix will also be symmetric. Evaluations of (6) using (4) are presented in the Appendix.

A lumped impedance post may be included in the formulation by adding a term to (1) and equivalently to (5); surface or subsurface metallization layers may also be modeled. Radially oriented lumped loads are approximated in the FE-BI formulation by a filamentary load located at $(\phi_L, z_L)$ [2]. Such posts have length $l$, cross-sectional area $s$ and impedance $Z_L$. The contribution to $[A]$ is given by

$$A_{ij} = jk_o Z_o \frac{l}{sZ_L} \int_V \frac{\delta(\phi - \phi_L)\delta(z - z_L)}{\rho}$$
$$\cdot W_i(\rho, \phi, z) W_j(\rho, \phi, z) \rho \, d\rho \, d\phi \, dz \qquad (7)$$

which may be readily evaluated in closed form. In addition, infinitesimally thin metallization layers may be represented by simply fixing a priori the weight coefficients to zero for weights associated with edges which are tangential to the metal. This is a consequence of using a total electric field formulation. The symmetry and sparsity of the FE system $[A]$ is maintained after the addition of these loads, while the BI system $[G]$ remains fully populated and symmetric.

The boundary integral provides an exact boundary condition for mesh closure, and its construction relies on a cylindrical dyadic Green's function. The entries of the boundary integral submatrix are

$$G_{ij} = (k_o a)^2 \int_{S_i} \int_{S_j} W_t(a, \phi, z; \tilde{\rho}_i, \tilde{\phi}_i, \tilde{z}_i, \tilde{s}_i)$$

$$\left[ \hat{\rho}(a, \phi, z) \times \overline{\overline{G}}_2(a, \tilde{\phi}, \tilde{z}) \times \hat{\rho}(a, \phi', z') \right]$$

$$\cdot W_s(a, \phi', z'; \tilde{\rho}_j, \tilde{\phi}_j, \tilde{z}_j, \tilde{s}_j) d\phi' \, dz' \, d\phi \, dz \qquad (8)$$

$$\cdot \left\{ \left(cos^2\theta + q(1 - q)(2 - 3cos^2\theta)\right)v(\beta) \right\}$$

$$G^{\Phi z}(a, \bar{\phi}, \bar{z}) \sim \frac{jk_o}{2\pi}qe^{-jk_o s}$$

$$\cdot \sin\theta\cos\theta \left\{ (1 - 3q(1 - q)) \cdot v(\beta) \right\}$$

$$G^{\Phi\Phi}(a, \bar{\phi}, \bar{z}) \sim -\frac{jk_o}{2\pi}qe^{-jk_o s}$$

$$\cdot \left\{ \left(sin^2\theta + q(1 - q)(2 - 3sin^2\theta)\right)v(\beta) \right.$$

$$\left. + q\left[sec^2\theta(u(\beta) - v(\beta))\right] \right\} \tag{10}$$

where $\beta = ks\left[\frac{cos^2\theta}{\sqrt{2k_oa}}\right]^{\frac{2}{3}}$ and $q = \frac{j}{k_os}$ has proven quite accurate. In the definition of $\beta$, $s$ is the usual geodesic path length ($s = \sqrt{(a\bar{\Phi})^2 + z^2}$) and $\theta$ is the direction of the geodesic trajectory $\left(\theta = tan^{-1}\left[\frac{a\bar{\phi}}{z}\right]\right)$. Depending on which of the two direct paths (shown in Fig. 3) is used, $\bar{\Phi} = \bar{\phi}$ or $\bar{\Phi} = 2\pi - \bar{\phi}$. The soft and hard Fock functions, $u(\beta)$ and $v(\beta)$, respectively, are characteristic of on-surface creeping wave interactions and have been extensively investigated by Logan [13]. These functions are also presented in the appendix of this paper. Although computation of the Green's function (10) is now tractable, evaluation of (8) must be done so that a discrete convolutional system is maintained and the singularity of (8) at $s = 0$ is properly treated.

Care must be taken in evaluating (8) so that the overall storage requirement remains $\mathcal{O}(N)$ and the singular integrals of (8) are accurately computed. If uniform zoning is used, the resulting submatrix ([$\mathcal{G}$]) is block Toeplitz and hence amenable to solution using the BiCG-FFT method. For the nonself-cell contributions, midpoint integration may be used while a regularization procedure must be employed for the self-cell. Bird [12] noted that (8) recovers the metallic screen Green's function when $\beta = 0$ within the available approximation order. This suggests that (8) may be regularized by adding and subtracting from (10) the function

$$2\bar{\bar{G}}_o(a, \bar{\phi}, \bar{z}) = \left[\bar{\bar{I}} + \frac{\nabla\nabla}{k_o^2}\right]\frac{e^{-jk_oR}}{2\pi R} \quad ; \quad R = |\bar{r} - \bar{r}'| \tag{11}$$

which is the free-space dyadic Green's function multiplied by two. The resulting regularized Green's function (curvature contribution) is given by

$$\bar{G}^{zz}(a, \bar{\phi}, \bar{z}) \sim -\frac{jk_o}{2\pi}qe^{-jk_o s}\left\{ \left(cos^2\theta + q(1 - q)\right) \right.$$

$$\left. \cdot(2 - 3cos^2\theta))[v(\beta) - 1] \right\}$$

$$\bar{G}^{\Phi z}(a, \bar{\phi}, \bar{z}) \sim \frac{jk_o}{2\pi}qe^{-jk_o s}\sin\theta\cos\theta \left\{ (1 - 3q(1 - q)) \right.$$
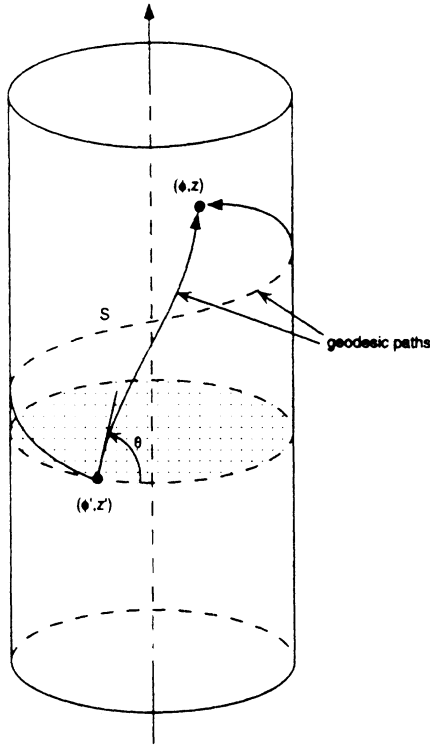
$$\left. \cdot[v(\beta) - 1] \right\}$$



Fig. 3. Geodesic paths on a circular cylinder.

where the weight functions are given by (4) and evaluated at the surface $\rho = a$. In (8), the dyadic Green's function ($\bar{\bar{G}}_2$) satisfies both the radiation condition, and the Neumann boundary condition at $\rho = a$. This dyadic Green's function may be expressed exactly [8]

$$G^{zz}(a, \bar{\phi}, \bar{z})$$

$$= -\frac{1}{(2\pi)^2}\sum_{n=-\infty}^{\infty}\int_{-\infty}^{\infty}\left(\frac{k_\rho}{k_o}\right)^2\frac{1}{\gamma}\frac{H_n^{(2)}(\gamma)}{H_n^{'(2)}(\gamma)}e^{j(n\bar{\phi}-k_z\bar{z})}dk_z$$

$$G^{\Phi z}(a, \bar{\phi}, \bar{z})$$

$$= -\frac{1}{(2\pi)^2}\sum_{n=-\infty}^{\infty}\int_{-\infty}^{\infty}\left(\frac{nk_z}{k_o^2a\gamma}\right)\frac{H_n^{(2)}(\gamma)}{H_n^{'(2)}(\gamma)}e^{j(n\bar{\phi}-k_z\bar{z})}dk_z$$

$$G^{\Phi\Phi}(a, \bar{\phi}, \bar{z})$$

$$= \frac{1}{(2\pi)^2}\sum_{n=-\infty}^{\infty}\int_{-\infty}^{\infty}\frac{1}{\gamma}$$

$$\cdot\left[\frac{H_n^{'(2)}(\gamma)}{H_n^{(2)}(\gamma)} - \left(\frac{nk_z}{k_oak_\rho}\right)^2\frac{H_n^{(2)}(\gamma)}{H_n^{'(2)}(\gamma)}\right]e^{j(n\bar{\phi}-k_z\bar{z})}dk_z \tag{9}$$

where $\gamma = k_\rho a$ and $k_\rho = \sqrt{k_o^2 - k_z^2}$. However, for large radius cylinders (e.g., $ka \geq 3$), (9) is computationally prohibitive. In these cases, which are of main concern in this paper, it is advantageous to employ an asymptotic expression for $\bar{\bar{G}}_2$ [9]-[12]. These employ a creeping wave series expansion of which only the two direct path contributions (see Fig. 3) are retained. The formula due to Pathak and Wang [9]

$$G^{zz}(a, \bar{\phi}, \bar{z}) \sim -\frac{jk_o}{2\pi}qe^{-jk_o s}$$

$$\tilde{G}^{\infty\infty}(a,\phi,z) \sim -\frac{jk_o}{2\pi}qe^{-jk_o s}\left\{ \left(sin^2\theta + q(1-q)\right. \right.$$

$$\cdot(2 - 3sin^2\theta))[v(\beta) - 1]$$

$$\left. + q[sec^2\theta(u(\beta) - v(\beta))] \right\} \tag{12}$$

and since it is no longer singular it may be evaluated numerically. The planar contribution may be calculated in the manner described previously by Jin and Volakis [5]. The FE-BI matrix has now been fully developed and it remains to specify the excitation function for external sources.

### III. PLANE WAVE EXCITATION

Plane wave excitation of the geometry is considered in this section for scattering analysis. The use of the exact boundary condition in (1) allows coupling of an exterior excitation field into the cavity. We will describe the form of the source function $f_i^{ext}$ and discuss its numerical implementation.

The forcing function, due to exterior sources $(f_i^{ext})$ is given by

$$f_i^{ext} = jZ_o k_o a \int_{S_i} \vec{W}_i(a,\phi',z') \cdot \hat{\rho}(a,\phi',z')$$

$$\times \vec{H}^{cyl}(a,\phi',z')d\phi' dz' \tag{13}$$

where $\vec{W}_i(\rho,\phi,z)$ is the testing weight for the $i$th row of the matrix and $\vec{H}^{cyl}$ represents the magnetic field on the cylinder's surface in the absence of the cavity. A plane wave

$$\vec{E}^i = \hat{e}^i e^{-jk_o(\hat{k}^i \cdot \vec{r})}$$

$$\vec{H}^i = Y_o\left[\hat{\rho}\left(\sin\gamma\cos\theta_i\cos\bar{\phi}_i - \cos\gamma\sin\bar{\phi}_i\right)\right.$$

$$- \hat{\phi}\left(\sin\gamma\cos\theta_i\sin\bar{\phi}_i + \cos\gamma\cos\bar{\phi}_i\right)$$

$$\left. - \hat{z}\sin\gamma\sin\theta_i\right]e^{jk_o[a\sin\theta_i\cos\bar{\phi}_i+z\cos\theta_i]} \tag{14}$$

is assumed to be incident on the cylinder from the direction $(\theta_i,\phi_i)$, where $\gamma$ is the polarization angle and $\hat{e}^i = \hat{\theta}^i\cos\gamma + \hat{\phi}^i\sin\gamma$ is the electric field polarization. In these, the difference between the observation and incidence angles is denoted by $\bar{\phi}_i = \phi - \phi_i$. The total surface field is given by the sum of the incident and corresponding scattered field from the infinite metallic cylinder [14]. Specifically,

$$\vec{H}^{cyl}(a,\phi,z) = \vec{H}^i(a,\phi,z) + \vec{H}^s_{cyl}(a,\phi,z)$$

$$= \hat{\phi}H^{cyl}_\phi + \hat{z}H^{cyl}_z \tag{15}$$

where

$$H^{cyl}_\phi(a,\phi,z) = -2Y_o\frac{e^{jk_o\cos\theta_i z}}{\pi k_o a \sin\theta_i}\sum_{n=-\infty}^{\infty}\left[\frac{\cos\gamma}{H_n^{(2)}(k_o a\sin\theta_i)}\right.$$

$$\left. + j\frac{n}{k_o a\sin\theta_i}\frac{\sin\gamma\cos\theta_i}{H_n^{(2)}(k_o a\sin\theta_i)}\right]jn e^{-jn\bar{\phi}_i}$$

$$H^{cyl}_z(a,\phi,z) = j2Y_o\frac{\sin\gamma}{\pi k_o a}e^{jk_o\cos\theta_i z}\sum_{n=-\infty}^{\infty}$$

$$\cdot\left[\frac{e^{jn(\frac{\pi}{2}-\bar{\phi}_i)}}{H_n^{(2)}(k_o a\sin\theta_i)}\right] \tag{16}$$

is obtained from traditional modal analysis. These expressions may be approximated by retaining only a few terms of the series if $k_o a \sin\theta_i$ is small. However, as this parameter becomes large (e.g., for large $a$ and $\theta_i \to 90°$), (16) may be replaced with equivalent asymptotic representations similar to those considered earlier. Utilizing Watson's transformation and Fock theory [14] in connection with (16), we find that

$$H^{cyl}_z \sim -Y_o\sin\gamma\sin\theta_i e^{jk_o\cos\theta_i z}$$

$$\cdot\sum_{p=1}^{2}e^{-jk_o a\sin\theta_i\Phi_p}\left[g^{(0)}(m\Phi_p)\right]^*$$

$$H^{cyl}_\phi \sim j2Y_o\cos\gamma\frac{m^2}{k_o a\sin\theta_i}e^{jk_o\cos\theta_i z}$$

$$\cdot\sum_{p=1}^{2}e^{-jk_o a\sin\theta_i\Phi_p}\left[f^{(0)}(m\Phi_p)\right]^*$$

$$- Y_o\sin\gamma\cos\theta_i e^{jk_o\cos\theta_i z}$$

$$\cdot\sum_{p=1}^{2}(-1)^p e^{-jk_o a\sin\theta_i\Phi_p}\left[g^{(0)}(m\Phi_p)\right.$$

$$\left. - j\frac{m}{k_o a\sin\theta_i}g^{(1)}(m\Phi_p)\right]^* \tag{17}$$

in which $\Phi_1 = \frac{3\pi}{2} - (\phi - \phi_i)$, $\Phi_2 = (\phi - \phi_i) - \frac{\pi}{2}$, $m = \left[\frac{k_o a\sin\theta_i}{2}\right]^{\frac{1}{3}}$, and complex conjugation is denoted by an asterisk. The appropriate far-zone Fock functions $(g^{(0)}, g^{(1)},$ and $f^{(0)})$ are given by Logan [13] and are also presented in the appendix of this paper.

The asymptotic formulas (17) are quite accurate except in the geometrical optics region $(\phi \approx \phi_i)$. In this case, Goriainov's [15] expressions

$$H^{cyl}_z \sim$$

$$- Y_o\sin\alpha\sin\theta_i e^{jk_o\cos\theta_i z}\left\{e^{-jk_o a\sin\theta_i\Phi_1}\left[g^{(0)}(m\Phi_1)\right]^*\right.$$

$$\left. + e^{jk_o a\sin\theta_i\cos(\phi-\phi_i)}[G(-m\cos(\phi-\phi_i))]^*\right\}$$

$$H^{cyl}_\phi \sim j2Y_o\cos\alpha\frac{m^2}{k_o a\sin\theta_i}$$

$$\cdot e^{jk_o\cos\theta_i z}\left\{e^{-jk_o a\sin\theta_i\Phi_1}\left[f^{(0)}(m\Phi_1)\right]^*\right.$$

$$\left. + e^{jk_o a\sin\theta_i\cos(\phi-\phi_i)}[F(-m\cos(\phi-\phi_i))]^*\right\}$$

$$+ Y_o\sin\alpha\cos\theta_i e^{jk_o\cos\theta_i z}\left\{e^{-jk_o a\sin\theta_i\Phi_1}\left[g^{(0)}(m\Phi_1)\right.\right.$$

$$\left.\left. - j\frac{m}{k_o a\sin\theta_i}g^{(1)}(m\Phi_1)\right]^*\right.$$

$$- e^{jk_o a\sin\theta_i\cos(\phi-\phi_i)}\left[G(-m\cos(\phi-\phi_i))\right.$$

$$\left.\left. - j\frac{m}{k_o a\sin\theta_i}G^{(1)}(-m\cos(\phi-\phi_i))\right]^*\right\} \tag{18}$$

34

have been found to be more accurate and can be used instead of (17). The Fock functions $(G, G^{(1)}$ and $F)$ are again defined in Logan [13] and given in the appendix. These surface field expressions may be used to calculate the entries of the column vector $\{f_i^{ext}\}$ efficiently via a numerical evaluation of (13). In particular, the modal series (16) is used when $k_o a \sin\theta_i \le 10$ and either (17) or (18) for $k_o a \sin\theta_i > 10$, as appropriate. With the excitation function and the FE-BI matrix now specified, the BiCG-FFT method [16]–[17] may be used to determine the unknown electric fields within the cavity.

## IV. SCATTERING

Once the cavity aperture and volume electric fields have been determined by solving (2) for an external excitation, the radar cross section (RCS) may be calculated. The far-zone fields may be computed by integrating the aperture fields with a suitable Green's function. In this section we present the relevant formula for calculating the far-zone fields and hence the RCS due to excitation by a plane wave (14).

To determine the far-zone fields, we begin with the integral representation for the scattered magnetic field in terms of the aperture fields. We have

$$\vec{H}^s(r,\theta,\phi) = jY_o k_o a \int_S \overline{\overline{G}}_2(r,\theta,\phi;a,\phi',z') \cdot$$
$$\left[\hat{\rho}(a,\phi',z') \times \vec{E}(a,\phi',z')\right] d\phi' dz' \quad (19)$$

with $(r, \theta, \phi)$ indicating the observation point in spherical coordinates. When the observation point is very far from the cylinder, the dyadic Green's function in (19) can be replaced by its far-zone representation

$$\overline{\overline{G}}_2(r,\theta,\phi;a,\phi',z')$$
$$\sim \frac{e^{-jk_o r}}{k_o r}\left[G^{\theta\phi}\hat{\theta}\hat{\phi}' + G^{\theta z}\hat{\theta}\hat{z} + G^{\phi\phi}\hat{\phi}\hat{\phi}'\right] \quad (20)$$

where the unprimed unit vectors are functions of the observation position and the primed ones are functions of the integration point in (19). The components of this far-zone Green's function

$$G^{\theta\phi} \sim \frac{j}{(2\pi)^2}\frac{2k_o\cos\theta}{(k_o a\sin\theta)^2}e^{jk_o\cos\theta z'}$$
$$\cdot \sum_{n=-\infty}^{\infty}\frac{n}{H_n^{'(2)}(k_o a\sin\theta)}e^{jn(\frac{\pi}{2}+(\phi-\phi'))}$$

$$G^{\theta z} \sim \frac{j}{(2\pi)^2}\frac{2}{a}e^{jk_o\cos\theta z'}$$
$$\cdot \sum_{n=-\infty}^{\infty}\frac{1}{H_n^{'(2)}(k_o a\sin\theta)}e^{jn(\frac{\pi}{2}+(\phi-\phi'))}$$

$$G^{\phi\phi} \sim \frac{j}{(2\pi)^2}\frac{2}{a\sin\theta}e^{jk_o\cos\theta z'}$$
$$\cdot \sum_{n=-\infty}^{\infty}\frac{1}{H_n^{(2)}(k_o a\sin\theta)}e^{jn(\frac{\pi}{2}+(\phi-\phi'))} \quad (21)$$

are determined by a mode matching procedure. As one might expect, these series converge rather slowly for large $k_o a \sin\theta$.

They must therefore be recast in another form by employing Watson's transformation and Fock theory, as was done previously (17). In doing so, we obtain

$$G^{\theta\phi} \sim \frac{k_o\cos\theta}{4\pi}e^{jk_o\cos\theta z'}\sum_{p=1}^{2}(-1)^p e^{-jk_o a\sin\theta\Phi_p}$$
$$\cdot \left[g^{(0)}(m\Phi_p) - j\frac{m}{k_o a\sin\theta}g^{(1)}(m\Phi_p)\right]^*$$

$$G^{\theta z} \sim -\frac{k_o\sin\theta}{4\pi}e^{jk_o\cos\theta z'}\sum_{p=1}^{2}e^{-jk_o a\sin\theta\Phi_p}\left[g^{(0)}(m\Phi_p)\right]^*$$

$$G^{\phi\phi} \sim \frac{m^2}{2a\pi\sin\theta}e^{jk_o\cos\theta z'}\sum_{p=1}^{2}e^{-jk_o a\sin\theta\Phi_p}\left[f^{(0)}(m\Phi_p)\right]^*$$
$$(22)$$

where the Fock functions are the same as those used with (17) due to reciprocity. As was the case for the plane wave source, Goriainov's [15] approximations are more accurate in the geometrical optics region $(\phi' \approx \phi)$ and similar expressions may be obtained for (22), as was found for (17). The far-zone scattered field can be computed numerically by using (19) and either the series or asymptotic formula as appropriate. Having done so, the RCS is calculated from

$$\sigma(\theta,\phi) = \lim_{r\to\infty}4\pi r^2\frac{|\vec{E}^s(r,\theta,\phi)|}{|\vec{E}^i(r,\theta,\phi)|}. \quad (23)$$

Above we presented a FE-BI formulation suitable for modeling cavity-backed structures embedded in a circular cylinder. Next, we consider a few numerical calculations aimed at validating this formulation and giving us an appreciation on how the cylinder's curvature influences the scattering parameters.

## V. RESULTS

Having solved for the electric fields induced by an incident plane wave, the resulting RCS data must be validated with known results. As previously mentioned, available measured or computed data is rather scarce, and as a consequence we are forced to rely on limiting cases in order to validate this work. As the radius of curvature decreases, a cylindrical-rectangular cavity will approximate a planar-rectangular cavity. Another limiting case involves comparison of an elongated 3-D cavity with a corresponding 2-D cavity for normal incidence $(\theta_i = 90°)$. Finally, we may compare our infinite cylinder results with a finite body of revolution (BOR) model for certain polarizations and angles of incidence. We begin with the quasiplanar case.

The first validation effort for scattering by cavity-backed patch antennas relies on the fact that a small patch on a very large radius cylinder is quasiplanar and approximates rather well an equal sized planar patch. For our test we chose as a reference a planar 3.678 cm × 2.75 cm patch residing on a 7.34 cm × 5.334 cm × 0.1448 cm cavity filled with a dielectric having $\epsilon_r = 4$. The equivalent patch on a 32.6 cm cylinder is 6.46° × 2.75 cm residing on a 12.90° × 5.334 cm × 0.1448
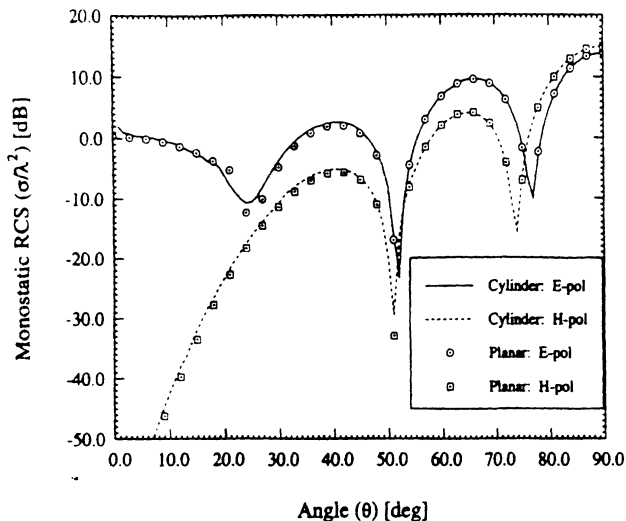
Fig. 4. Comparison of RCS for a planar patch (3.678 cm × 2.75 cm) residing on a 7.34 cm × 5.334 cm × 0.1448 cm cavity filled with $\epsilon_r = 4$ dielectric and a corresponding quasi-planar patch on a large radius (32.6 cm) cylinder. The operating frequency is 9.2 GHz.



Fig. 5. Comparison of 2-D MoM results and FE-BI RCS results for a 45° × 5λ₀ × 0.1λ₀ air-filled cavity that is recessed in a cylinder with a radius of 1λ₀.

cm cavity. At the operating frequency of 9.2 GHz, the cylinder has an electrical radius of $10\lambda_o$.

Fig. 4 shows the results for the patch on a large radius cylinder with corresponding data for the planar cavity-backed patch. Clearly, the two RCS patterns are in excellent agreement, and although Fig. 4 illustrates only monostatic scattering in the $\phi = 0°$ plane, additional runs for normally incident monostatic scattering and various bistatic situations yield similar agreement.

Comparisons may also be made for elongated cavities and 2-D MoM results. Long narrow cavities have very little axial interaction for principal plane ($\theta = 90°$) excitation and therefore results based on this formulation should compare well with corresponding 2-D data. It is well known that the RCS of a 3-D scattering body of length $L \gg \lambda_0$ is related to the corresponding 2-D scattering of the same cross section via the relation

$$\sigma_{3D} = 2\left(\frac{L}{\lambda_0}\right)^2 \sigma_{2D}. \tag{24}$$

Such a comparison is shown in Fig. 5 for monostatic scattering by a 45° × 5λ × 0.1λ cavity recessed in a cylinder with a radius of 1λ₀ for both principal polarizations. Once again the agreement between the two results is excellent, thus providing a partial validation of the formulation for highly curved geometries. We remark that similar agreement has been observed for bistatic scattering in the $\theta = 90°$ plane.

The planar approximation eliminates the effects of curvature, which is a primary interest in this work, and the 2-D comparisons done above are only valid for normal incidence and observation. To consider oblique angles and a highly curved structure, we resort to comparisons with a body of revolution (BOR) code for wraparound cavities. Since the BOR code can only model finite structures, we simulate an infinite cylinder by coherently subtracting the far-zone fields
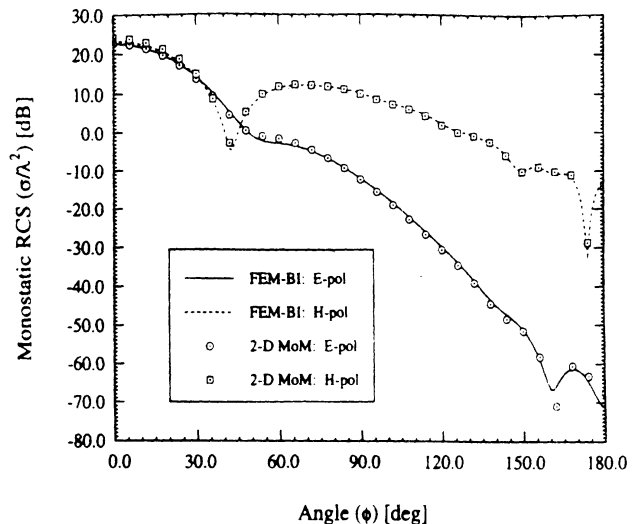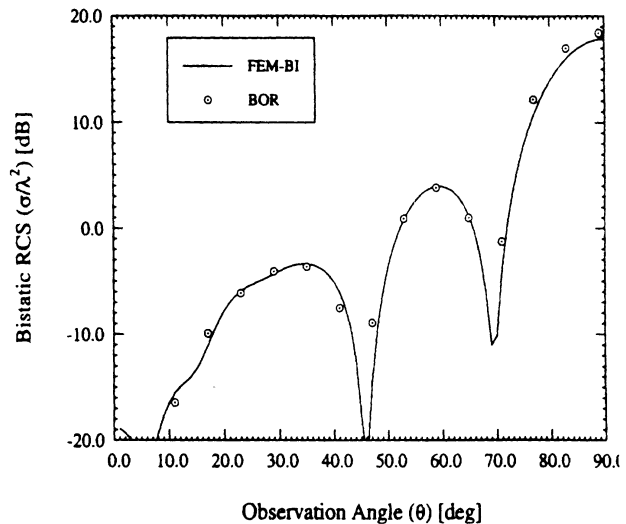


Fig. 6. Comparison of the RCS computed via the FE-BI method and a BOR code for a 3λ₀ × 0.1λ₀ air-filled wraparound cavity recessed in a cylinder with a radius of 1λ₀ that is excited by a normally incident H-polarized (α = 90°) plane wave.

of the finite structure without a cavity from similar data which includes the cavity. Such an procedure mimics common measurement practices and was found suitable for near normal incidence and quite acceptable near grazing incidence in the case of H-polarization ($\alpha = 90°$). An example calculation for the former case is given in Fig. 6. where a bistatic scattering pattern is presented in the $\phi = 0°$ plane due to a plane wave incident at ($\theta_i = 90°, \phi_i = 0°$). Clearly, there is good agreement between the FE-BI results and data based on the BOR formulation.

The previous comparisons serve to validate the formulation. Having done so, it is instructive to examine the effect that curvature has on the scattering properties of cavity-backed patch antennas. Consider a 2 cm × 3 cm patch residing on a 5 cm × 6 cm × 0.07874 cm cavity that is filled with a dielectric having $\epsilon_r = 2.17$. The cylinder has a radius of 15.28 cm. Figs.

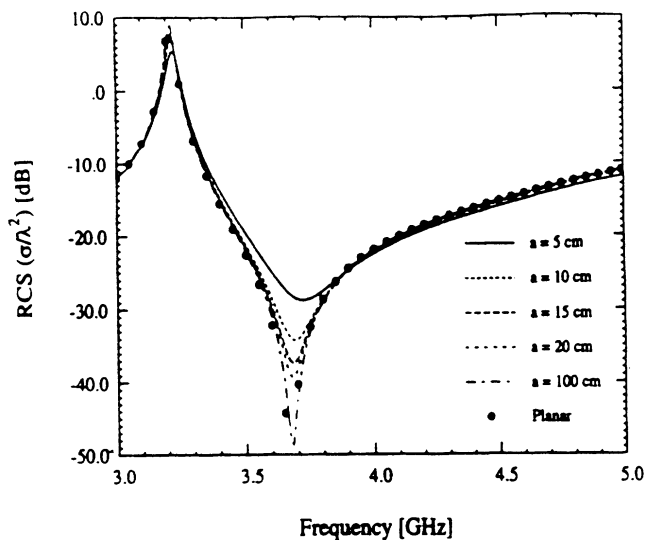Fig. 7. RCS frequency response for a 2 cm × 3 cm patch residing in a 5 cm × 6 cm × 0.07874 cm cavity with $\epsilon_r$ = 2.17 as a function of curvature for E-polarization ($\alpha$ = 0°).
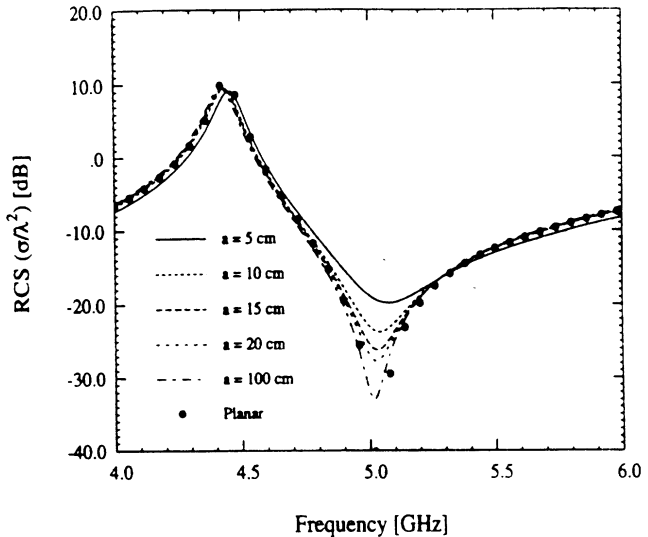
Fig. 8. RCS frequency response for a 2 cm × 3 cm patch residing in a 5 cm × 6 cm × 0.07874 cm cavity with $\epsilon_r$ = 2.17 as a function of curvature for H-polarization ($\alpha$ = 90°).

7 and 8 illustrate the behavior of this geometry as a function of frequency and curvature.

Evidently, the resonance behavior of this patch is sensitive to curvature for both principal polarizations. The frequency response for E-polarization is more sensitive to curvature since the radiating surface field component is parallel to the long side of the patch and cavity. If the patch and cavity were oriented so that the long side is in the $\phi$ direction, the response to H-polarization would exhibit greater sensitivity. Such an effect is important to low observable antenna designers since they want to operate the antenna in the region of lowest RCS. This low return region is a consequence of delicate cancellations due to the physical layout of the aperture. Such cancellations are not as complete for highly curved structures as they are for planar cavities.

Conformal antenna designers often use wraparound antennas to achieve omnidirectional coverage. Two different configurations are typically used: a continuous cavity where the cavity is filled with a single continuous collar of dielectric, and discrete cavities symmetrically placed around the circumference of the cylinder. These two configurations are shown in Fig. 9.

Since near resonance the radiation properties of these two types of antennas are similar, any RCS advantage one might possess could govern the appropriate choice of arrays. Fig. 10 compares the E-polarized monostatic scattering at 3 GHz in the $\theta$ = 90° plane for a wraparound cavity and four discrete cavities, where the patches and cavities are identical to those used in the previous example. The radius of the cylinder is 15.28 cm. and the four patches are centered at 0°, 90°, 180°, and 270°. Not surprisingly, the wraparound structure has a higher return due to coupling within the substrate. However, since in this case the scattered field is due to the $z$ component of the surface field ($\phi$-directed magnetic currents), both cavities yield large scattered fields in the four directional lobes. Fig. 11 is the corresponding comparison for H-polarization.

In this case, the scattered field is attributed to the $\phi$ component of the surface fields ($z$-directed magnetic currents). Therefore, substrate modes diffract near the patch, resulting in discrete lobes for the discrete array while creeping waves shed isotropically for the continuous wraparound cavity. Low observable designs will favor discrete cavity arrays over continuous cavities since the scattering may be channeled in preferred directions and the overall scattering level is consistently lower. A final example is shown in Fig. 12, where we observe that other than the expected higher scattering from the wraparound cavity, the scattering behavior of the two arrays is very similar.

## VI. CONCLUSIONS

In this paper, we have presented a finite element–boundary (FE-BI) integral technique suitable for electromagnetic scattering calculations involving cavities embedded within a circular, metallic cylinder. This formulation is analogous to the FE-BI approach used by Jin and Volakis [1], [5], [6] and may accordingly be used for the analysis of scattering by a large array of cavity-backed patch antennas. These cavities need not be identical, periodically spaced, or homogeneously filled and may in fact may possess lumped impedance loads or surface metallization layers. The FE approach employs vector finite elements that properly represent the electromagnetic fields and possess high geometrical fidelity for cylindrical-rectangular cavities. Such elements were presented and are analogous to the bricks used for modeling rectangular cavities. In addition, we presented an efficient method for evaluating the on-surface and far-zone dyadic Green's functions. The presented formulation is amenable to solution using the BiCG-FFT method provided uniform zoning is used across the aperture, and as a consequence this implementation has low computational and memory demand. We have presented some validation of this work with appropriate limiting cases that provides further archival reference data. In addition, we showed how this formulation may be used to influence conformal antenna designs.
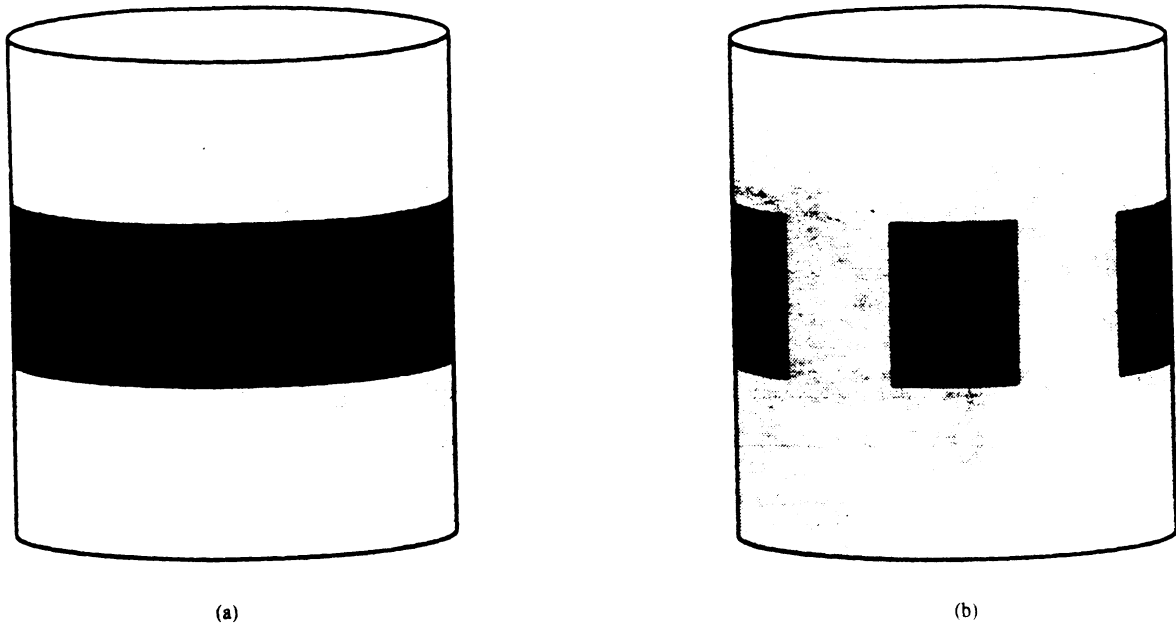
(a)                                          (b)

Fig. 9.   Illustration of two types of arrays: (a) continuous wraparound array; (b) discrete wraparound cavity array.



Angle (φ) [deg]

Fig. 10.   Comparison of E-polarized monostatic RCS at 3 GHz for a four-patch array placed on a wraparound collar or in four discrete cavities. The cylinder radius is 15.28 cm. The patches and cavities are identical to the one used in Fig. 7. The observation plane is $\theta = 90°$.
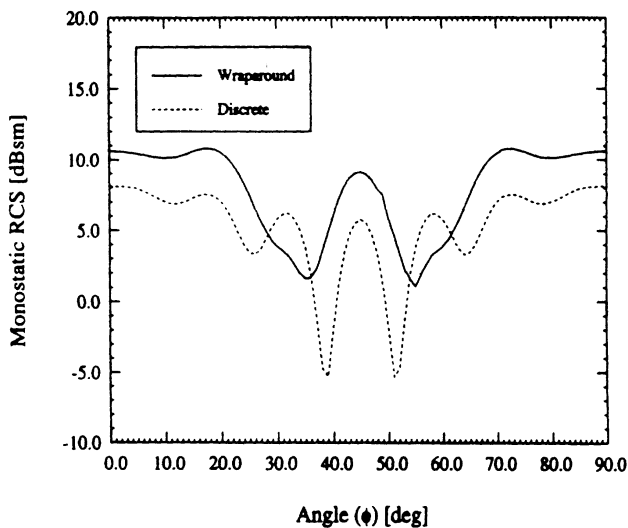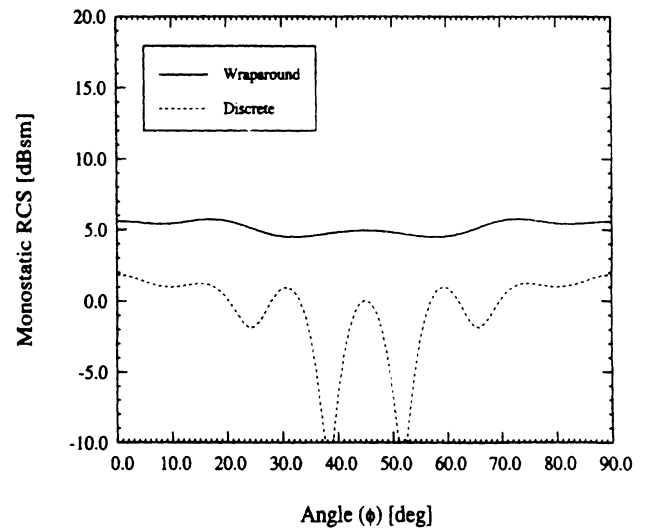
Fig. 11.   Comparison of H-polarized monostatic RCS at 3 GHz for a four patch array placed on a wraparound collar or in four discrete cavities. The cylinder radius is 15.28 cm. The patches and cavities are identical to the one used in Fig. 8. The observation plane is $\theta = 90°$.

## APPENDIX:
## FOCK FUNCTIONS

The asymptotic form of the dyadic Green's function with observation both on the surface of the cylinder and in the far field involves Fock functions. These have been extensively studied and tabulated by Logan [13]. The numerical evaluation of these functions is performed for either small arguments or large arguments.

The on-surface Fock functions used in this paper are

$$v(\xi) = \frac{1}{2}e^{j\pi/4}\sqrt{\frac{\xi}{\pi}} \int_{\infty e^{-j2\pi/3}}^{\infty} \frac{w_2(\tau)}{w_2'(\tau)} e^{-j\xi\tau} d\tau$$

$$u(\xi) = e^{j3\pi/4}\frac{\xi^{\frac{3}{2}}}{\sqrt{\pi}} \int_{\infty e^{-j2\pi/3}}^{\infty} \frac{w_2(\tau)}{w_2'(\tau)} e^{-j\xi\tau} d\tau \qquad \text{(A-1)}$$

where $w_2(\tau)$ and its derivative $w_2'(\tau)$ denote Airy functions of the Second Kind. For small arguments ($\xi < 0.6$), the asymptotic expansion of (A-1) is given by

$$v(\xi) \sim 1.0 - \frac{\sqrt{\pi}}{4}\xi^{\frac{3}{2}} + j\frac{7}{60}\xi^3 + \frac{7}{512}\sqrt{\pi}e^{-j\frac{\pi}{4}}\xi^{\frac{9}{2}} + \cdots$$

$$u(\xi) \sim 1.0 - \frac{\sqrt{\pi}}{2}\xi^{-j\frac{\pi}{4}}\xi^{\frac{3}{2}} + j\frac{5}{12}\xi^3 + \frac{5}{64}\sqrt{\pi}e^{-j\frac{\pi}{4}}\xi^{\frac{9}{2}} + \cdots$$

(A-2)

while a rapidly converging residue series is used for $\xi > 0.6$:

$$v(\xi) \sim = e^{-j\frac{\pi}{4}}\sqrt{\pi\xi}\sum_{n=1}^{10}\left(\tau_n'\right)^{-1}e^{-j\xi\tau_n'}$$
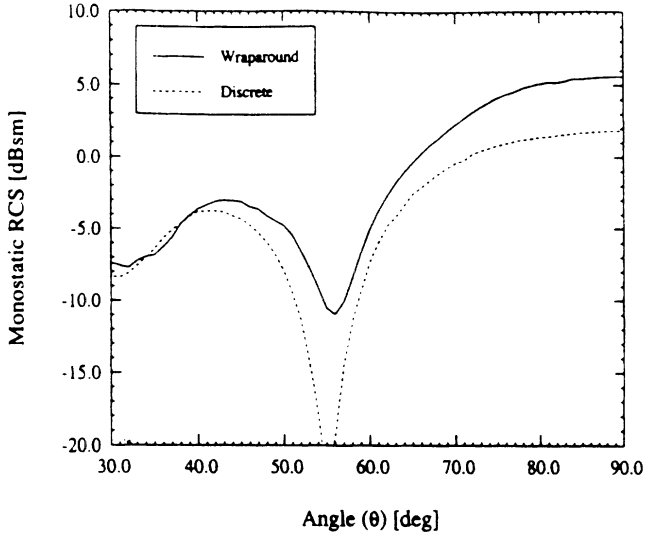
Fig. 12. Comparison of H-polarized monostatic scattering at 3 GHz by a four-patch array placed on a wraparound collar or in four discrete cavities. The cylinder radius is 15.28 cm. The patches and cavities are identical to the one used in Fig. 8. The observation plane is $o = 0°$.

TABLE I

| Table B-1 | |
|---|---|
| Zeros of the $w_2(\tau)$ and $w_2'(\tau)$ | |
| $\tau_n = |\tau_n|e^{-j\frac{\pi}{3}}$ and $\tau_n' = |\tau_n'|e^{-j\frac{\pi}{3}}$ | |
| n | $|\tau_n|$ | $|\tau_n'|$ |
|---|---|---|
| 1 | 2.33811 | 1.011879 |
| 2 | 4.08795 | 3.24819 |
| 3 | 5.52056 | 4.82010 |
| 4 | 6.78661 | 6.16331 |
| 5 | 7.94413 | 7.37218 |
| 6 | 9.02265 | 8.48849 |
| 7 | 10.0402 | 9.53545 |
| 8 | 11.0085 | 10.5277 |
| 9 | 11.9300 | 11.4751 |
| 10 | 12.8288 | 12.3848 |

$$u(\xi) \sim= 2e^{j\frac{\pi}{4}}\sqrt{\pi}\xi^{\frac{3}{2}}\sum_{n=1}^{10}(\tau_n)^{-1}e^{-j\xi\tau_n} \qquad (A-3)$$

where $\tau_n$ and $\tau_n'$ are zeros of $w_2(\tau)$ and $w_2'(\tau)$, respectively. Those zeros are given in Table I.

The far-zone Fock functions are given by

$$g^{(l)}(\xi) = \frac{j^l}{\sqrt{\pi}}\int_\Gamma \frac{e^{j\xi\tau}}{w_1'(\tau)}d\tau$$

$$f^{(l)}(\xi) = \frac{j^l}{\sqrt{\pi}}\int_\Gamma \frac{e^{j\xi\tau}}{w_1(\tau)}d\tau$$

$$G^{(l)}(\xi) = g^{(l)}(\xi)e^{j\frac{\xi^3}{3}}$$

$$F^{(l)}(\xi) = f^{(l)}(\xi)e^{j\frac{\xi^3}{3}} \qquad (A-4)$$

where $w_1(\tau)$ and its derivative $w_1'(\tau)$ denote Airy functions of the First Kind and the integration contour is given by Logan [13]. These functions, $g^{(0)}(\xi)$, $g^{(1)}(\xi)$, and $f^{(0)}(\xi)$, may be

TABLE II

| Table B-2 | | | |
|---|---|---|---|
| Constants for (A-5) and (A-6) | | | |
| m | c(m) | $\alpha'(m)$ | Ai(m) |
|---|---|---|---|
| 1 | 0.7473831 | 1.01879297 | 0.5356566 |
| 2 | -0.6862081 | 3.2481975 | -0.41901548 |
| 3 | -2.9495325 | 4.82009921 | 0.38040647 |
| 4 | -3.4827075 | 6.16330736 | -0.35790794 |
| 5 | 8.9378967 | 7.37217726 | 0.34230124 |
| 6 | 56.1946214 | 8.48848673 | -0.33047623 |
| 7 | | 9.53544905 | 0.32102229 |
| 8 | | 10.52766040 | -0.31318539 |
| 9 | | 11.47505663 | 0.30651729 |
| 10 | | 12.38478837 | -0.30073083 |

calculated using

$$g^{(0)}(\xi) = 2.0e^{-j\frac{\xi^3}{3}} \qquad \xi < -1.3$$

$$= 1.39937 + \sum_{m=1}^{6}\frac{c(m)}{m!}(\kappa\xi)^m \qquad -1.3 \le \xi \le 0.5$$

$$= \sum_{m=1}^{10}\frac{e^{[\kappa\alpha'(m)\xi]}}{\alpha'(m)Ai(m)} \qquad 0.5 < \xi \le 4.0$$

$$= 1.8325e^{\left[-(0.8823-j0.5094)\xi-j\frac{\xi^3}{3}\right]} \qquad \xi > 4.0 \quad (A-5)$$

$$g^{(1)}(\xi) = -j2.0\left(\xi^2 + j\frac{0.25}{\xi} - \frac{0.25}{\xi^4}\right)e^{-j\frac{\xi^3}{3}} \qquad \xi < -2.8$$

$$= \sum_{m=1}^{6}\frac{c(m)\kappa^m}{m!}(\xi)^{m-1} \qquad -2.8 \le \xi \le 0.5$$

$$= \kappa\sum_{m=1}^{10}\frac{e^{[\kappa\alpha(m)\xi]}}{Ai(m)} \qquad 0.5 < \xi \le 4.0$$

$$= -1.8325(0.8823 - j0.5094 + j\xi^2)$$
$$\cdot e^{\left[-(0.8823-j0.5094)\xi-j\frac{\xi^3}{3}\right]} \qquad \xi > 4.0 \qquad (A-6)$$

$$f^{(0)}(\xi) = j2\xi\left(1 - \frac{0.25}{\xi^3} + \frac{0.5}{\xi^6}\right)e^{-j\frac{\xi^3}{3}} \qquad \xi < -1.1$$

$$= 0.77582 + e^{-j\pi/3}\sum_{m=1}^{6}\frac{c(m)}{m!}(\kappa\xi)^m \qquad -1.1 \le \xi \le 0.5$$

$$= e^{-j\pi/3}\sum_{m=1}^{10}\frac{e^{[\kappa\alpha(m)\xi]}}{Ai(m)} \qquad 0.5 < \xi \le 4.0$$

$$= 0.0 \qquad \xi > 4.0 \qquad (A-7)$$

with constant $\kappa = e^{-j5\pi/6}$ and the coefficients for (A-5) and (A-6) given in Table II.

The corresponding constants for (A-7) are given as shown in Table III.

TABLE III

| Table B-3 Constants for (A-7) | | | |
|---|---|---|---|
| m | c(m) | $\alpha$(m) | $Ai'$(m) |
| 1 | 1.146730417 | 2.33810741 | 0.70121082 |
| 2 | 0.86284558 | 4.08794944 | -0.80311137 |
| 3 | -2.0192636 | 5.52055983 | 0.86520403 |
| 4 | -9.977776 | 6.78670809 | -0.91085074 |
| 5 | -14.59904 | 7.94413359 | 0.94733571 |
| 6 | 49.0751 | 9.02265085 | -0.97792281 |
| 7 | | 10.04017434 | 1.00437012 |
| 8 | | 11.00852430 | -1.02773869 |
| 9 | | 11.93601556 | 1.04872065 |
| 10 | | 12.82877675 | -1.06779386 |

## FE Matrix Entries

The matrix entries for the FE portion of the system (5) are given in this appendix assuming that the cylindrical shell elements (4) are used in (6). These integrals are given by

$$I_{\rho\rho}^{(1)} = \frac{\bar{s}_s \bar{s}_t}{(\alpha h)^2} \left[ \rho_b^2 h \ln\left(\frac{\rho_b}{\rho_a}\right) \int_{\phi_l}^{\phi_r} (\phi - \bar{\phi}_s)(\phi - \bar{\phi}_t) d\phi \right.$$
$$\left. + \frac{\alpha}{2}\left(\frac{\rho_b^2}{\rho_a^2} - 1\right) \int_{z_b}^{z_t} (z - \bar{z}_s)(z - \bar{z}_t) dz \right]$$

$$I_{\rho\phi}^{(1)} = -\frac{\bar{s}_s \bar{s}_t}{th^2} \left[ 2\rho_b \ln\left(\frac{\rho_b}{\rho_a}\right) + \bar{\rho}_t\left(1 - \frac{\rho_b}{\rho_a}\right) \right]$$
$$\cdot \int_{z_b}^{z_t} (z - \bar{z}_s)(z - \bar{z}_t) dz$$

$$I_{\rho z}^{(1)} = -\frac{\bar{s}_s \bar{s}_t \rho_b}{\alpha^2} \int_{\phi_l}^{\phi_r} (\phi - \bar{\phi}_s)(\phi - \bar{\phi}_t) d\phi$$

$$I_{\phi\phi}^{(1)} = \frac{\bar{s}_s \bar{s}_t \alpha}{(th)^2} \left[ h\left(\frac{1}{4}\left(\rho_b^4 - \rho_a^4\right)\right.\right.$$
$$\left.+ \frac{1}{3}(\bar{\rho}_s + \bar{\rho}_t)\left(\rho_a^3 - \rho_b^3\right) + \frac{1}{2}\bar{\rho}_s\bar{\rho}_t\left(\rho_b^2 - \rho_a^2\right)\right)$$
$$+ \left(2\left(\rho_b^2 - \rho_a^2\right) - 2t(\bar{\rho}_s + \bar{\rho}_t) + \bar{\rho}_s\bar{\rho}_t \ln\left(\frac{\rho_b}{\rho_a}\right)\right)$$
$$\left.\cdot \int_{z_b}^{z_t} (z - \bar{z}_s)(z - \bar{z}_t) dz \right]$$

$$I_{\phi z}^{(1)} = -\frac{\bar{s}_s \bar{s}_t}{t^2} \int_{\rho_a}^{\rho_b} (\rho - \bar{\rho}_s)(\rho - \bar{\rho}_t) d\rho$$

$$I_{zz}^{(1)} = \frac{\bar{s}_s \bar{s}_t h}{(t\alpha)^2} \left[ \alpha\left(\frac{1}{2}\left(\rho_b^2 - \rho_a^2\right) - t(\bar{\rho}_s + \bar{\rho}_t) + \bar{\rho}_s\bar{\rho}_t \ln\left(\frac{\rho_b}{\rho_a}\right)\right) \right.$$
$$\left. + \frac{1}{2}\left(\rho_b^2 - \rho_a^2\right) \int_{\phi_l}^{\phi_r} (\phi - \bar{\phi}_s)(\phi - \bar{\phi}_t) d\phi \right]$$

$$I_{\rho\rho}^{(2)} = \frac{\bar{s}_s \bar{s}_t \rho_b^2}{(\alpha h)^2} \ln\left(\frac{\rho_b}{\rho_a}\right) \int_{\phi_l}^{\phi_r} (\phi - \bar{\phi}_s)(\phi - \bar{\phi}_t) d\phi$$
$$\cdot \int_{z_b}^{z_t} (z - \bar{z}_s)(z - \bar{z}_t) dz$$

$$I_{\phi\phi}^{(2)} = \frac{\bar{s}_s \bar{s}_t \alpha}{(th)^2} \left[ \frac{1}{4}\left(\rho_b^4 - \rho_a^4\right) + \frac{1}{3}(\bar{\rho}_s + \bar{\rho}_t)\left(\rho_a^3 - \rho_b^3\right) \right.$$
$$\left. + \frac{1}{2}\bar{\rho}_s\bar{\rho}_t\left(\rho_b^2 - \rho_a^2\right) \right] \times \int_{z_b}^{z_t} (z - \bar{z}_s)(z - \bar{z}_t) dz$$

$$I_{zz}^{(2)} = \frac{\bar{s}_s \bar{s}_t h}{(t\alpha)^2} \left[ \frac{1}{4}\left(\rho_b^4 - \rho_a^4\right) + \frac{1}{3}(\bar{\rho}_s + \bar{\rho}_t)\left(\rho_a^3 - \rho_b^3\right) \right.$$
$$\left. + \frac{1}{2}\bar{\rho}_s\bar{\rho}_t\left(\rho_b^2 - \rho_a^2\right) \right] \times \int_{\phi_l}^{\phi_r} (\phi - \bar{\phi}_s)(\phi - \bar{\phi}_t) d\phi.$$

(B-1)

Each of the above unevaluated integrals is of the form

$$\int_L^U \left(\xi - \bar{\xi}_s\right)\left(\xi - \bar{\xi}_t\right) d\xi = \frac{1}{2}\left(L^2 - U^2\right)\left(\bar{\xi}_s + \bar{\xi}_t\right)$$
$$+ \frac{1}{3}\left(U^3 - L^3\right) + \bar{\xi}_s\bar{\xi}_t(U - L).$$

(B-2)

The integrals $I_{st}^{(1),(2)}$ are used in the assembly of the FE portion ([A]) of the system.

## References

[1] J.-M. Jin and J. L. Volakis, "A hybrid finite element method for scattering and radiation by microstrip patch antennas and arrays residing in a cavity," IEEE Trans. Antennas Propagat., vol. 39, no. 11, pp. 1598–1604, Nov. 1991.

[2] J. L. Volakis, A. Chatterjee, and J. Gong, "A class of hybrid finite element methods for electromagnetics: A review," to appear in J. Electromagn. Waves Appl., 1994.

[3] Z. J. Cendes, "Vector finite elements for electromagnetic field computation," IEEE Trans. Magn., vol. 27, no. 5, pp. 3958–3966, Sept. 1991.

[4] A. Bossavit, "A rationale for edge-elements in 3D fields computations," IEEE Trans. Magn., vol. 24, no. 1, pp. 74–79, Jan. 1988.

[5] J.-M. Jin and J. L. Volakis, "A finite element-boundary integral formulation for scattering by three-dimensional cavity-backed apertures," IEEE Trans. Antennas Propagat., vol. 39, no. 1, pp. 97–104, Jan. 1991.

[6] ——, "Electromagnetic scattering by and transmission through a three-dimensional slot in a thick conducting plane," IEEE Trans. Antennas Propagat., vol. 39, no. 4, pp. 543–550, Apr. 1991.

[7] A. Chatterjee, J.-M. Jin, and J. L. Volakis, "Computation of cavity resonances using edge-based finite elements," IEEE Trans. Microwave Theory Tech., vol. 40, no. 11, pp. 2106–2108, Nov. 1992.

[8] C.-T. Tai, Dyadic Green's Functions in Electromagnetic Theory. Scranton, PA: International Textbook, 1971.

[9] P. H. Pathak and N. N. Wang, "An analysis of the mutual coupling between antennas on a smooth convex surface," Ohio State Univ. ElectroScience Lab., Rep. 784583-7, Oct. 1978.

[10] J. Boersma and S. W. Lee, "Surface field due to a magnetic dipole on a cylinder: Asymptotic expansions of exact solution," Univ. Illinois Electromagnetics Lab., Rep. 78-17, 1978.

[11] T. S. Bird, "Comparison of asymptotic solutions for the surface field excited by a magnetic dipole on a cylinder," IEEE Trans. Antennas Propagat., vol. 32, no. 11, pp. 1237–1244, Nov. 1984.

[12] ——, "Accurate asymptotic solution for the surface field due to apertures in a conducting cylinder," IEEE Trans. Antennas Propagat., vol. 33, no. 10, pp. 1108–1117, Oct. 1985.

[13] N. A. Logan, "General research in diffraction theory," Lockheed Aircraft Corp., Missiles and Space Div., vol. 1 and 2, Rep. LMSD-288088, Dec. 1959.

[14] O. Einarsson, R. E. Kleinman, P. Laurin, and P. L. E. Uslenghi, "Studies in radar cross sections L—Diffraction and scattering by regular bodies IV: The circular cylinder," Univ. of Michigan, Tech. Rep. 7133-3-T, 1966.

[15] A. S. Gonainov, "An asymptotic solution of the problem of diffraction of a plane electromagnetic wave by a conducting cylinder," Radio Eng. Electron. Phys., vol. 3, pp. 23–39, 1958. (English translation of Radiotekhnica i Elektronica, vol. 3)

[16] T. K. Sarkar, "On the application of the generalized biconjugate gradient method," J. Electromagn. Waves Appl., vol. 1, no. 3, pp. 223–242, 1987.

[17] C. F. Smith, A. F. Peterson, and R. Mittra, "The biconjugate gradient method for electromagnetic scattering," IEEE Trans. Antennas Propagat., vol. 38, no. 6, pp. 938–940, June 1990.

**Leo C. Kempel** (S'89) was born on October 30, 1965, in Akron, OH. He participated in the co-operative education program from January 1986 to September 1989 with General Dynamics/Fort Worth Div, and received the BSEE degree from the University of Cincinnati, Cincinnati, OH, in 1989. He received the MSEE degree and the Ph.D. degree from the University of Michigan in 1990 and 1994, respectively.

Since September 1989 he has been associated with the Radiation Laboratory at the University of Michigan as a Graduate Student Research Assistant. He is currently a Senior Electrical Engineer with Mission Research Corp. Combat Applications Group, Valparaiso, FL. His research interests include analytical and computational electromagnetics as applied to scattering and radiation problems.

Dr. Kempel is a member of Tau Beta Pia and Eta Kappa Nu.

**John L. Volakis** (S'77-M'82-SM'89), for a photograph and biography, please see p. 1242 of this issue of this TRANSACTIONS.

41

FE-ABC FORMULATION FOR PATCH ANTENNAS ON A CIRCULAR
CYLINDER

Leo C. Kempel and John L. Volakis
The University of Michigan
Radiation Laboratory
1301 Beal Ave.
Ann Arbor, MI 48109-2122

### Abstract

The finite element-boundary integral (FE-BI) method has been shown to
accurately model the scattering and radiation of cavity-backed patch anten-
nas. Unfortunately, extension of this rigorous technique to coated or doubly
curved platforms is cumbersome and inefficient. An alternative approximate
approach is to employ an absorbing boundary condition for terminating the
finite element mesh thus avoiding use of a Green's function. In this report,
a FE-ABC method is used to calculate the radar cross section (RCS) and
radiation pattern of a cavity-backed patch antenna which is recessed within
a metallic surface. It is shown that this approach is accurate for RCS and
antenna pattern calculations with an ABC surface displaced as little as $0.3\lambda$
from the cavity aperture. These patch antennas may have a dielectric overlay
which may also be modelled with this technique.

# 1  Introduction

Recently, a Finite Element-Boundary Integral (FE-BI) formulation was pro-
posed by the authors [1] for modeling the scattering and radiation of cavity-
backed patch antennas recessed in a cylindrical platform. The use of the
boundary integral for terminating the FE mesh renders the FE-BI method
numerically exact but leads to a partially full and partially sparse matrix. To
obtain a fully sparse system, we must use approximate local boundary con-
ditions for terminating the FE mesh and this is usually done by employing
absorbing boundary conditions (ABCs).

In this report, a new conformal ABC recently introduced by Chatterjee
and Volakis [2] will be used for scattering and radiation parameter calcu-
lations in connection with cavity-backed antenna elements on a cylindrical

platform. This second order conformal ABC allows the closure surface to be brought quite close to the cavity aperture. As a result, the required degrees of freedom are significantly less than the number typically used with traditional spherical surface/boundary condition such as the one proposed by Peterson [3] or the one introduced by Webb and Kanellopoulos [4]. The accuracy of this FE-ABC method will be established along with guidelines for the distance between the structure and the ABC boundary. In addition, this new FE-ABC approach will be used to compute the radiation pattern and input impedance of conformal patch antennas with a dielectric overlay.

## 2 Formulation

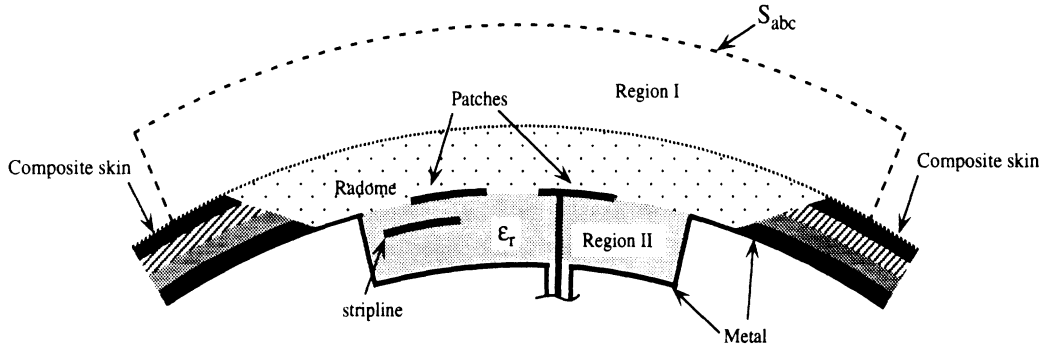Consider the computational domain shown in Figure 1. There are two volume



Figure 1: Typical coated cavity-backed patch antenna with ABC mesh termination.

regions: an exterior region, $V^I$, which includes any radome overlay and an interior region, $V^{II}$. Both regions may be inhomogeneous and are separated by the aperture surface, $S^{ap}$, and the surface metallization surface, $S^{sm}$ both of which lie on the surface of the metallic cylinder ($\rho = a$). Thus, the exterior region is defined by $\rho \geq a$ while the interior region has $\rho \leq a$. The computational domain is bounded by the union of the metallic surface, $S^{metal} = S^{sm} + S^{cm}$ where $S^{cm}$ is the metallic walls of the cavity and the ABC surface, $S^{abc}$.

43

Within the computational volume, the total electric fields may be written as

$$
\begin{aligned}
\vec{E}(\vec{r}) &= \vec{E}^I(\vec{r}) + \vec{E}^{cyl}(\vec{r}) \quad \vec{r} \in V^I \\
&= \vec{E}^{II}(\vec{r}) \qquad\qquad \vec{r} \in V^{II}
\end{aligned}
\tag{1}
$$

where $\vec{E}^{cyl}(\vec{r}) = \vec{E}^i(\vec{r}) + \vec{E}^r(\vec{r})$ as before. The total magnetic fields are likewise written

$$
\begin{aligned}
\vec{H}(\vec{r}) &= \vec{H}^I(\vec{r}) + \vec{H}^{cyl}(\vec{r}) \quad \vec{r} \in V^I \\
&= \vec{H}^{II}(\vec{r}) \qquad\qquad \vec{r} \in V^{II}
\end{aligned}
\tag{2}
$$

where $\vec{H}^{cyl}(\vec{r}) = \vec{H}^i(\vec{r}) + \vec{H}^r(\vec{r})$. The boundary conditions are readily written in terms of the electric and magnetic fields. Within the cavity, the tangential electric field vanishes on the metallic walls

$$
\hat{n} \times \vec{E}^{II}(\vec{r}) = 0 \quad \vec{r} \in S^{cm}
\tag{3}
$$

while on the aperture, the total tangential fields are continuous

$$
\begin{aligned}
\hat{n} \times \vec{E}^I(\vec{r}) &= \hat{n} \times \vec{E}^{II}(\vec{r}) && \vec{r} \in S^{ap} \\
\hat{n} \times \vec{H}^I(\vec{r}) &= \hat{n} \times \vec{H}^{II}(\vec{r}) - \hat{n} \times \vec{H}^{cyl}(\vec{r}) && \vec{r} \in S^{ap}
\end{aligned}
\tag{4}
$$

On metallic surfaces, all tangential electric fields vanish, i.e.

$$
\hat{n} \times \vec{E}^{cyl}(\vec{r}) = \hat{n} \times \vec{E}^I(\vec{r}) = \hat{n} \times \vec{E}^{II}(\vec{r}) = 0 \quad \vec{r} \in S^{sm}
\tag{5}
$$

while $\hat{n} \times \vec{E}^{cyl}(\vec{r})$ also vanishes over the aperture

$$
\hat{n} \times \vec{E}^{cyl}(\vec{r}) = 0 \quad \vec{r} \in S^{ap}
\tag{6}
$$

since it contains both the incident and reflected fields. Thus, the only non-zero electric fields on the surface of the metallic cylinder correspond to the unknown fields within each region which are continuous across the surface aperture as implied by (4).

The FE equations may be developed by considering the inhomogeneous vector wave equation. Employing the method of weighted residuals and

44

Green's first vector identity, the weak form of the vector wave equation

$$\int_{V_i} \frac{\nabla \times \vec{E}(\rho, \phi, z) \cdot \nabla \times \vec{W}_i(\rho, \phi, z)}{\mu_r(\rho, \phi, z)} \rho\, d\rho\, d\phi\, dz$$

$$-k_o^2 \int_{V_i} \epsilon_r(\rho, \phi, z) \vec{E}(\rho, \phi, z) \cdot \vec{W}_i(\rho, \phi, z) \rho\, d\rho\, d\phi\, dz$$

$$-j k_o Z_o \oint_{S_i} \hat{n}(\rho, \phi, z) \times \vec{H}(\rho, \phi, z) \cdot \vec{W}_i(\rho, \phi, z) dS = f_i^{int} \qquad (7)$$

where $\hat{n}(\rho, \phi, z)$ indicates the outward pointing normal of the element surface associated with the $i$th unknown, $S_i$ is the surface area of that element, and $\vec{H}(\rho, \phi, z)$ is the total magnetic field. It can be shown that the surface integral of (7) vanishes for all elements which do not border the cavity aperture. Furthermore, their non-zero contribution is limited to the portion of their surface which coincides with the aperture. The interior source functional, $f_i^{int}$, is once again given by

$$f_i^{int} = -\int_{V_i} \left\{ \nabla \times \left[ \frac{\vec{M}^i(\rho, \phi, z)}{\mu_r(\rho, \phi, z)} \right] + j k_o Z_o \vec{J}^i(\rho, \phi, z) \right\} \cdot \vec{W}_i(\rho, \phi, z) \rho\, d\rho\, d\phi \quad (8)$$

where $\vec{M}^i$ and $\vec{J}^i$ are impressed currents within the cavity.

A domain decomposition is accomplished by substituting the total field relationships (1) and (2) into (7) and after some manipulation we get the FE-ABC equation

$$\int_{V_i^I} \left[ \frac{\nabla \times \vec{E}^I \cdot \nabla \times \vec{W}_i}{\mu_r} - k_o^2 \epsilon_r \vec{E}^I \cdot \vec{W}_i \right] dV +$$

$$\int_{V_i^{II}} \left[ \frac{\nabla \times \vec{E}^{II} \cdot \nabla \times \vec{W}_i}{\mu_r} - k_o^2 \epsilon_r \vec{E}^{II} \cdot \vec{W}_i \right] dV +$$

$$\int_{S_i^{abc}} \left( \hat{n} \times \nabla \times \vec{E}^I \right) \cdot \vec{W}_i\, dS = f_i^{int} + j \frac{k_o Z_o}{\mu_{re}} \int_{S_i^{ap}} \left( \hat{\rho} \times \vec{H}^{cyl} \right) \cdot \vec{W}_i\, dS -$$

$$k_o^2 \int_{V_i^{Id}} \left[ \frac{1}{\mu_r} - \epsilon_r \right] \vec{E}^{cyl} \cdot \vec{W}_i\, dV - j k_o Z_o \left[ \frac{1}{\mu_{ri}} - \frac{1}{\mu_{re}} \right] \int_{S_i^{Id}} \hat{n} \cdot \left[ \vec{W}_i \times \vec{H}^{cyl} \right]\, dS$$

$$(9)$$

where $S_i^{ap}$ denotes integration of the aperture associated with the $i^{th}$ unknown, $S_i^{Id}$ is associated with integration over the bounding surface of any

dielectric elements in the exterior region. $\mu_{r_i}$ is the relative permeability of the elements interior to $S_i^{Id}$ whereas $\mu_{r_e}$ is the permeability exterior to that surface.

This set of FE-ABC equations may be written as a linear system of equations

$$\left[\mathcal{A}_{fe-abc}\right] \begin{Bmatrix} E_j^{ap} \\ E_j^{int} \end{Bmatrix} = \begin{Bmatrix} f_i^{ext(abc)} \\ \{f_i^{int}\} \end{Bmatrix} \tag{10}$$

where the FE matrix $\left[\mathcal{A}_{\{1-1\}}\right]$ may be written as a sum of the FE matrix used in the FE-BI formulation [1] and a second term attributed to the ABC surface

$$\left[\mathcal{A}_{\{1-1\}}\right] = [\mathcal{A}] + \left[\mathcal{A}^{1\}}\right] \tag{11}$$

The new FE-ABC equation (9) is comparable to (7) except that the latter utilizes a total field formulation throughout the computational domain. However, previously we utilized an integral expression for the total magnetic field across the aperture which resulted in the FE-BI equation used in [1]. Such an integral expression provides an exact relationship between the total tangential electric and magnetic fields over the aperture surface which also formed the computational domain boundary. Alternatively, we may employ an approximate relationship between these two fields with the goal of retaining the sparsity of the resulting linear system. Additionally, as shown in (9), this FE-ABC formulation may be used for coated as well as uncoated geometries. In the next section, we will develop an approximate relationship suitable for mesh closure.

# 3   Conformal ABCs

Traditional three-dimensional vector ABCs [3, 4] require a spherical outer boundary which results in an excessive number of unknowns. New conformal ABCs have recently been proposed by Chatterjee and Volakis [2] which have an outer boundary that follows the contour of the enclosed geometry resulting in a minimal number of unknowns. In this section, the specific expressions required by this new ABC for a cylindrical-rectangular box boundary will be derived. A definition of ABC order will be given and subsequently the first- and second-order ABC expressions will be presented.

For the purposes of discussion, we define a secondary field as the field which is a consequence of equivalent currents that are supported by some primary source which is either external or internal to the computational domain. Thus for scattering problems, the scattered field is the secondary field while the incident and reflected fields are considered primary fields. Likewise, for a radiation problem, the radiated field is the secondary field whereas the source field due to an impressed current is the primary field. In (9), we recognize that an ABC must supply a relationship between the tangential components of magnetic and electric *secondary* fields on the absorbing boundary, $S^{abc}$.

The secondary field may be expressed as a Wilcox expansion

$$\vec{E}^s(n, t_1, t_2) = \frac{e^{-jk_o n}}{4\pi\sqrt{u}} \lim_{P\to\infty} \sum_{p=0}^{P} \frac{\vec{E}_p^s(t_1, t_2)}{u^p} \tag{12}$$

where $u = \sqrt{R_1 R_2}$, $R_i = \rho_i + n$ and $\rho_i$ is a principal radius of curvature. In this form, the curvature of the non-spherical wavefront is explicitly used. The point of observation is given in Dupin coordinates as

$$x = n\hat{n} + \vec{x}_o(t_1, t_2) \tag{13}$$

where $\hat{n}$ is the unit normal and $\vec{x}_o(t_1, t_2)$ denotes the surface of the reference phase front and therefore, $t_1$ and $t_2$ denote tangential coordinates on that surface. Absorbing boundary conditions annihilate outward propagating waves up to a certain order. A zeroth-order (P = 0) ABC represents the usual Sommerfeld radiation condition. A first-order ABC (P = 1) annihilates all fields with up to a $u^{-1}$ dependency while all higher order fields are reflected back into the computational domain. For a cylindrical surface, $u = \sqrt{\rho}$, thus the zeroth-order ABC is simply the geometrical optics spread factor while the first order ABC annihilates fields up to $\mathcal{O}(\rho^{-\infty})$. Evidently, as the ABC order increases, the reflected fields have an increasingly higher attenuation factor and hence the boundary may be placed closer to the geometry without inducing erroneous reflections.

We present the second order conformal ABCs attributed to Chatterjee and Volakis[2]. In particular, the appropriate expressions for a cylindrical-rectangular box boundary will be given.

Absorbing boundary conditions provide a local relationship between the electric field and its curl which may be approximated as

$$\hat{n} \times \nabla \times \vec{E}^s = \overline{\overline{\alpha}} \cdot \vec{E}_t^s + \overline{\overline{\beta}} \cdot \nabla \times \left[\hat{n}\left(\hat{n} \cdot \nabla \times \vec{E}^s\right)\right] + \overline{\overline{\gamma}} \cdot \nabla_t\left(\hat{n} \cdot \vec{E}^s\right) \tag{14}$$

where $\nabla_t$ denotes the tangential surface gradient operator. Unfortunately, use of (14) would result in an asymmetric system $\left[\mathcal{A}^{\dashv \sqcup}\right]$ due to the last term which possesses only one differential operator. An asymmetric system requires an iterative solver which utilizes two vector-matrix products such as the conjugate gradient squared (CSG) solver such as the one presented by [5]. A symmetric system requires only one matrix-vector product if the BiCG solver is used. Additionally, for symmetric systems, only the upper or lower triangle of the matrix need be computed and stored.

The gradient in (14) may be approximated by

$$\nabla_t \left(\nabla \cdot \vec{E}_t^s\right) = jk_o \nabla_t \left(\hat{n} \cdot \vec{E}^s\right) + \mathcal{O}\left(\backslash^{-\nabla}\right) \tag{15}$$

With both a gradient and a divergence operator present, one operator can be transferred to the test vector while the other may remain with the source vector. Hence, the resulting matrix *may* be symmetric since both the test and source fields are differentiated. With (15), (14) may be written

$$\hat{n} \times \nabla \times \vec{E}^s = \overline{\overline{\alpha}} \cdot \vec{E}_t^s + \overline{\overline{\beta}} \cdot \nabla \times \left[\hat{n}\left(\hat{n} \cdot \nabla \times \vec{E}^s\right)\right] + \overline{\overline{\gamma}} \cdot \nabla_t \left(\nabla \cdot \vec{E}_t^s\right) \tag{16}$$

For the basis vectors used in [1], $\nabla \cdot \vec{E}_t^s$ is always zero on $S^{abc}$ and hence the third term of (16) will not contribute to this form of the ABC. For surfaces with a common constant curvature for both tangential directions on a surface, this new vector ABC (16) will lead to a symmetric FE system $\left[\mathcal{A}^{\dashv \sqcup}\right]$. However, if the principal curvatures on a surface are unequal, the system will be asymmetric. For either (14) or (16), the three coefficient dyads are given by

$$\overline{\overline{\alpha}} = \sum_{i=1}^{2}\left\{\frac{\hat{t}_i\hat{t}_i}{D - \Delta\kappa - 2\kappa_i}\left[4\kappa_m^2 - \kappa_g + D\left(jk_o - \kappa_i\right) + \kappa_i^2\right]\right\}$$

$$\overline{\overline{\beta}} = \sum_{i=1}^{2}\left\{\frac{\hat{t}_i\hat{t}_i}{D - \Delta\kappa - 2\kappa_i}\right\}$$

$$\overline{\overline{\gamma}} = \sum_{i=1}^{2}\left\{\frac{1}{\left(D - \Delta\kappa - 2\kappa_i\right)}\left[jk_o + 3\kappa_m - \frac{\kappa_g}{\kappa_m} - 2\kappa_i\right]\hat{t}_i\hat{t}_i\right\} \tag{17}$$

where $\kappa_g = \kappa_1\kappa_2$, $\Delta\kappa = \kappa_1 - \kappa_2$ and $D = jk_0 + 5\kappa_m - \frac{\kappa_g}{\kappa_m}$. In the case of (16), $\overline{\overline{\gamma}}$ must be divided by $jk_o$ due to (15).

48

It is advantageous to consider the second-order ABC for singly curved and flat surfaces separately. For a singly curved surface, the unit normal direction and curvature parameters are $\hat{n} = \hat{\rho}$, $\kappa_1 = -\frac{1}{\rho}$ and $\kappa_2 = 0$ as before. After some manipulation, we find that (17) becomes

$$
\begin{aligned}
\overline{\overline{\alpha}} &= \frac{2\rho}{j2k_o\rho + 1}\left[\frac{2}{\rho^2} + D\left(jk_o + \frac{1}{\rho}\right)\right]\hat{\phi}\hat{\phi} + \frac{2\rho}{j2k_o\rho - 3}\left[\frac{1}{\rho^2} + jk_oD\right]\hat{z}\hat{z} \\
\overline{\overline{\beta}} &= \frac{2\rho}{j2k_o\rho + 1}\hat{\phi}\hat{\phi} + \frac{2\rho}{j2k_o\rho - 3}\hat{z}\hat{z} \\
\overline{\overline{\gamma}} &= \left[\hat{\phi}\hat{\phi} + \hat{z}\hat{z}\right]
\end{aligned}
\tag{18}
$$

where $D = jk_o - \frac{5}{2\rho}$. Note that $\overline{\overline{\beta}}$ is not symmetric unless $\rho \to \infty$

For the second-order ABC, it is advantageous to segment the matrix entry $\left[\mathcal{A}^{-1}\mathsf{U}\right]$ into three parts. After some vector manipulation, these contributions are given by

$$
\begin{aligned}
I^{(1)abc} &= \int_{S_t^{abc}} \vec{W}_i \cdot \left[\overline{\overline{\alpha}} \cdot \vec{W}_j\right] \, dS \\
I^{(2)abc} &= \int_{S_t^{abc}} \left[\hat{n} \cdot \nabla \times \vec{W}_i\right]\left[\hat{n} \cdot \nabla \times \left(\overline{\overline{\beta}} \cdot \vec{W}_j\right)\right] \, dS \\
I^{(3)abc} &= \int_{S_t^{abc}} \vec{W}_i \cdot \left[\overline{\overline{\gamma}} \cdot \nabla_t\left(\hat{n} \cdot \vec{W}_j\right)\right] \, dS
\end{aligned}
\tag{19}
$$

where $I^{(3)abc}$ is only used for the original, asymmetric ABC (14). Closed form expressions for these three integrals may be readily found by utilizing the vector basis functions given in [1]. As mentioned previously, since the principal radii of curvature are not identical for a cylindrically curved surface, $I^{(2)abc}$ will not be symmetric. However, these terms are asymptotically identical as the radius of the ABC surface becomes large since the surface will then be approximately planar. A symmetric ABC may be obtained by dividing both the numerator and the denominator of $I^{(2)abc}$ by the ABC radius, $\rho$, which results in a symmetric operator.

# 4   Radiation Integral

Not surprisingly, since the FE-ABC method is being proposed for modelling more complex geometries than the FE-BI method presented previously by the

authors [1], some support task such as computation of the far-zone radiated fields must become necessarily more complex.

The radiation integral for computing the far-zone radiated fields previously was confined to the surface of the cylinder for uncoated antennas. This field was solely due to radiating magnetic currents in the aperture of the cavity due to the use of a second kind dyadic Green's function (see [1] for details). However, when a overlay or a protruding element is present, the radiation integral must contain such material. Thus, for this work, the radiation integration surface is deformed to contain any material above the cavity. To do so, both electric and magnetic currents over this blister must be used along with both the first and second kind dyadic Green's functions.

# 5 Results

The aforementioned FE-ABC has been implemented and in this section, it will be used to examine the radiation and input impedance properties of conformal patch antennas with dielectric overlays. However, the formulation's accuracy must first be established via comparison with the FE-BI method presented previously by the authors [1].

Consider a 2 cm × 3 cm patch antenna residing atop a 5 cm × 6 cm × 0.07478 cm dielectric filled cavity. This substrate has a dielectric constant of 2.17 and the cylinder radius is 15.27887 cm. The patch antenna is fed as to excite a pure axial mode ($\phi_s = 0^\circ, z_s = -0.375$ cm). Figure 2 compares the FE-ABC and FE-BI formulations. In this, data was taken from 3.0 GHz to 3.2 GHz every 5 MHz. The agreement is quite good and we find that the resonant frequency is 3.11 GHz. At this frequency, the H-plane radiation pattern is shown in figure 3.

The previous example involved a single antenna element placed within a discrete cavity with a minimal ABC surface. Since no superstrate was present, the exterior region of the computational domain was limited to the immediate vicinity of the cavity. However, if a dielectric coating is used, a continuous wraparound exterior region is desirable. In this way, the physics involved in substrate mode guided waves is included explicitly in the finite element analysis. The next example utilizes such a computational domain where the exterior region extends a full 360° around the cylinder while its axial length is limited. Furthermore, the discrete cavity which contains the

50

antenna element is minimized.

To consider the effect of a dielectric overlay, Ke and Wong [6] examined the antenna used by Dahele *et. al.* in [7] which is 3 cm × 4 cm and fed to excite a pure axial mode ($\phi_s = 0^o, z_s = 1.0$ cm). The substrate is 0.0795 cm thick with a dielectric constant of 2.32. Figure 4 compares the H-plane pattern of this antenna for uncoated and with a 0.3975 cm dielectric cover which is identical in material parameters with the substrate. In this, each antenna was excited at their resonant frequencies, 3.0 GHz and 2.91 GHz, respectively. Note that, as one might expect, there is no change between the antenna pattern associated with the coated and uncoated antennas. The agreement with the corresponding E-plane pattern is shown in figure 5. However, a slight beam broadening is observed rather than narrowing as predicted by Ke and Wong [6]. The differences may likely be due to the finite cavity aperture in our calculations whereas in [6] the coating and substrate were assumed to cover the entire cylinder. Further communication will be conducted with the authors of [6] to clear up this area of disagreement.

In the previous example, the resonance frequency was seen to shift due to the presence of the dielectric overlay. Such a shift is illustrated in figure 6 which shows the input resistance of a 2 cm × 3 cm patch antenna (see figure 2) with different overlay thickness. In this example, the substrate and superstrate are identical material ($\epsilon_r = 2.17$).

# 6 Comments

In this report, we have presented a new application for the FE-ABC method which has been developed at the Radiation Laboratory: radiation analysis of conformal antennas mounted on an infinite cylinder. We have sketched the formulation and presented some initial validation results. Currently, this new FE-ABC formulation has matched data generated by a FE-BI method for uncoated patch antennas. We have presented some preliminary data for patch antennas with dielectric overlays and are currently seeking appropriate measured data. In this report, only axial polarization was considered. Circumferential polarization should also be studied with emphasis on dielectric overlay effects.

Initial results are promising and correspond to expectation. It should be stressed that this new FE-ABC approach is considerably more flexible than

previously developed FE-BI methods since it permits material or protruding elements in the exterior region of the cylinder. We will explore the utility of this approach for inhomogeneous coatings, complex protruding antennas, etc. in future reports.

# References

[1] L.C. Kempel and J.L. Volakis, "A finite element-boundary integral method for cavities in a circular cylinder," *1993 IEEE Antennas and Propagat. Soc. Int. Symp.*, Vol. 1, pp. 292-295, June 1993.

[2] A. Chatterjee and J.L. Volakis, "Conformal absorbing boundary conditions for the vector wave equation," *Microwave Opt. Technol. Lett.*, Vol. 6, pp. 886-889, Dec. 1993.

[3] A.F. Peterson, "Absorbing boundary conditions for the vector wave equation," *Microwave Opt. Technol. Lett.*, Vol. 1, pp. 62-64, April 1988.

[4] J.P. Webb and V.N. Kanellopoulos, "Absorbing boundary conditions for finite element solution of the vector wave equation," *Microwave Opt. Technol. Lett.*, Vol. 2, pp. 370-372, Oct. 1989.

[5] H.A. van der Vorst, "BI-CGSTAB: A fast and smoothly converging variant of BI-CG for the solution of nonsymmetric linear systems," *SIAM J. Sci. Stat. Comput.*, Vol. 13, No. 2, pp. 631-644, Mar. 1992.

[6] S-Y Ke and K-L Wong, "Full wave analysis of probe-fed superstrate-loaded rectangular microstrip antennas on a cylindrical body," *1994 IEEE Antennas and Propagat. Soc. Int. Symp.*, Vol. 3, pp. 2224-2227, June 1994.

[7] J.S. Dahele, R.J. Mitchell, K.M. Luk and K.F. Lee, "Effect of curvature on characteristics of rectangular patch antenna," *Electronics Letters*,Vol. 23, No. 14, pp. 748-749, 1987.
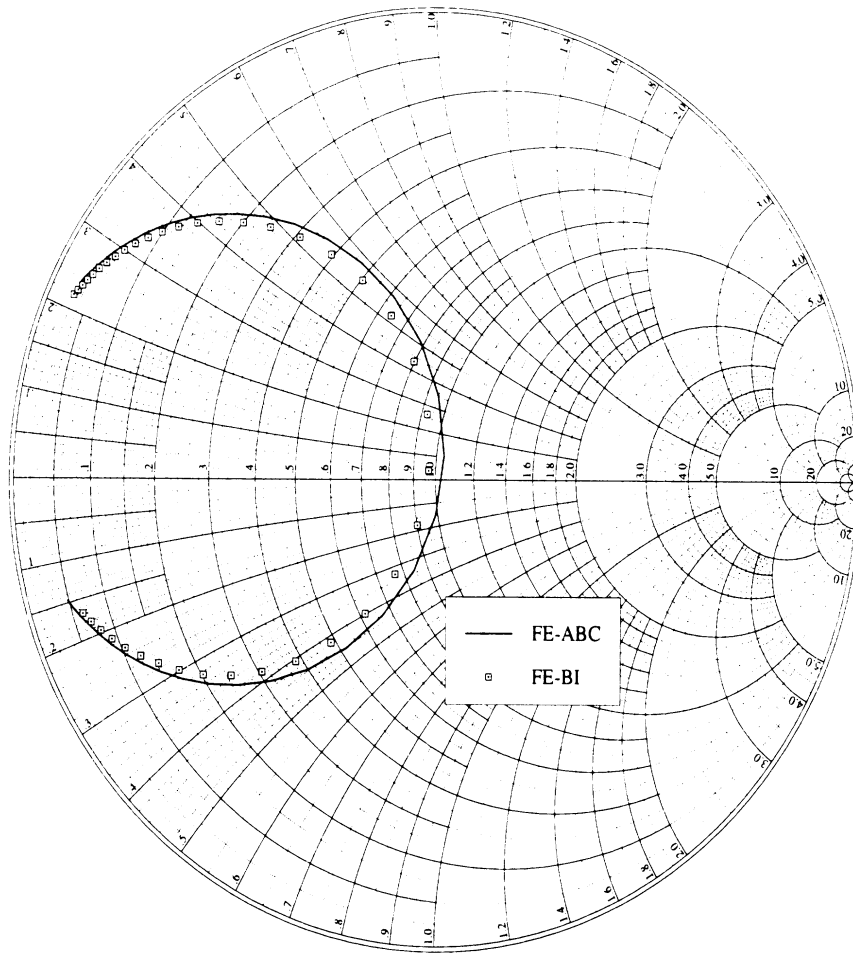
Figure 2: Input impedance for the axially polarized patch antenna which is 2 cm × 3 cm in a 5 cm × 6 cm × 0.07874 cm cavity. The frequency range is 3.0 to 3.2 GHz with data taken every 5 MHz.
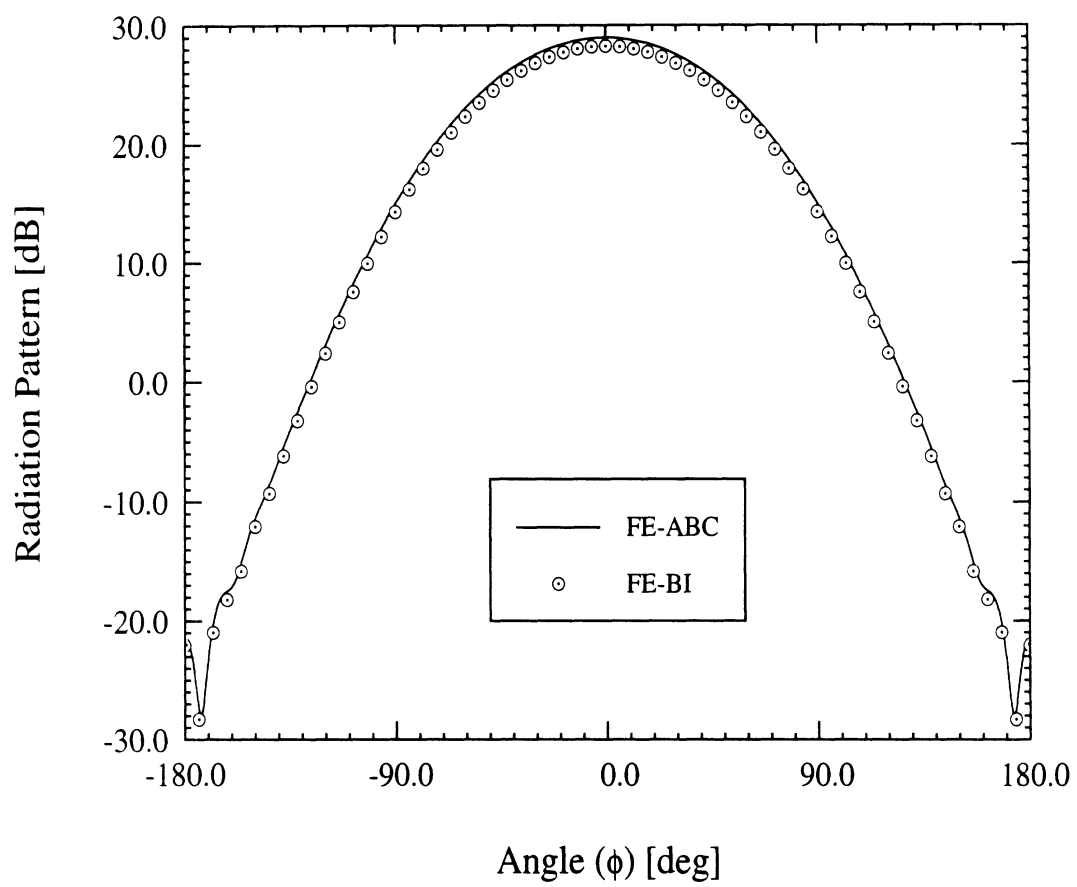
Figure 3: Radiation pattern for a patch antenna which is 2 cm × 3 cm in a 5 cm × 6 cm × 0.07874 cm cavity operated at 3.11 GHz.
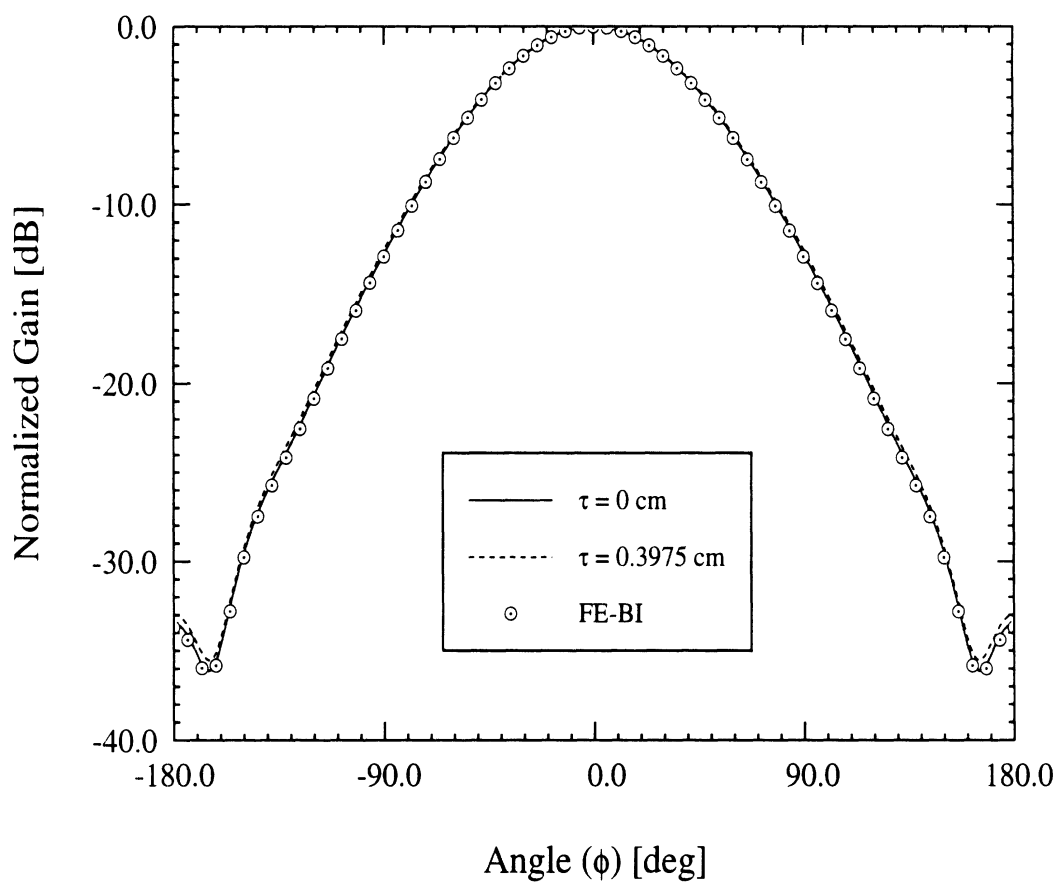
Figure 4: H-plane radiation pattern for a patch antenna which is 4 cm × 3 cm in a 8 cm × 6 cm × 0.0795 cm cavity with different overlay thickness. The dielectric constant of the overlay and the substrate is 2.32 and the feed point is ($\phi_s = 0^o, z_s = 1.0$ cm).
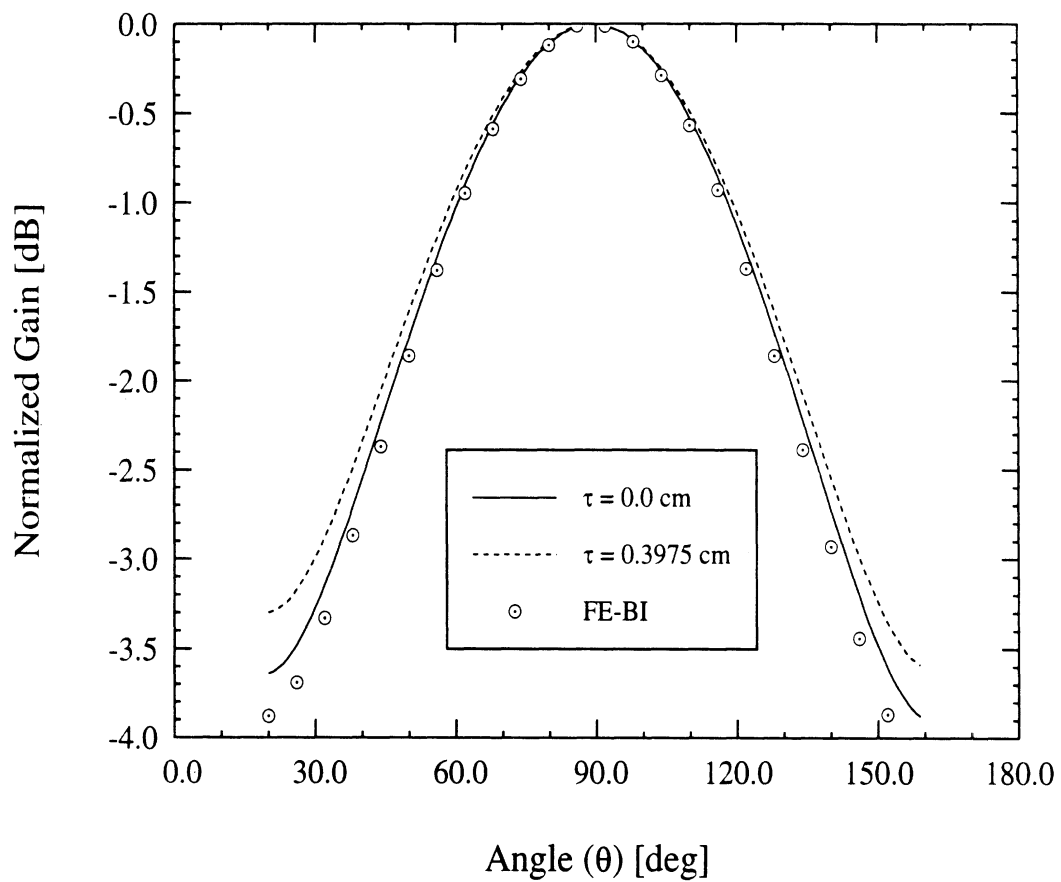
Figure 5: E-plane radiation pattern for a patch antenna which is 4 cm × 3 cm in a 8 cm × 6 cm × 0.0795 cm cavity with different overlay thickness. The dielectric constant of the overlay and the substrate is 2.32 and the feed point is ($\phi_s = 0^o, z_s = 1.0$ cm).
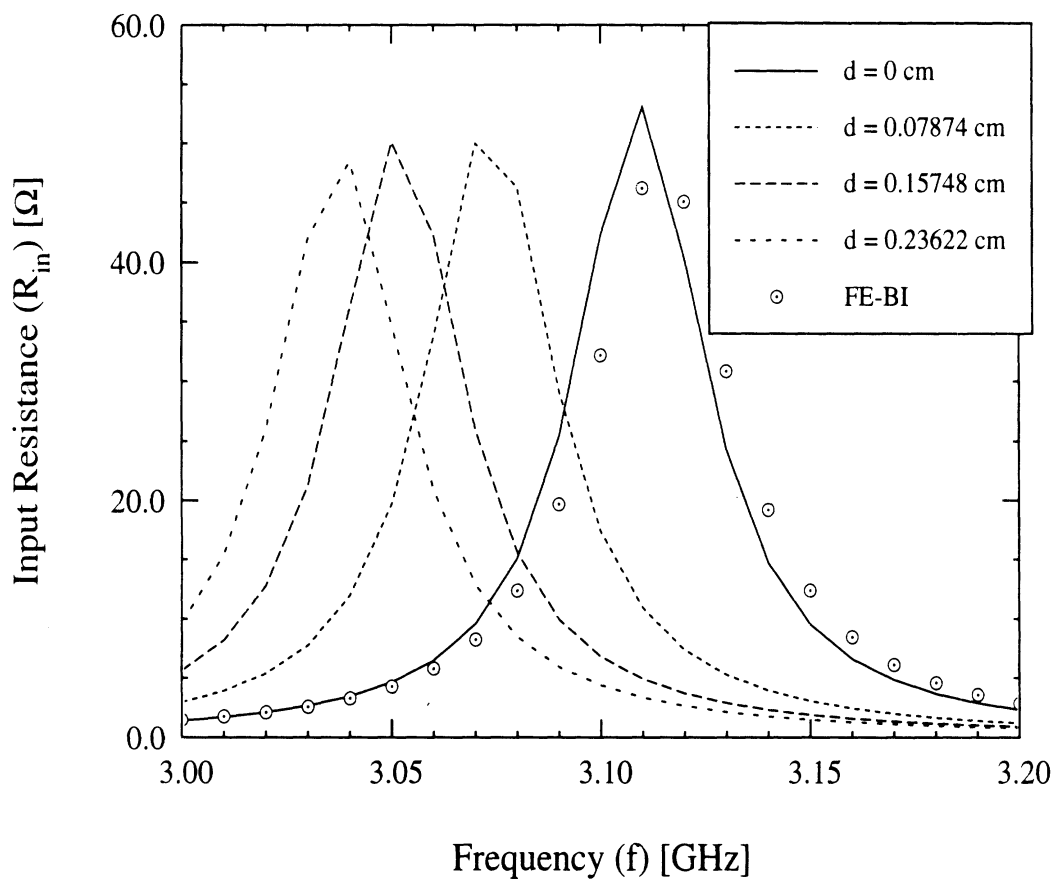
Figure 6: Input resistance for a patch antenna which is 2 cm × 3 cm in a 5 cm × 6 cm × 0.07874 cm cavity with different overlay thickness. The dielectric constant of the overlay and the substrate is 2.17 and the feed point is ($\phi_s = 0°, z_s = -0.375$ cm).

# An Efficient and Accurate Model Of The Coax Cable Feeding Structure For FEM Simulations

Jian Gong and John L. Volakis,

Radiation Laboratory
Department of Electrical Engineering
and Computer Science
The University of Michigan
Ann Arbor MI 48109-2122

## Abstract

An efficient and accurate coax cable feed model is proposed for microstrip or cavity-backed patch antennas in the context of a hybrid finite element method (FEM). A TEM mode at the cavity-cable junction is assumed for the FEM truncation and system excitation. Of importance in this implementation is that the cavity unknowns are related to the model fields by enforcing an equi-potential condition rather than field continuity. This scheme proved quite accurate and may be applied to other decomposed systems as a connectivity constraint. Comparisons of our predictions with input impedance measurements are presented and demonstrate the substantially improved accuracy of the proposed model.

# I. Introduction

The coax cable is widely used as a feeding structure for microstrip or cavity-backed patch antennas because of its simplicity and low spurious radiation. Indeed, abundant literature exists on the theoretical and experimental investigation of coax cable feeds [1]-[3]. Most of these papers present integral equation techniques in conjunction with the pertinent Green's functions. However, the Green's function is only available for a certain class of geometries, and this limits the application of the integral techniques to those geometry designs. Also, the formulation must be modified and recoded for different antenna configurations corresponding to Green's function variations. To avoid the complexity of the Green's function, a hybrid finite element – boundary integral approach [5] was recently proposed to simulate cavity-backed antennas of arbitrary shapes. For antenna radiation it is observed that a simple

probe model with a constant current along the inner conductor linking the grounded base to the antenna element is straightforward and efficient. But the probe feed is only valid for thin substrates and this is consistent with the Moment Method (MM) results. To model an electrically thick substrate, in this communication we propose a more sophisticated feed modeling scheme in the context of the finite element method (FEM) using linear edge-based tetrahedral elements. In the next section, the formulation of the entire hybrid numerical system is first described for reference purposes. The proposed feed model is then presented in section III on the basis of a TEM mode excitation. Model improvements are also discussed for the case when the TEM assumption at the cavity-cable junction does not hold. Input impedance comparisons between measurements and predictions based on this technique are presented in section IV.

## II. Hybrid FE–BI System

The functional pertinent to the radiation by a cavity-backed antenna with a coax cable feed (as shown in figure 1) is given by

$$
\begin{aligned}
F(\mathbf{E}) \;=\; & \frac{1}{2} \iiint_V \left\{ (\nabla \times \mathbf{E}) \cdot \frac{1}{\mu_r} (\nabla \times \mathbf{E}) - k_0^2 \epsilon_r \mathbf{E} \cdot \mathbf{E} \right\} dv \\
& - 2k_0^2 \iint_S (\mathbf{E} \times \hat{z}) \cdot \left\{ \iint_{S'} (\mathbf{E} \times \hat{z}) \cdot \left( \bar{\mathbf{I}} + \frac{1}{k_0^2} \nabla \nabla \right) G_0(\mathbf{r}, \mathbf{r}') \, dS' \right\} dS \\
& - j k_0 Z_0 \iint_C (\mathbf{E} \times \mathbf{H}) \cdot \hat{z} \, dS,
\end{aligned}
\tag{1}
$$

where V refers to the cavity volume and the surface S encompasses the cavity aperture excluding the portion occupied by the metallic antenna elements; $\epsilon_r$ and $\mu_r$ denote, respectively, the relative permittivity and permeability; $k_0$ is the free space wave number, $Z_0$ is the free space intrinsic wave impedance, $\bar{\mathbf{I}}$ is the unit dyad, and $G_0(\mathbf{r}, \mathbf{r}')$ is the free space Green's function with $\mathbf{r}$ and $\mathbf{r}'$ denoting the observation and integration points; the surface C is the cross section of the coax cable at the cavity–cable junction.

Following the standard discretization procedure [5], we obtain a system of equations of the form

$$
\sum_{e=1}^{N_e} \left\{ [A_{ij}^e]\{E_j^e\} \right\} + \sum_{e \in S}^{N_S e} \left\{ [B_{ij}^e]\{E_j^e\} \right\} + \sum_{e \in C}^{N_C e} \frac{\partial F_C(\mathbf{E}, \mathbf{H})}{\partial E_i} = 0,
\tag{2}
$$

where the explicit expressions for $A_{ij}$ and $B_{ij}$ may be found in [5] and the functional term $F_C$ is the surface integral on C in (1) . It is apparent that the system excitation is associated with the functional $F_C$ whose evaluation is the subject of this communication.

## III. Coax Cable Feed Modeling

To proceed with the evaluation of

$$
F_C = -j k_0 Z_0 \iint_C (\mathbf{E} \times \mathbf{H}) \cdot \hat{z} \, dS,
\tag{3}
$$

a boundary constraint relating **E** to **H** is needed. To this end, we assume a TEM mode on C and consequently the fields within the cavity may be expressed as (see Figure 2)

$$\mathbf{E} = \frac{I_0 Z_0}{2\pi\sqrt{\epsilon_{rc}}}(1+\Gamma)\frac{1}{r}\hat{r}, \quad \mathbf{H} = \frac{I_0}{2\pi}(1-\Gamma)\frac{1}{r}\hat{\phi}, \tag{4}$$

where $\epsilon_{rc}$ is the relative permittivity inside the coax cable; $\Gamma$ denotes the reflection coefficient measured at $z = 0$ and $I_0$ is the given input current source at the same location. Also, $(r, \phi, z)$ are the polar coordinates of a point in the cable with the center at $r = 0$. To simplify the analysis, we introduce the quantities

$$e_0 = \frac{I_0 Z_0}{2\pi\sqrt{\epsilon_{rc}}}(1+\Gamma), \quad h_0 = \frac{I_0}{2\pi}(1-\Gamma). \tag{5}$$

Hence,

$$\mathbf{E} = \frac{e_0}{r}\hat{r}, \quad \mathbf{H} = \frac{h_0}{r}\hat{\phi}, \tag{6}$$

and from (5) it follows

$$h_0 = -\frac{\sqrt{\epsilon_{rc}}}{Z_0}e_0 + \frac{I_0}{\pi}, \tag{7}$$

which is the desired constraint at the cable junction in terms of the new quantities $h_0$ and $e_0$. Note that $e_0$ and $h_0$ are field coefficients as new unknowns in place of the fields **E** and **H**, and it is therefore appropriate to rewrite $F_C$ in terms of these new coefficients. To do so, we substitute (5) and (7) into (3) and upon making use of the axisymmetric field property we obtain

$$F_C = -2\pi j k_0 Z_0 e_0 h_0^{src} ln(\frac{b}{a}), \tag{8}$$

where a and b are the radii of the inner and outer cable conductors. The superscript *src* stands to indicate that $h_0$ is treated as a source term in the extremization of the functional.

We choose the linear edge-based tetrahedral elements to discretize the cavity and the corresponding mesh on the cross section C is shown in Figure 2(b). In this formulation, the field across the $p^{th}$ edge, p=1,2,..., $N_C$ ($N_C$ is the number of cavity mesh edges on C), is set to a constant as dictated by the linear edge-based expansion function inside the cavity. However, the cable TEM modal fields (4) behave as $1/r$ and this modeling inconsistency makes it difficult to apply the tangential field continuity condition at the cable junction ( i.e. over the aperture C). To overcome these difficulties, we can relate the fields across the cable junction by recognizing that the potential difference between the inner and outer conductors must be the same as computed by the fields of the cavity or those in the cable region. Specifically, if the $N_p^{th}$ edge of the cavity region borders and is also across the coax cable, from (4)-(6) it then follows that the appropriate equi-potential condition is

$$\Delta V = E_i(b-a) = e_0 ln\frac{b}{a}, \quad i = N_p(p = 1,2,...,N_C). \tag{9}$$

where $\Delta V$ denotes the potential difference between the inner and outer surface of the cable. This condition simply provides a relation between the constant cavity edge field and the coax cable modal field. When used into the functional $F_C$, it introduces the excitation into the hybrid finite element system without a need to extend the mesh inside the cable or to employ a fictitious current probe. It remains to rewrite $F_C$ in terms of $E_i$, i.e. the field value of the edges bordering the cable and to do so we substitute (7) and (9) into (8). Then upon taking into account all $N_C$ cavity mesh edges on the cable junction, we obtain

$$
F_C = -\frac{\pi}{3} j k_0 Z_0 (b-a) \left\{ \frac{I_0}{\pi} - \frac{\sqrt{\epsilon_{rc}}}{Z_0} \frac{b-a}{ln\frac{b}{a}} E_i \right\}^{src} \sum_{i=N_p}^{N_C} E_i .
\tag{10}
$$

In this expression, rather than representing the functional $F_C$ in terms of a single edge field, we made use of the average field across the cable as computed by the totality of the equal element fields on the cable's aperture (because of the axisymmetric property, all elements fields at the cable's aperture are equal). The factor inside the curly brackets of (10), with the superscript $src$, functions as a source in the extremization process. Hence, the extremization of (10) yields

$$
\begin{aligned}
\frac{\partial F_C}{\partial E_i} &= -\frac{1}{3}\pi j k_0 Z_0 (b-a) \left\{ \frac{I_0}{\pi} - \frac{\sqrt{\epsilon_{rc}}}{Z_0} \frac{b-a}{ln\frac{b}{a}} E_i \right\} \\
&= U_i E_i - V_i, \quad i = N_p (p = 1, 2, ... N_C),
\end{aligned}
\tag{11}
$$

where

$$
U_i = j\frac{1}{3}\pi k_0 \sqrt{\epsilon_{rc}} \frac{(b-a)^2}{ln\frac{b}{a}}
\tag{12}
$$

$$
V_i = j\frac{1}{3} k_0 Z_0 (b-a) I_0 .
\tag{13}
$$

We observe that the 'constant cavity field' along each mesh edge at the cable junction is just a fictitious field representation and its meaningful physical interpretation is governed by the equi–potential constraint (9). To proceed, we assemble the FEM system together with (11). Specifically, each $U_i$ is added to the $N_C$ diagonal entries of the finite element matrix which is associated with the $N_C$ edges bordering the coax cable. Also, the excitation column of the hybrid system is nullified everywhere except for the $N_C$ entries which are set to $V_i$. Once the hybrid FE-BI system is solved [5], the input admittance at z=0 is calculated from

$$
\begin{aligned}
Y_{in} &= \frac{1}{V_0} \oint_{2\pi} \mathbf{H} \cdot \hat{r} \, r d\phi \\
&= \frac{2I_0}{e_0 ln(\frac{b}{a})} - \frac{1}{Z_C} .
\end{aligned}
\tag{14}
$$

where $Z_c$ is the characteristic impedance of the coax cable.

In the above feed model we assumed the presence of only the dominant(TEM) mode at the cavity-cable junction, an assumption which may not be suitable for certain applications.

To overcome this limitation, one approach is to extend the mesh (say, a distance d) into the cable. The equi–potential condition will then be applied at z=-d, where all higher order modes vanish. This scheme requires a more suitable expansion for the fields in the $-d < z < 0$ section to avoid the complication of extending the tetrahedral mesh into the cable and, thus, retain the efficiency of the equi–potential feed model. Since the antenna is, in most cases, operated in the frequency range far below the cut–off of the first higher order mode of the coax cable, the field distribution near the junction C will still be dominated by the fundamental TEM mode. With this understanding, a possible suitable expansion for the field in the coax cable (using shell elements rather than tetrahedrals) is

$$\mathbf{E} = \sum_q \sum_i^4 E_q^i \frac{\mathbf{N}_q^i(r,\phi,z)}{r}, \tag{15}$$

where q=r, $\phi$ or z, i=1,2,3 or 4 and $\mathbf{N}_q^i(r,\phi,z)$ is defined as

$$\mathbf{N}_{q_a}^i = \frac{\tilde{\epsilon}_i}{\Delta q_b \Delta q_c}(q_b - q_b')(q_c - q_c')\hat{q}_a \tag{16}$$

with $q_a, q_b$ and $q_c$ representing $r, \phi$ and $z$ in a cyclic rotation. Also, i denotes the edge number along each coordinate, and $\Delta q_a$ is the width of the edge along the $\hat{q}_a$ direction. The correspondence between the edge numbers and the node pairs for each coordinate($r, \phi$ or $z$) is given in Table 1 along with the definition of the primed parameters and $\tilde{\epsilon}_i$ which carries the sign of the vector basis.

## TABLE1

| coordinates q | i | node pairs | $\tilde{\epsilon}$ | $r'$ | $\phi'$ | $z'$ |
|---|---|---|---|---|---|---|
| | | | parameters | | | |
| r | 1 | (1-2) | + | | $\phi_1 + \Delta\phi$ | $z_1 + \Delta z$ |
| | 2 | (4-3) | - | | $\phi_1$ | $z_1 + \Delta z$ |
| | 3 | (8-7) | + | | $\phi_1$ | $z_1$ |
| | 4 | (5-6) | - | | $\phi_1 + \Delta\phi$ | $z_1$ |
| $\phi$ | 1 | (1-4) | + | $r_1 + \Delta r$ | | $z_1 + \Delta z$ |
| | 2 | (5-8) | - | $r_1 + \Delta r$ | | $z_1$ |
| | 3 | (6-7) | + | $r_1$ | | $z_1$ |
| | 4 | (2-3) | - | $r_1$ | | $z_1 + \Delta z$ |
| z | 1 | (1 5) | + | $r_1 + \Delta r$ | $\phi_1 + \Delta\phi$ | |
| | 2 | (2 6) | - | $r_1$ | $\phi_1 + \Delta\phi$ | |
| | 3 | (3 7) | + | $r_1$ | $\phi_1$ | |
| | 4 | (4 8) | - | $r_+\Delta r$ | $\phi_1$ | |
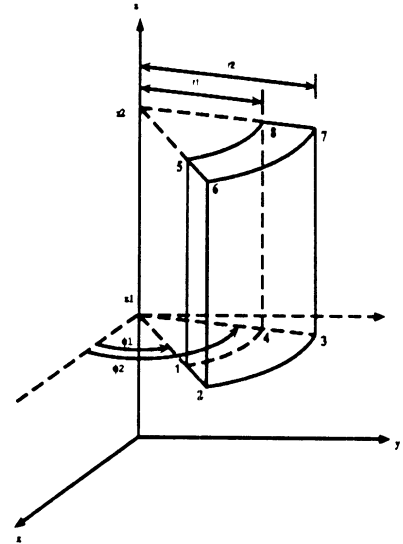
When an axisymmetric field property is assumed, the expansions reduce to

$$N_r^1 = \frac{(z - z_1)}{\Delta z}, \quad N_r^2 = -\frac{(z - z_1 - \Delta z)}{\Delta z}$$

$$N_z^1 = \frac{(r - r_1)}{\Delta r}, \quad N_z^2 = -\frac{(r - r_1 - \Delta r)}{\Delta r} \tag{17}$$

where $(r_1, \phi_1, z_1)$ denote the coordinates of node 1. The accuracy of expansion (17) is demonstrated in Figure 3. where we show that only 3 elements are needed along the radial direction for the accurate prediction of the dominant field distribution. When compared to the conventional linear tetrahedral elements, the efficiency of this expansion is apparent (i.e., many more tetrahedrals are needed to model the same cable region).

# IV. Results and Conclusion

To validate our proposed feed simulation, two circular patch antenna configurations were used for calculation. One patch antenna was of radius 1.3 cm printed atop of a circular cavity (radius=2.1 cm) filled with a dielectric ($\epsilon_r$=2.9) material 0.41 cm deep. For this patch, the feed was placed 0.8 cm from the center and the input impedance was measured over the band 2 – 5 GHz. In Figure 4 we compare the measured input impedance with data computed on the basis of the proposed equi-potential feed model. Clearly, the results from measurements and the equi–potential model are in excellent agreement whereas the probe model yields substantially inaccurate results near resonance.

Figure 5 shows the comparison between measurements and calculations for another patch antenna whose input impedance was measured by Aberle and Pozar [6]. This patch had a radius of 2.0 cm and the 0.218 cm thick substrate had $\epsilon_r$=2.33 and a loss tangent tan$\delta$=0.0012. The feed was located 0.7 cm from the center, and for our FE-BI calculation the patch was placed in a circular cavity of 2.44 cm in radius. As shown in Figure 5, the equi-potential model is again in excellent agreement with measurements, as opposed to the results by the probe model in [6] .

In conclusion, the presented equi–potential feed model has been shown to be extremely accurate in modeling coax feed structures. Moreover, its implementation in the context of a finite element formulation is very simple and as easy to implement as the probe feed. It was also demonstrated how the proposed feed model can be generalized to the case of asymmetric feed structures where evanescent modes may be present.

# References

[1] J.P. Damiano and A. Papiernik, "Survey of Analytical and Numerical Models for Probe-fed Microstrip Antennas," *IEE Proc. H.*, Vol. 141, No. 1, pp. 15–22, February, 1994

[2] J Zheng and D.C. Chang, "End-Correction Network of a Coaxial Probe for Microstrip Paths Antennas,' *IEEE Trans. Antennas Propagat.*, Vol. 39, No.1,pp. 115–118, January 1991

[3] W.C. Chew, Z. Nie, Q.H. Liu and Y.T. Lo, "Analysis of a probe-fed microstrip disk antennas," *IEE Proc. H*, Vol. 138, No. 2, pp. 185–191, 1991.

[4] J.L. Volakis, J. Gong and A. Alexanian, "Electromagnetic Scattering From Microstrip Patch Antennas and Spirals Residing in a Cavity," *Electromagnetics*, Vol. 14, No. 1, pp 63–85, 1994

[5] J. Gong, J.L. Volakis. A.C. Woo and H.G. Wang, "A Hybrid Finite Element-Boundary Integral Method for the Analysis of Cavity-backed Antennas of Arbitrary Shape," To appear in *IEEE Trans Antenna and Propagat.*, September 1994

[6] J.T. Aberle, D.M. Pozar and C.R. Birtcher,"Evaluation of Input Impedance and Radar Cross Section of Probe-Fed Microstrip Patch Elements using an Accurate feed model," *IEEE Trans. Antennas Propagat.*, Vol. 39, No.12, pp. 1691-1696. Dec. 1991

# List of Figures

Figure 1: Illustration of a cavity-backed patch antenna with a coax cable feed.



**(a)**

**(b)**
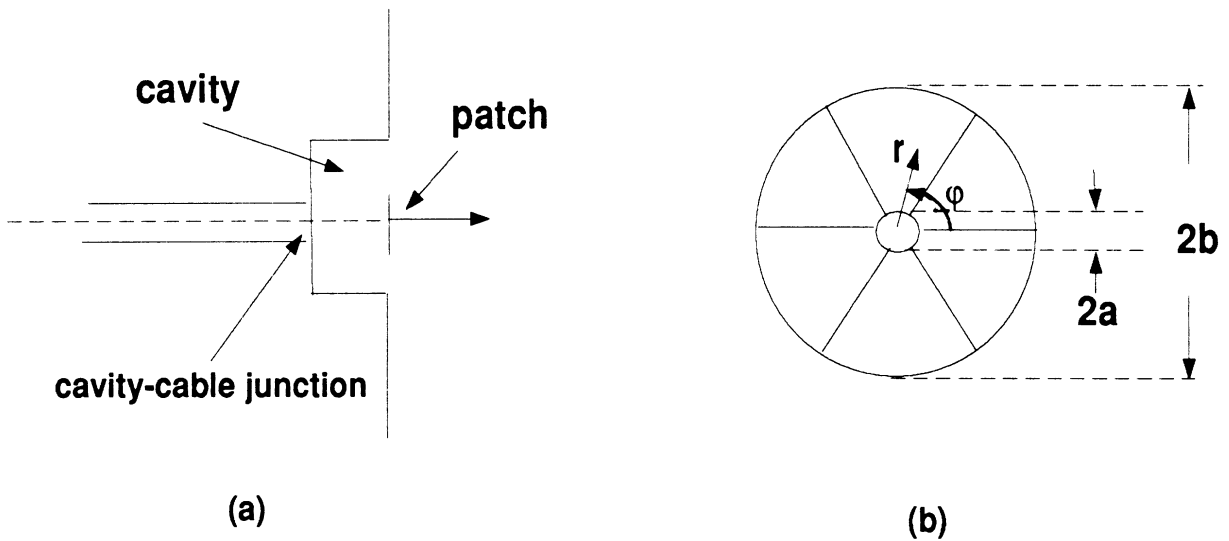
Figure 2: (a) Side view of a cavity-backed antenna with a coax cable feed; (b) Illustration of the FEM mesh at the cavity-cable junction.
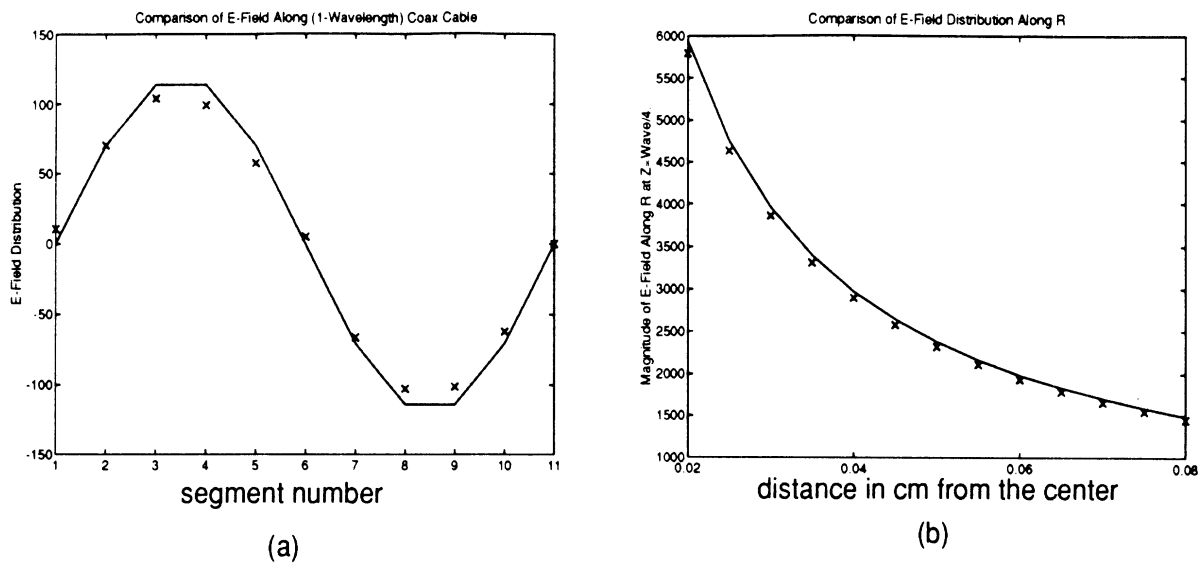
Figure 3: Field distribution in a shorted coax cable as computed by the finite element method using the expansion (14). —: analytical; xxx: numerical. (a) Field coefficient $e_0$ along the length of the cable (leftmost point is the location of the short); (b) Field along the radial coordinate calculated at a distance $\lambda/4$ from the shorted termination.
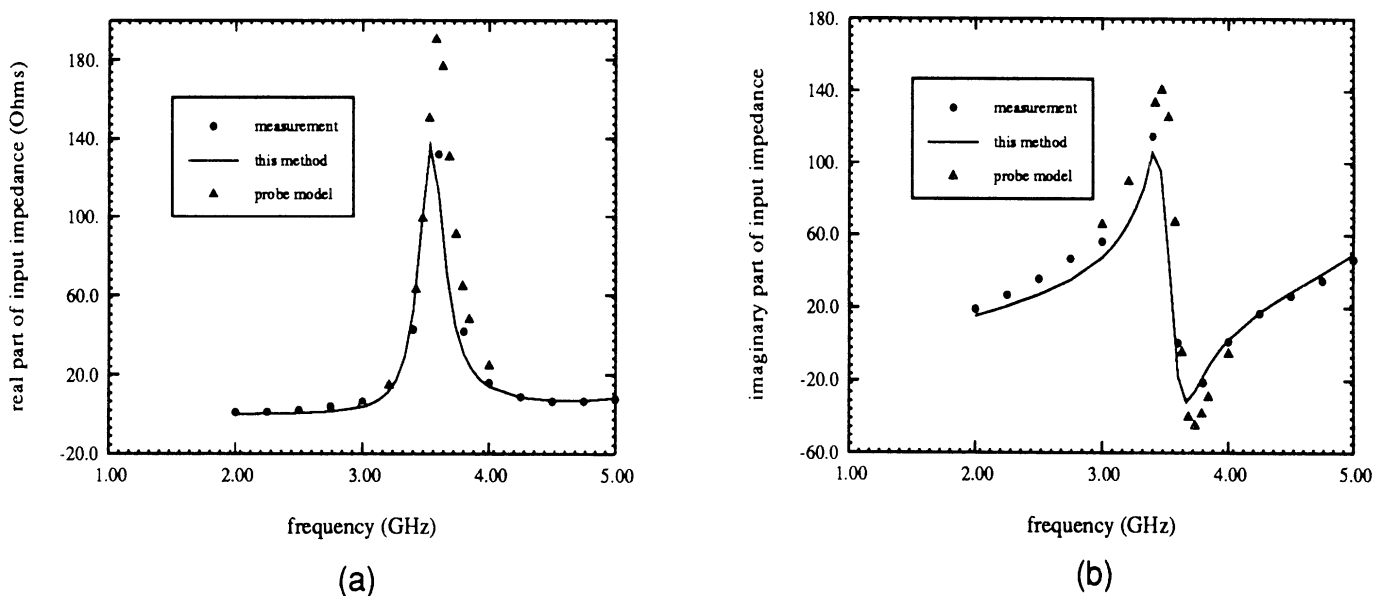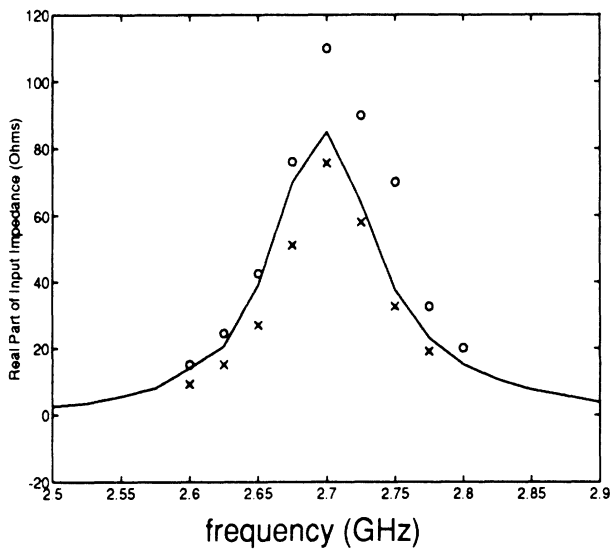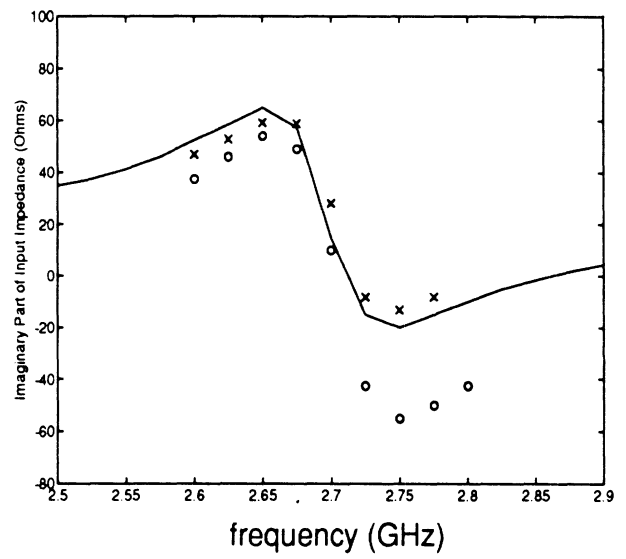


Figure 4: Measured and calculated input impedance for a cavity-backed circular patch antenna having the following specifications: patch radius r=13mm; cavity radius R=21.1mm; substrate thickness t=4.1mm; $\epsilon_r$=2.4; and feed location $x_f$=0.8 cm distance from center. Results based on the simple probe model are also shown for comparison. (a) Real part; (b) Imaginary part.

Figure 5: Measured and calculated input impedance for a circular patch antenna [6] having the following specifications: patch radius r=2cm; substrate thickness d=0.21844cm; feed location from center $x_f$=0.7cm; $\epsilon_r$=2.33; $tan\delta$=0.0012. [6]. —: measurement; xxx: this method; o o o: probe model [6] (a) Real part; (b) Imaginary part.

# Triangular prisms for edge-based vector finite element analysis of cavity-backed antennas recessed on planar platforms

T. Özdemir and J. L. Volakis

Radiation Laboratory
University of Michigan
Ann Arbor, Michigan 48109-2122

# 1    Introduction

The motivation for this work is the desire to characterize conformal antennas mounted on doubly curved platforms which are often seen on the surfaces of aircrafts and missiles. The suggested technique is to first discretize the platform surface containing the antenna and then to grow the mesh up to the termination boundary by use of appropriate volume finite elements. When the surface mesh is created using triangular patches (which are very useful in modeling arbitrarily shaped surface structures), the logical volume element for growing the mesh is the triangular prism. The mesh is terminated using ABCs or Artificial Absorbers.

Here, we report the progress to date on the development of triangular elements and their testing for planar platforms. When the platform is planar, the volume elements are right triangular prisms.

# 2    Right triangular prism and edge-based vector basis functions

Figure 1a shows a right triangular prism as an edge-based vector finite element. The top and the bottom surfaces are identical and parallel to each other while the vertical arms are perpendicular to the base of the prism. The vector electric field inside the element is an interpolation among the nine vector unknowns each parallel to and constant along a particular edge of the prism. Hence the term *edge-based* is used to describe the interpolation. Mathematically speaking, the field inside the prism is the sum of nine scalar unknowns (corresponding to the magnitudes of vector unknowns along the edges of the prism) weighted by appropriate vector functions of position, which we will henceforth refer to as *basis functions*.

The prism is specified by its height, the lengths of and the angle between two sides of its triangular surface, namely, $c, d_2, d_3$ and $\alpha_1$, respectively. First, we need to compute some scalar and vector quantities that will be used later in our analysis. These are illustrated in Figure 1b and given by
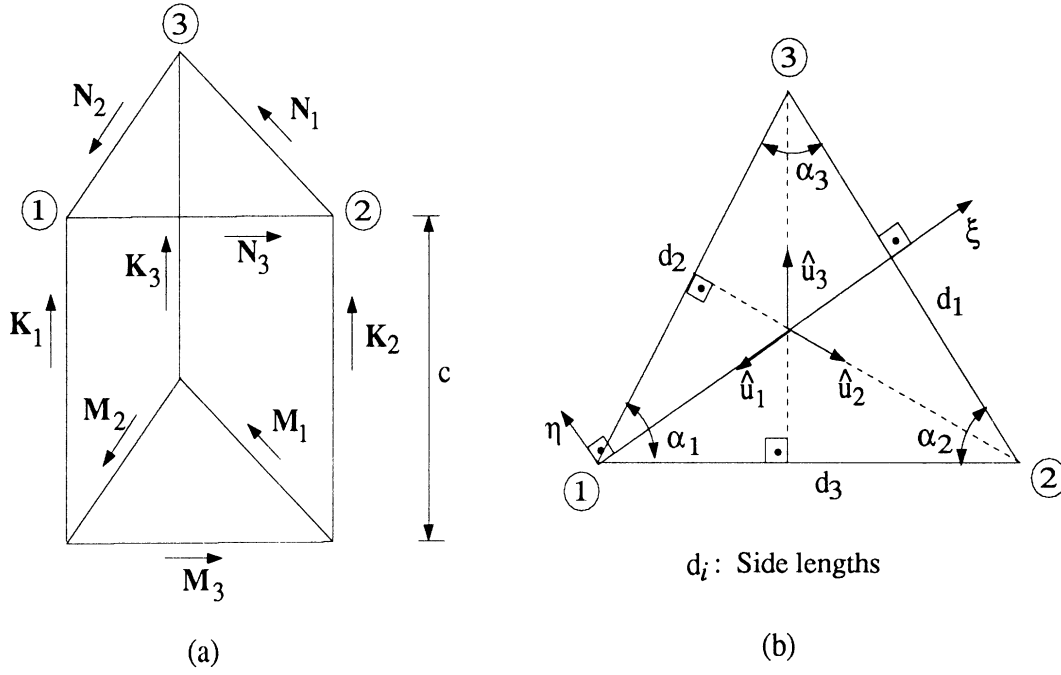
$$d_1 \quad = \quad \sqrt{d_2^2 + d_3^2 - 2d_2 d_3 cos\alpha_1}$$

Figure 1: Triangular prism with edge-based unknowns; (a) perspective view; (b) top view.

$$\alpha_2 = \cos^{-1}\left(\frac{d_1^2 + d_3^2 - d_2^2}{2d_1 d_3}\right)$$

$$\alpha_3 = \cos^{-1}\left(\frac{d_1^2 + d_2^2 - d_3^2}{2d_1 d_2}\right)$$

$$h_1 = d_2 \sin \alpha_3$$

$$h_2 = d_3 \sin \alpha_1$$

$$h_3 = d_1 \sin \alpha_2$$

$$\hat{u}_1 = -\hat{\xi}$$

$$\hat{u}_2 = \cos \alpha_3 \,\hat{\xi} - \sin \alpha_3 \,\hat{\eta}$$

$$\hat{u}_3 = \cos \alpha_2 \,\hat{\xi} + \sin \alpha_2 \,\hat{\eta}$$

In developing the vector edge-based basis functions, we will make use of the linear node-based scalar basis functions for the triangle given in Figure 1b [1]. Based on the $(\xi, \eta)$ coordinate system chosen for convenience, these basis functions are given by
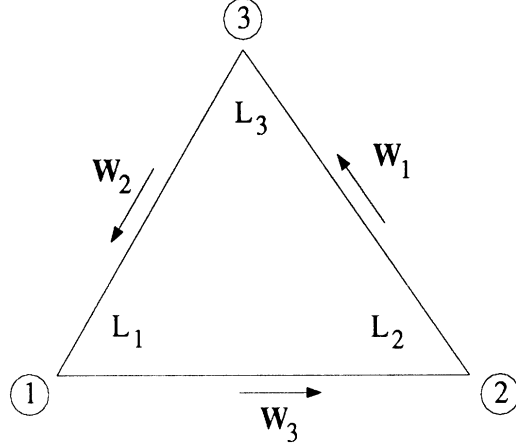
$$L_1(\xi, \eta) = 1 - \frac{1}{h_1}\xi$$

71

Figure 2: Local indexing for the triangle; node based scalar and edge-based vector basis functions

$$L_2(\xi,\eta) = \frac{\cos\alpha_3}{h_2}\xi - \frac{\sin\alpha_3}{h_2}\eta$$

$$L_3(\xi,\eta) = \frac{\cos\alpha_2}{h_3}\xi + \frac{\sin\alpha_2}{h_3}\eta.$$

Figure 2 shows the local indexing of the edge unknowns. Satisfying both the condition of divergenceless and the condition of the continuity of the tangential fields across neighboring elements, the obvious choice for the vector basis functions associated with the vertical arms of the prism is

$$\mathbf{K}_1(\xi,\eta) = \hat{z}\,L_1(\xi,\eta)$$

$$\mathbf{K}_2(\xi,\eta) = \hat{z}\,L_2(\xi,\eta)$$

$$\mathbf{K}_3(\xi,\eta) = \hat{z}\,L_3(\xi,\eta)$$

where $\hat{z}$ is the unit vector in the vertical direction.

The development of the basis functions for the horizontal edges of the prism involve two steps. We first derive the edge-based vector basis functions for the horizontal (triangular) surface of the prism by applying the Whitney [2] method. For the top triangular face, they are given by

$$\mathbf{W}_1 = d_1\,(\,L_2\nabla L_3 - L_3\nabla L_2\,)$$

72

$$\mathbf{W}_2 = d_2 \left( L_3 \nabla L_1 - L_1 \nabla L_3 \right)$$
$$\mathbf{W}_3 = d_3 \left( L_1 \nabla L_2 - L_2 \nabla L_1 \right)$$

which hold for the bottom triangular face as well. These functions have no vertical components and are divergenceless. They also support the continuity of the tangential fields across neighboring elements. Therefore, in reference to Figure 2, the final vector basis functions can be obtained from them without violating the divergenceless condition by simply multiplying those for the top surface by $z/c$ and those for the bottom surface by $1 - z/c$, i.e.,

$$\mathbf{N}_1 = \mathbf{W}_1 \, (z/c)$$
$$\mathbf{N}_2 = \mathbf{W}_2 \, (z/c)$$
$$\mathbf{N}_3 = \mathbf{W}_3 \, (z/c)$$
$$\mathbf{M}_1 = \mathbf{W}_1 \, (1 - z/c)$$
$$\mathbf{M}_2 = \mathbf{W}_2 \, (1 - z/c)$$
$$\mathbf{M}_3 = \mathbf{W}_3 \, (1 - z/c)$$

The vector basis functions in their final forms are given by

$$\mathbf{N}_1 = d_1 \left( L_2 \frac{\hat{u}_3}{h_3} - L_3 \frac{\hat{u}_2}{h_2} \right) (z/c)$$

$$\mathbf{N}_2 = d_2 \left( L_3 \frac{\hat{u}_1}{h_1} - L_1 \frac{\hat{u}_3}{h_3} \right) (z/c)$$

$$\mathbf{N}_3 = d_3 \left( L_1 \frac{\hat{u}_2}{h_2} - L_2 \frac{\hat{u}_1}{h_1} \right) (z/c)$$

$$\mathbf{M}_1 = d_1 \left( L_2 \frac{\hat{u}_3}{h_3} - L_3 \frac{\hat{u}_2}{h_2} \right) (1 - z/c)$$

$$\mathbf{M}_2 = d_2 \left( L_3 \frac{\hat{u}_1}{h_1} - L_1 \frac{\hat{u}_3}{h_3} \right) (1 - z/c)$$

$$\mathbf{M}_3 = d_3 \left( L_1 \frac{\hat{u}_2}{h_2} - L_2 \frac{\hat{u}_1}{h_1} \right) (1 - z/c)$$

$$\mathbf{K}_1 = \hat{z} \, L_1$$
$$\mathbf{K}_2 = \hat{z} \, L_2$$
$$\mathbf{K}_3 = \hat{z} \, L_3$$

# 3　Element Matrices

In the assembly of the finite element equations, the relevant quantities and their values are

$$ENNC_{i\ell} = \int\int\int_V (\nabla \times \mathbf{N}_i) \bullet (\nabla \times \mathbf{N}_\ell) dV$$

$$= \frac{d_i d_\ell}{c} \left( \frac{\cos\beta_{kn}}{h_k h_n} \chi_{jm} + \frac{\cos\beta_{jm}}{h_j h_m} \chi_{kn} - \frac{\cos\beta_{km}}{h_k h_m} \chi_{jn} - \frac{\cos\beta_{jn}}{h_j h_n} \chi_{km} + \right.$$
$$\left. \frac{2}{3} \frac{c^2 h_1 d_1}{h_j h_k h_m h_n} \sin\beta_{jk} \sin\beta_{mn} \right)$$

$$ENMC_{i\ell} = \int\int\int_V (\nabla \times \mathbf{N}_i) \bullet (\nabla \times \mathbf{M}_\ell) dV$$

$$= \frac{d_i d_\ell}{c} \left( -\frac{\cos\beta_{kn}}{h_k h_n} \chi_{jm} - \frac{\cos\beta_{jm}}{h_j h_m} \chi_{kn} + \frac{\cos\beta_{km}}{h_k h_m} \chi_{jn} + \frac{\cos\beta_{jn}}{h_j h_n} \chi_{km} + \right.$$
$$\left. \frac{1}{3} \frac{c^2 h_1 d_1}{h_j h_k h_m h_n} \sin\beta_{jk} \sin\beta_{mn} \right)$$

$$ENKC_{i\ell} = \int\int\int_V (\nabla \times \mathbf{N}_i) \bullet (\nabla \times \mathbf{K}_\ell) dV$$

$$= \frac{h_1 d_1}{6} d_i \left( \frac{\cos\beta_{j\ell}}{h_j h_\ell} - \frac{\cos\beta_{k\ell}}{h_k h_\ell} \right)$$

$$EMMC_{i\ell} = \int\int\int_V (\nabla \times \mathbf{M}_i) \bullet (\nabla \times \mathbf{M}_\ell) dV$$

$$= ENNC_{i\ell}$$

$$EMKC_{i\ell} = \int\int\int_V (\nabla \times \mathbf{M}_i) \bullet (\nabla \times \mathbf{K}_\ell) dV$$

$$= -ENKC_{i\ell}$$

$$EKKC_{i\ell} = \int\int\int_V (\nabla \times \mathbf{K}_i) \bullet (\nabla \times \mathbf{K}_\ell) dV$$

$$= c \frac{h_1 d_1}{2} \frac{\cos\beta_{i\ell}}{h_i h_l}$$

$$ENND_{i\ell} = \int\int\int_V \mathbf{N}_i \bullet \mathbf{N}_\ell dV$$

$$= c\frac{d_i d_\ell}{3}\left(\frac{\cos\beta_{kn}}{h_k h_n}\chi_{jm} + \frac{\cos\beta_{jm}}{h_j h_m}\chi_{kn} - \frac{\cos\beta_{km}}{h_k h_m}\chi_{jn} - \frac{\cos\beta_{jn}}{h_j h_n}\chi_{km}\right)$$

$$ENMD_{i\ell} = \int\int\int_V \mathbf{N}_i \bullet \mathbf{M}_\ell dV$$

$$= \frac{1}{2}ENND_{i\ell}$$

$$ENKD_{i\ell} = \int\int\int_V \mathbf{N}_i \bullet \mathbf{K}_\ell dV$$

$$= 0$$

$$EMMD_{i\ell} = \int\int\int_V \mathbf{M}_i \bullet \mathbf{M}_\ell dV$$

$$= ENND_{i\ell}$$

$$EMKD_{i\ell} = \int\int\int_V \mathbf{M}_i \bullet \mathbf{K}_\ell dV$$

$$= 0$$

$$EKKD_{i\ell} = \int\int\int_V \mathbf{K}_i \bullet \mathbf{K}_\ell dV$$

$$= c\chi_{i\ell}$$

where $V$ is the volume of the prism and

$$\beta_{rs} = \begin{cases} 0 & \text{if } r = s \\ \alpha_r + \alpha_s & \text{otherwise} \end{cases}$$

$$\chi_{rs} = \frac{h_1 d_1}{2}\left\{w_r w_s + \frac{h_1}{3}[(cot\alpha_3 - cot\alpha_2)(\eta_s w_r + \eta_r w_s) + 2(\xi_s w_r + \xi_r w_s)] + \right.$$

$$\left.\frac{h_1^2}{12}[3(cot\alpha_3 - cot\alpha_2)(\eta_s\xi_r + \eta_r\xi_s) + 2\eta_r\eta_s(cot^2\alpha_2 - cot\alpha_2 cot\alpha_3 + cot^2\alpha_3) + 6\xi_r\xi_s]\right\}$$

$$r, s = 1, 2, 3$$

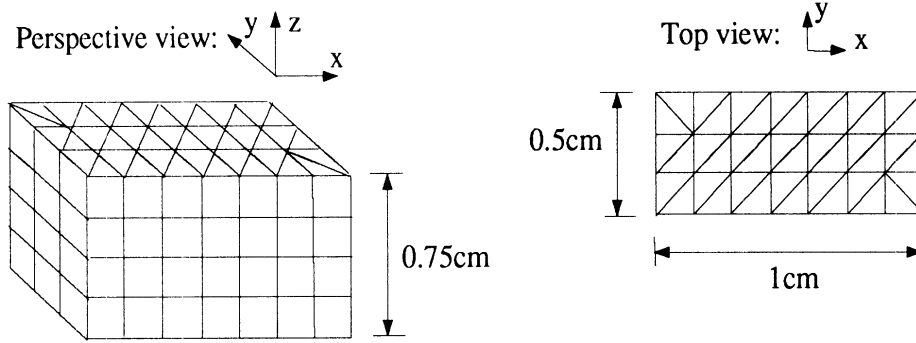| $i$ | $j$ | $k$ | $\ell$ | $m$ | $n$ |
|---|---|---|---|---|---|
| 1 | 2 | 3 | 1 | 2 | 3 |
| 2 | 3 | 1 | 2 | 3 | 1 |
| 3 | 1 | 2 | 3 | 1 | 2 |

$$w_1 = 1 \qquad \xi_1 = -\frac{1}{h_1} \qquad \eta_1 = 0$$

Figure 3: Discretization of the rectangular cavity using triangular prisms

$$w_2 = 0 \quad \xi_2 = \frac{\cos \alpha_3}{h_2} \quad \eta_2 = -\frac{\sin \alpha_3}{h_2}$$

$$w_3 = 0 \quad \xi_3 = \frac{\cos \alpha_2}{h_3} \quad \eta_3 = \frac{\sin \alpha_2}{h_3}$$

# 4 Testing of the right triangular prism

The new finite elements have been put to test in a variety of configurations involving eigenvalue computation, scattering and radiation problems. In the following four sections, we illustrate the performance of the new elements in dealing with four selective problems.

## 4.1 Eigen modes of a rectangular cavity

As a first test, we have computed the eigenvalues of the rectangular cavity shown in Figure 3. The cavity was first discretized using bricks. Then, the bricks were sliced diagonally to obtain two triangular prisms. Note that, the bricks at two corners were sliced along different diagonals from the bricks at the other two corners.

Finite element equations have been constructed by employing Galerkin's testing to obtain the generalized eigenvalue problem given by

$$AX = k^2 BX \tag{1}$$

where both $A$ and $B$ are *positive definite symmetric* matrices, $X$ is a column vector of edge unknowns, and $k$ is the wave number of any eigenmode supported by the cavity. There are widely available software packages for solving for $k$ in (1). Using one of these solvers, we computed the wave numbers for the first eight modes. Table 1 shows the percent error for triangular prisms along with the results for bricks and tetrahedrals [3]. The number of segments along the $x, y$, and $z$ directed edges are 7, 4, and 5, respectively, for both the triangular prism and the brick discretizations resulting in 382 edge unknowns in the triangular prism case and 270 edge unknowns in the brick case. Tetrahedral discretization, on the other hand, resulted in 260 unknowns. As one can see, the performance of the triangular prisms is comparable to the performances of bricks and tetrahedrals.

| Mode | Exact $(k, cm^{-1})$ | Triangular Prism (% Error) | Brick (% Error) | Tetrahedra (% Error) |
|---|---|---|---|---|
| $TE_{101}$ | 5.236 | -0.99 | -1.36 | 0.44 |
| $TM_{110}$ | 7.025 | -4.44 | -2.23 | 0.70 |
| $TE_{011}$ | 7.531 | 0.07 | -2.58 | 1.00 |
| $TE_{201}$ | 7.531 | -0.25 | -3.13 | -0.56 |
| $TM_{111}$ | 8.179 | -0.31 | -2.09 | 2.29 |
| $TE_{111}$ | 8.179 | -3.72 | -2.09 | 0.70 |
| $TM_{210}$ | 8.886 | -6.55 | -2.98 | 3.53 |
| $TE_{102}$ | 8.947 | -7.47 | -5.38 | 1.70 |

Table 1: Accuracy of triangular prisms in calculating the eigenvalues of a rectangular cavity of dimensions $1cm$ x $0.5cm$ x $0.75cm$ in comparison to bricks and tetrahedras.

## 4.2 Eigenmodes of a cylindrical-circular cavity

As a second test, we have discretized a cylindrical-circular cavity with metal walls as shown in Figure 4 using right triangular prisms and computed its eigenvalues. Table 2 shows the percentage error in calculation of the first five eigenvalues. The result is remarkable given the fact that the discretization resulted in only four edges along the radius as well as axis of the cylinder. This example shows the advantage of the triangular elements over rectangu-
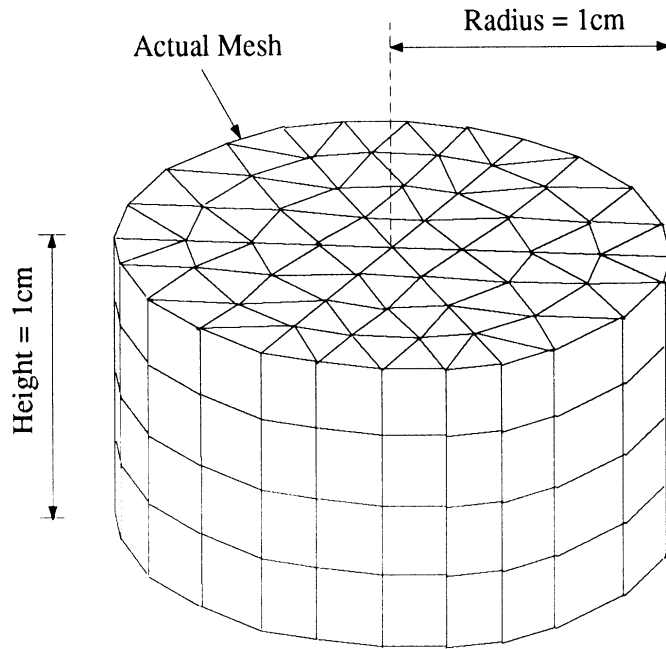
Figure 4: Cylindrical-circular cavity discretized using triangular prisms

lar ones in being able to model cavities with arbitrary cross section.

| Mode | Exact $(k, cm^{-1})$ | Triangular Prism (% Error) |
|---|---|---|
| $TM_{010}$ | 2.405 | 1.25 |
| $TE_{111}$ | 3.640 | 2.20 |
| $TM_{110}$ | 3.830 | 2.96 |
| $TM_{011}$ | 3.955 | 0.76 |
| $TE_{211}$ | 4.380 | -9.02 |

Table 2: Accuracy of triangular prisms in calculating the eigenvalues of a cylindrical-circular cavity of $1cm$ radius and height.
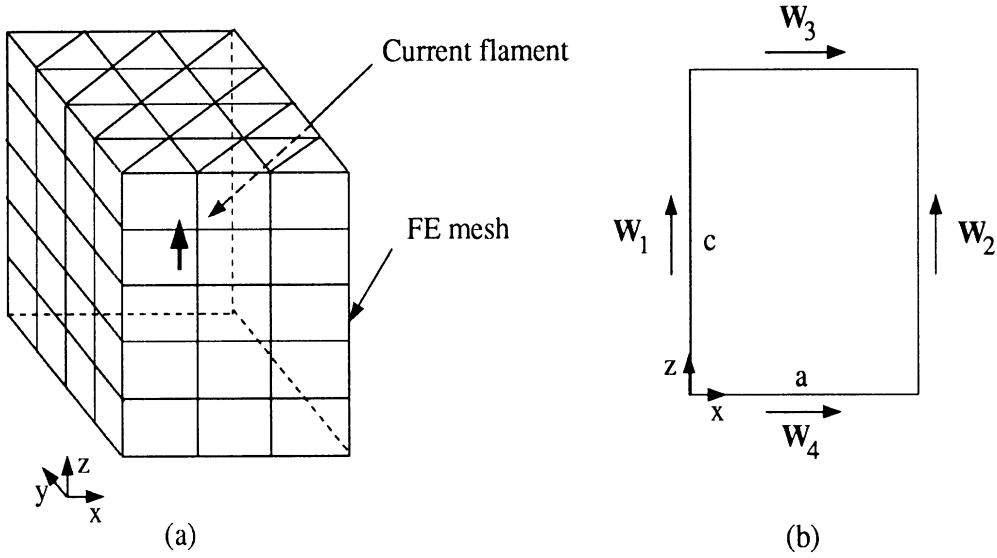
Figure 5: Problem geometry for radiation from a current flament; (a) finite element volume mesh surrounding the current flament; (b) a typical surface element on vertical faces of the finite element mesh.

## 4.3 Radiation from a small current filament in free-space

As a third test for the new elements, we have looked at the radiation from a small electric current filament in free-space. Figure 5a shows the problem geometry where a $\lambda_o/20$ long current filament in free space is situated at the center of a finite element mesh truncated a fraction of a wave length away from the filament forming a rectangular box. The mesh is made up of triangular prisms and is terminated using the second order symmetric absorbing boundary condition (ABC) given by [4]

$$\hat{n} \times \mathbf{H} = -Y_o \mathbf{E}_t + \frac{Y_o}{2k_o^2} \nabla \times [\hat{n}(\nabla \times \mathbf{E})_n] + \frac{Y_o}{2k_o^2} \nabla_t(\nabla \bullet \mathbf{E}) \qquad (2)$$

where $\hat{n}$, $Y_o$, and $k_o$ are the outward normal to the termination boundary, the free space wave admittance and the free space wave number, respectively.

In the assembly of finite element equations, in addition to the quantities given in Section 3 representing edge interactions within the mesh volume only, there are also quantities describing interactions among elements on the

termination boundaries. These involve both the triangular and rectangular faces of the triangular prisms making up the termination boundary. The quantities associated with the bottom triangular faces of the prisms are identical to those associated with the top triangular faces of the prisms. As a result, it suffices to present the quantities in two groups, the ones associated with the triangular faces and the ones associated with the rectangular faces. For the calculations, only the surface variations of the basis functions are relevant. The quantities associated with the triangular faces are (see Figures 1b and 2)

$$
\begin{aligned}
EC_{i\ell} &= \int\int_S (\nabla \times \mathbf{W}_i) \bullet (\nabla \times \mathbf{W}_i)\, dS \\
&= 2h_1 d_1 d_i d_\ell \frac{\sin \beta_{jk}}{h_j h_k} \frac{\sin \beta_{mn}}{h_m h_n} \\
ED_{i\ell} &= \int\int_S \mathbf{W}_i \bullet \mathbf{W}_\ell\, dS \\
&= d_i d_\ell [\chi_{jm}\frac{\cos \beta_{kn}}{h_k h_n} + \chi_{kn}\frac{\cos \beta_{jm}}{h_j h_m} - \chi_{jn}\frac{\cos \beta_{km}}{h_k h_m} - \chi_{km}\frac{\cos \beta_{jn}}{h_j h_n}]
\end{aligned}
$$

where $\chi_{ij}$ and the relationship of $j, k, m, n$ to $i$ and $j$ are given on page 7.

As for the rectangular faces (see Figure 5b), we first write the edge-based vector basis functions given by

$$
\begin{aligned}
\mathbf{W}_1 &= \left(1 - \frac{x}{a}\right)\hat{z} \\
\mathbf{W}_2 &= \frac{x}{a}\hat{z} \\
\mathbf{W}_3 &= \frac{z}{c}\hat{x} \\
\mathbf{W}_4 &= \left(1 - \frac{z}{c}\right)\hat{x}
\end{aligned}
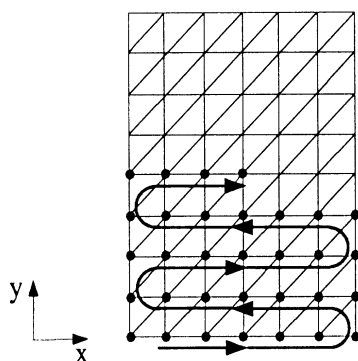$$

Then the relevant quantities are

Figure 6: Top surface of the finite element mesh. Solid circles mark the locations of computation of the data presented in Figures 6a and b. Arrows indicate the direction of increase for the index number making up the horizontal axis in Figures 6a and b.

| $i$ | $j$ | $EC_{ij}$ | $ED_{ij}$ |
|---|---|---|---|
| 1 | 1 | $\frac{c}{a}$ | $\frac{ac}{3}$ |
| 1 | 2 | $-\frac{c}{a}$ | $\frac{ac}{6}$ |
| 1 | 3 | $1$ | $0$ |
| 1 | 4 | $-1$ | $0$ |
| 2 | 2 | $\frac{c}{a}$ | $\frac{ac}{3}$ |
| 2 | 3 | $-1$ | $0$ |
| 2 | 4 | $1$ | $0$ |
| 3 | 3 | $\frac{a}{c}$ | $\frac{ac}{3}$ |
| 3 | 4 | $-\frac{a}{c}$ | $\frac{ac}{6}$ |
| 4 | 4 | $\frac{a}{c}$ | $\frac{ac}{3}$ |

The solid lines in Figures 7a and b show the percentage error in the computed magnitude and phase, respectively, of the z component of the electric field at points on the top surface of the finite element mesh (see Figure 6) located $0.25\lambda_o$ above the radiator. Dotted lines, on the other hand, show the same data observed at the same locations with the ABC surface pushed out in all directions to a distance of $0.45\lambda_o$ from the radiator displaying a significant improvement in the accuracy of the field computations. This is a testimony to the consistency of the new finite elements as well as the approximate termination method employed.
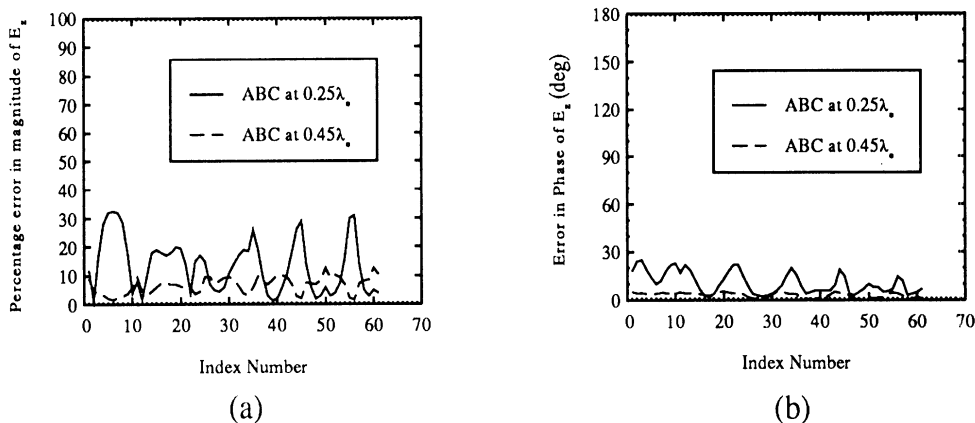
81

Figure 7: Error in computation of the z-component of the electric field due to a z-directed small electric current element (twentieth of a wave length long); (a) Percentage error in magnitude; (b) Error in phase. Computations are carried out at the top surface of the finite element mesh located a quarter of a wave length above the radiator. The computation points remain the same when the mesh termination boundary is pushed to 0.45 $\lambda$ . Exact locations of computation are shown in Figure 5.

## 4.4 Radiation and scattering from cavity backed structures

As the last test, we have looked at radiation and scattering from current elements inside three-dimensional cavities in an infinite ground plane and the scattering from such cavities. The general set up geometry is shown in Figure 8. As it is seen, a three dimensional cavity is discretized using the triangular prisms. The finite element mesh is extended outside the cavity in all directions about a fraction of the wave length and truncated using the same ABC used in the free-space radiation problem that has been described in the previous section.

We have first looked at the radiation from a pair of current elements residing inside the cavity; one horizontally and one vertically oriented as shown in Figure 9. Radiation pattern is shown in Figures 10a and b. The solid and dotted line esults were obtained using brick elements and closing the finite element domain at the aperture of the cavity via boundary integral (BI) method, which is an exact formulation and is explained in [5]. The triangular prism results were obtained in conjunction with the absorbing boundary condition (ABC) to truncate the mesh $0.3\lambda_o$ away from the cavity aperture in all directions. As the plots clearly demonstrate, the triangular
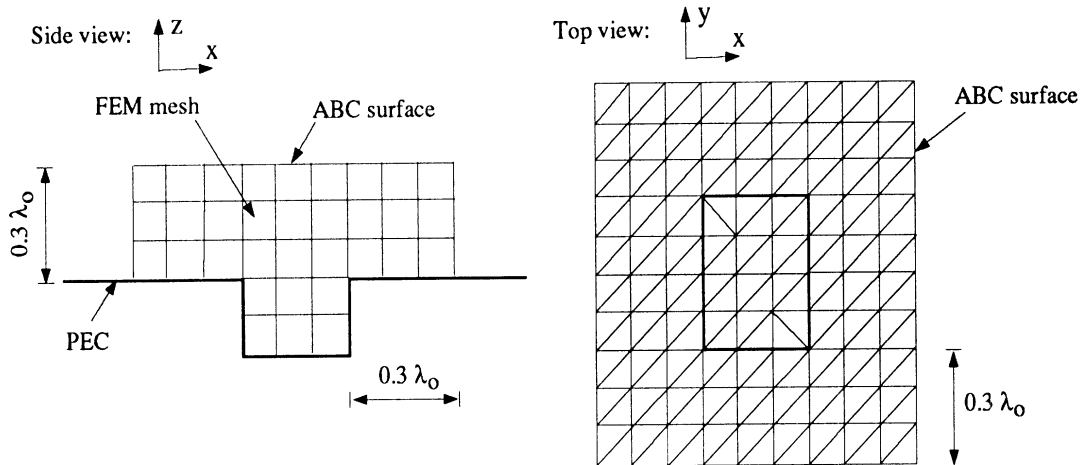
Figure 8: The geometrical set up for finite element-ABC formulation of radiation and scattering from cavities in infinite ground planes.

prisms together with the ABC perform well.

Next, we have looked at the plane wave scattering from a larger cavity whose dimensions in $x, y$, and $z$ directions are $1.2\lambda_o$, $0.75\lambda_o$, and $0.3\lambda_o$, respectively. The geometrical set up for the finite element-ABC formulation is the same as in the previous radiation problem which is illustrated in Figure 8. Figures 11 and 12 show bistatic and backscattering radar cross sections (RCS), respectively, of the cavity. It is seen that the FEM-ABC method using triangular prism elements exhibit sufficient accuracy in computing plane wave scattering from cavities in a ground plane.

# 5   Conclusions and future work

All results presented so far testify to the fact that the right triangular prism mesh, when used together with the second order ABC, yields good results for characterization of the radiation and scattering from cavity-backed antennas. The next step is the development and testing of the triangular prism for modeling antennas on doubly curved platforms. This element will have vertical arms not parallel to each other, and the associated edge-based vector basis functions will not therefore, be divergenceless. However, results presented so far are quite promising with regard to such elements [6].
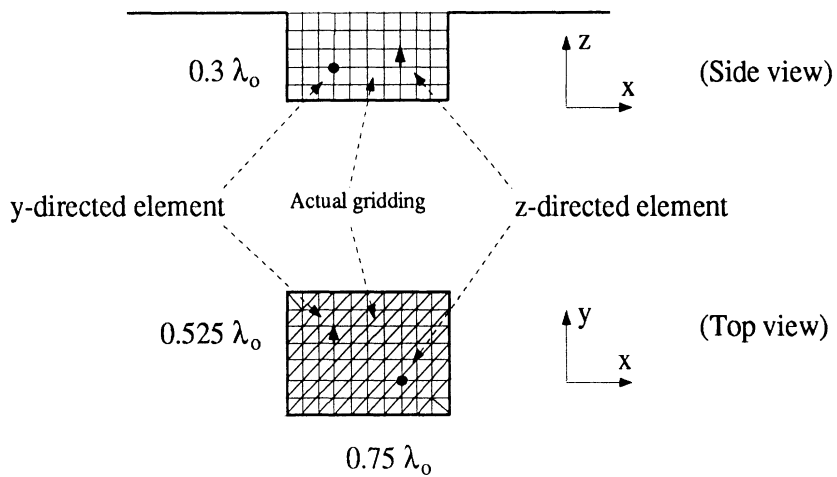
83

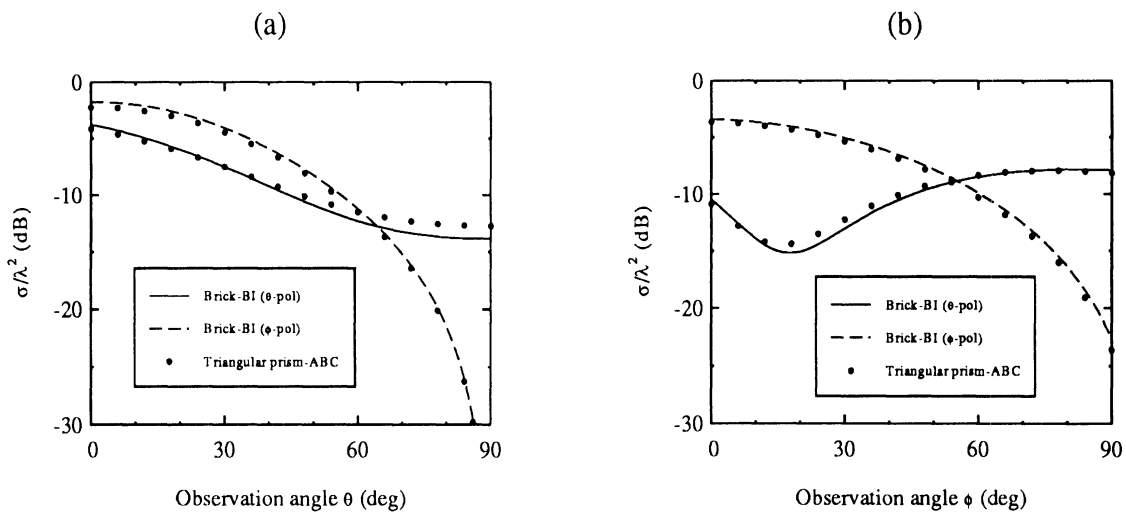Figure 9: Locations of current elements with respect to the gridding inside the cavity



Figure 10: Radiation pattern of two current elements located inside the cavity; (a) $\phi=45^{\circ}$; (b) $\theta=45^{\circ}$.
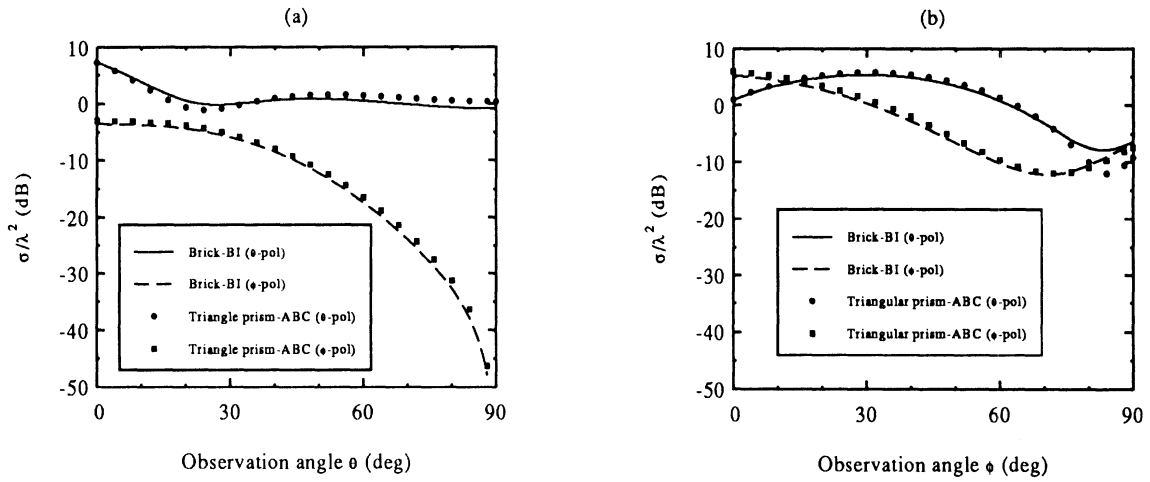
(a)



(b)



Figure 11: Bistatic RCS of a cavity of dimensions 1.2 $\lambda_0$ x 0.75 $\lambda_0$ x 0.3 $\lambda_0$ for a plane wave with its electric field vector making an angle of 45 with the unit vector in $\theta$ direction incident on the cavity aperutre at $\theta^{inc}$=45°, $\phi^{inc}$=30°, (a) $\phi$=60°, (b) $\theta$=45°.



(a)



(b)
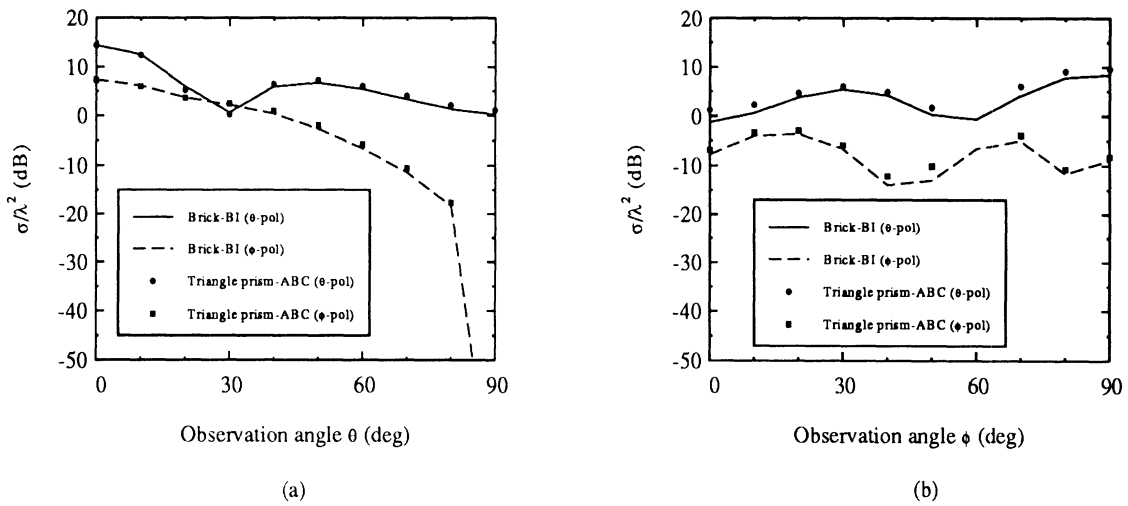
Figure 12: Backscatter RCS of a cavity of dimensions 1.2$\lambda_0$ x 0.75 $\lambda_0$ x 0.3$\lambda_0$ for an incident plane wave with its electric field vector making an angle of 30° with the unit vector in $\theta$ direction; (a) $\phi$=30°; (b) $\theta$=60°.

85

# References

[1] Zienkiewicz, O. C. and R. L. Taylor, *The Finite Element Method, Volume 1: Basic Formulation and Linear Problems*, Fourth Edition, McGraw-Hill Book Company (UK) Limited, London, 1989.

[2] Whitney, H., *Geometric Integration Theory*, Princeton University Press, Princeton, New Jersey, 1957.

[3] Chatterjee, A., J. M. Jin and J. L. Volakis, "Computation of Cavity Resonances Using Edge-Based Finite Elements," *IEEE Trans. Microwave Theory Tech.*, Vol. 40, No. 11, pp. 2106-2108, Nov. 1992.

[4] Webb, J. P. and V. N. Kanellopoulos, "Absorbing boundary conditions for finite element solution of the vector wave equation," *Microwave and Opt. Tech. Letters*, Vol. 2, No. 10, pp. 370-372, October 1989.

[5] Jin, J. M. and J. L. Volakis, "A finite element-boundary integral formulation for scattering by three-dimensional cavity-backed apertures," *IEEE Trans. Antennas Propagat.*, Vol. 39, pp. 97-104, Jan. 1991.

[6] Antilla, G. E. and N. G. Alexopoulos, "Scattering from complex three-dimensional geometries by a curvilinear hybrid finite element-integral equation approach," J. Opt. Soc. Am. A, vol. 11, no. 4, pp. 1445-57, April 1994.